A New Class of Resonant Metasurfaces Based on Highly Subwavelength Metamaterial-Lined Apertures and Metamaterial-Coated Discs

by

Elham Baladi

A thesis submitted in partial fulfillment of the requirements for the degree of

Doctor of Philosophy

in

Electromagnetics and Microwaves

Department of Electrical and Computer Engineering

University of Alberta

Abstract

This work presents analytical, numerical and experimental studies of a new class of resonant metasurfaces (MTSs), which may also be classified as miniaturized-element frequency selective surfaces (FSSs). The proposed MTS unit cells consist of circular aperture or disc resonators that are made subwavelength through the introduction of metamaterial (MTM) liners. First, the theory of reduced-frequency resonances in a circular aperture in a conducting screen lined using a layer of ϵ-negative and near-zero (ENNZ) MTM is studied by treating the liner as a homogeneous and anisotropic medium. It is shown that an array of circular apertures in a conducting screen whose interior is lined through thin layers of ENNZ MTM liners demonstrates resonant transmission at frequencies that are well below the natural resonance frequencies of unlined circular apertures of the same size or diffraction anomalies. Resonant transmission below the natural resonance frequency allows the use of smaller resonators at the operating frequency, resulting in miniaturization of the MTS unit cells. This theory is then extended through the application of Babinet's principle to the design of miniaturized resonant discs loaded using μ-negative and near-zero (MNNZ) MTM liners. A dual transmission-reflection spectrum is obtained at the reduced

resonant modes of the metallic disc resonators, providing frequency-selective reflection through compact MTSs at microwave frequencies.

Both the ENNZ and MNNZ liners in the proposed MTSs are realized through practical printed-circuit board (PCB) implementations. A homogenization scheme based on transmission-line studies of the liners is used to show that they provide the desired permittivity/permeability behaviour. Numerical and experimental studies are presented to verify the successful frequency-selective enhancement of transmission/reflection at the resonance frequencies of extremely subwavelength MTM-lined circular apertures/discs. As the transmission/reflection mechanism in such aperture/disc arrays does not rely on diffraction effects, and each resonator demonstrates isolated resonance behaviour, the resonators can be closely spaced, resulting in compact array sizes, which is important at RF/microwave frequencies. Furthermore, interesting Fano-shape transmission/reflection parameters are obtained at the resonance frequency of aperture/disc arrays, which may be beneficial for many applications. For example, this property has been used to design for strongly decoupled aperture resonators with slightly different resonance frequencies. Such isolated resonators are then used to design an imaging device that can magnify subwavelength conducting features to the far-field. The performance of this device has been verified numerically as well as experimentally. The Fano-shape reflection parameter in the disc array results in very-high transmission levels above the resonant reflection frequency, which is important for shielding applications that require the MTS to remain transparent

outside the shielding band. Extremely subwavelength, dual-band MTS unit cells are also developed based on the proposed MNNZ MTM-lined disc resonators combined with a different disc resonator realized through the application of μ-positive and large (MPL) liners. Practical MTS unit cell implementations are used throughout these studies, and homogenized sheet models are obtained to explain the resonance behaviour at different operating bands. The performance of the proposed dual-band MTSs is studied numerically as well as experimentally.

Preface

This thesis presents the design of highly subwavelength, MTM-loaded aperture/disc resonators in the microwave regime. In all the material presented in this thesis, Elham Baladi is the main student contributor. This work is conducted individually or in collaboration with other students in Prof. Iyer's research group, as explained below.

A portion of chapter 3 and the material in chapter 4 are published as E. Baladi, J. G. Pollock, and A. K. Iyer, "New approach for extraordinary transmission through an array of subwavelength apertures using thin ENNZ metamaterial liners", *Opt. Express*, Vol. 23, No. 16, pp. 20356-20365, July 2015. In this work, I performed the analysis, simulations and measurements, while Justin Pollock and Prof. Iyer provided the initial ideas and background on MTM-lined structures and assisted in writing and preparation of the manuscript. Chapter 5 was published as E. Baladi and A. K. Iyer, "Far-Field Magnification of Subdiffraction Conducting Features Using Metamaterial-Lined Aperture Arrays", *IEEE Trans. Antennas Propag.*, Vol. 66, No. 7, pp. 3482-3490, July 2018. Prof. Iyer played a strong supervisory role in providing the initial ideas and guiding the research, while I developed the ideas further and designed simulations and measurement setups to verify

them. Chapter 6 has been submitted as E. Baladi, M. Semple, and A. K. Iyer, "A Filtering Metasurface Based on Highly Miniaturized MNNZ-Loaded Discs", *IEEE Trans. Antennas Propagation*, and chapter 7 is prepared for submission as E. Baladi, M. Semple, and A. K. Iyer, "Single-Layer Dual-Band Polarization-Selective Metafilm with Independently Controlled and Closely Spaced Bands", *IEEE Trans. Antennas Propagation*. In both works, I have developed the theory, conducted the simulations and experiments, and Mitchell Semple assisted in verifying the theory and preparation of the manuscript. Prof. Iyer has supervised the research, and assisted in organization and production of both manuscripts.

Acknowledgements

First and foremost, I would like to express my sincere gratitude to my supervisor, Prof. Ashwin K. Iyer, for his guidance, encouragement, deep insights and constant support during the course of my Ph.D studies. I appreciate his fruitful discussions, immense knowledge and valuable suggestions that helped me learn something new every day. It has been a real privilege and great honor to have studied under Prof. Iyer's supervision for the last five years. Once again, thank you! I consider myself incredibly lucky to have met such an excellent instructor, mentor, and wonderful friend.

Second, I would like to thank my parents for their selfless love and endless care, and for always supporting my ambition in education. I could not have been where I am today without your support. Words cannot describe all my gratitude and love for you. I would also like to thank my loving husband, Mohammad, for his invaluable support and continuous encouragements, and my siblings, Sajad, Fateme and Kowsar, for always being there for me and encouraging me.

I would like to thank my colleagues- Justin, Stuart, Linh, Sanghamitro, Braden, Mitchell,

Contents

List of Figures

List of Tables

List of Abbreviations

MTM	Metamaterial
MTS	Metascreen
ENNZ	Epsilon Negative and Near Zero
EPNZ	Epsilon Positive and Near Zero
MNNZ	Mu Negative and Near Zero
MPL	Mu Positive (and larger than unity)
EOT	Extraordinary Optical Transmission
ET	Extraordinary Transmission
FSS	Frequency Selective Surface
1D	One Dimentional
2D	Two Dimentional
3D	Three Dimentional
TE	Transverse Electric
TM	Transverse Magnetic
TEM	Transverse Electric and Magnetic
HE	Hybrid Electric
EH	Hybrid Magnetic
NRI	Negative Refractive Index
TL	Transmission Line
GHz	Gigahertz
THz	Terahertz

PCB Printed Circuit Board

List of Symbols

γ Complex Axial Propagation Constant

α Axial Attenuation Constant

β Axial Propagation Constant

ρ Cylindrical Coordinate System's Radial Distance

ϕ Cylindrical Coordinate System's Azimuthal Angle

Z Cylindrical Coordinate System's Axial Distance

k_0 Free-space Propagation Constant

ϵ Permittivity

ϵ_0 Free-Space Permittivity

μ Permeability

μ_0 Free-Space Permeability

L Inductance

C Capacitance

Q Quality Factor

ω Angular Frequency

ω_{ep} Angular Electric Plasma Frequency

ω_{mp} Angular Magnetic Plasma Frequency

f Frequency

f_{ep} Electric Plasma Frequency

f_{mp} Magnetic Plasma Frequency

f_c Cutoff Frequency

f_r Resonance Frequency

Chapter 1

Introduction

1.1 Motivation

This work introduces a new class of resonant metasurfaces (MTSs) based on highly sub-wavelength metamaterial (MTM)-lined apertures and MTM-coated conducting discs. MTSs are the two-dimensional equivalents of MTMs and can replace them in many applications [1]. Resonant MTSs are periodic arrays of subwavelength apertures or scatterers, and operate in the regime that both the aperture/scatterer size and their periodicity in the array are small compared to the wavelength, but the individual apertures/scatterers are made resonant by means of modifying their shape/material properties. The highly-subwavelength and strongly decoupled resonant elements introduced in this work may be closely packed, yielding compact arrays as well as control over the transmitted/reflected

fields with high spatial resolution. Furthermore, the operating frequency as well as polarization selectivity of the proposed MTS unit cells is highly controllable, resulting in versatile design techniques. The bandwidth and degree of coupling of adjacent resonators may also be easily adjusted through the control of the Fano lineshape (i.e., a peak followed by a minimum, or vice versa) of transmission/reflection parameter. Eventually, these features may be adapted for the design of dual-band and polarization-selective MTSs, which demonstrate improvements as compared to the existing MTS or miniaturized-element frequency-selective surface (FSS) designs, including the single-layer geometry, independent control of the operating bands, and ease of designing for closely spaced bands.

Recently, it was shown that transmission through miniaturized circular waveguides (CWGs) can be vastly improved through the introduction of thin MTM liners [2]. Reduction in operating frequency while maintaining the waveguide size implies miniaturization. This work establishes the analogy between circular apertures and CWGs lined using ENNZ MTM liners, and demonstrates that this method is successful in miniaturizing the apertures as well. Therefore, miniaturization of the apertures will be achieved through MTM liners that do not add any additional thickness and/or transverse dimensions. A similar approach based on Babinet's principle is applied to miniaturize metallic disc resonators at microwave frequencies, and it is shown that an array of MTM-lined disc resonators demonstrates increased reflection at the operating frequency. Miniaturization of the unit cells inside an array also enables the description of these arrays in terms of

effective surface properties.

The first proposed MTS structure in this work is a uniform array of MTM-lined apertures designed to demonstrate ET at microwave frequencies. Extraordinary optical transmission (EOT) through a square array of subwavelength apertures on a metallic film was reported in 1998, when experiments in the optical regime observed unusual transmission and direct beaming of light through arrays of subwavelength apertures which were expected to transmit no light to the other side [3–5]. A peak was observed in the transmission spectrum, and found to be caused by the interaction of surface plasmon polaritons (SPPs) at the interface between imperfect metallic screens and air. Many works after that have further investigated the physical mechanisms responsible for the phenomenon, and the effect of changing different design parameters on the transmission behavior [6–13]. A wide range of applications, such as filtering, switching, sensing, and absorption spectroscopy were developed to benefit from this direct beaming of light through arrays of holes on the screen. Also, there have been extensive research activities to improve the transmission peak level and extend it to the other frequency ranges, such as microwave and millimeter wave frequencies [14–17]. Extraordinary transmission (ET) has been known in general to rely on diffraction effects, and occur at frequencies where the spacing of apertures measures one wavelength. Since a reasonably high number of apertures is needed to

get a strong transmitted beam through this mechanism, and considering the larger wavelength of microwaves, such arrays would possess a large overall size, which is undesirable. Thus, proposing ET mechanisms at the microwave regime that do not depend on diffraction effects but are realized by means of improved transmission through subwavelength apertures are preferred. Therefore, the proposed MTM-lined apertures that demonstrate strong resonant transmission while being subwavelength and closely spaced are suitable candidates for achieving ET in the microwave regime.

Another goal of this project was to develop cost- and size-effective imaging/sensing approaches using a nonuniform MTS consisted of these MTM-lined apertures. Imaging in general is limited by the diffraction limit [18], which expresses that the smallest feature that can be detected using a wave with wavelength of is $\lambda/(2n)$, where n is the refractive index of the medium in which imaging is performed (Abbe's limit, 1873). This results in a maximum resolution of $\lambda/2$ in free space. Therefore, development of techniques that enable imaging of obstacles beyond the diffraction limit is an ongoing challenge.

Periodic surfaces such as the ones introduced in this work may also be used to filter an interfering RF frequency adjacent to a desired transmission frequency in several antenna applications. This is particularly relevant to the shielding of ISM bands, which are unregulated frequency bands reserved internationally for industrial, scientific and medical applications. Specifically, the 2.4 GHz ISM band is often used by specialized medical

devices. The proposed MTSs could be used to mitigate interference taking place in critical situations, such as that between medical diagnostic devices and other ubiquitous RF sources in a hospital. Interpretation mistakes because of low-quality recordings caused by electromagnetic interference is another problem, which may result in misdiagnoses and unnecessary medical treatment, and may even be life-threatening. Therefore, more stringent shielding requirements are the answer to prevent electromagnetic interference from causing medical equipment malfunction. The MTSs designed here can be easily integrated to the medical devices operating at ISM frequency bands to protect them from possible interference. Although metallic sheets could be easily used for shielding, the advantage of the proposed periodic surfaces is to provide frequency and/or polarization selectivity. We show the possibility of polarization-selective and multi-band shielding with single-layer MTSs that offer independent control of operating bands and ease of designing for closely spaced bands. Other applications of such MTSs include shielding electronic devices in wireless-communication applications such as broadcast radio, Wi-Fi, mobile communication, and linear-polarization satellite communication systems, to protect the devices from malfunction and/or mitigate multipath effects.

Access to the interior region provided by aperture arrays can also be beneficial in sensing or characterization of fluids or biological materials. When a biological substance passes through the aperture and fills the empty interior, it is expected to cause a downshift in the resonance frequency. Additionally, when that material comes in contact with

the MTM liner region, it causes additional downshifting of the operating frequency by affecting the properties of the MTM liner. This can result in the design of highly sensitive sensors.

1.2 Objectives

The objectives of this work can be summarized as follows: (1) develop a complete analytical solution for the miniaturization of circular apertures in a conducting screen based on the analogy to MTM-lined circular waveguides, (2) apply Babinet's principle to obtain miniaturization of metallic disc resonators at microwave frequencies, (3) investigate the effective material properties of fully printed MTM liners and field distributions of reduced resonant modes in each of the above-mentioned designs, (4) use miniaturized circular apertures for obtaining ET at microwave frequencies; (5) design an imaging device capable of magnifying subwavelength distributions of obstacles that would otherwise be indistinguishable due to the diffraction limit; and (6) employ the MTM-lined discs for the design of novel MTSs that provide the possibility of polarization-sensitive and/or multi-band shielding through compact prototypes, and model the unit cells through an effective-medium description in terms of surface parameters. Objectives (4)-(6) are validated numerically as well as experimentally.

1.3 Outline

Chapter 2 provides a background on Bethe's aperture theory, MTMs and their realization and modeling, generalized sheet transition conditions and their application to characterize MTSs. Furthermore, a comprehensive background is presented on several areas and structures that can benefit from the proposed MTM-lined apertures and/or discs, including extraordinary transmission, frequency selective surfaces, metasurfaces and far-field imaging devices. Chapter 3 discusses the analogy between modes of a PEC circular waveguide and a circular aperture in a PEC screen, and explores the theory of reduced-frequency modes supported by the proposed ENNZ-lined circular apertures. Analytical solutions are presented for the reduced resonance frequencies of a circular aperture lined using a homogeneous and anisotropic MTM liner. This is followed by the analysis of a complementary unit cell, consisting of a metallic disc lined using an MNNZ MTM liner. It is discussed that a complementary unit cell design is expected to show complementary transmission/reflection behaviour. Transmission line models are presented to model the ENNZ/MNNZ liners, and obtain the corresponding electric/magnetic plasma frequencies, and to provide insight into the MTM liner's effective-medium parameters. Chapter 4 offers a new approach for extraordinary transmission by investigating the reduced HE_{11} mode of ENNZ-lined apertures. The ENNZ MTM liner is implemented using an arrangement of inductively loaded copper traces, and successful achievement of resonant

transmission enhancement at microwave frequencies is verified through full-wave electromagnetic simulations as well as experiments. Chapter 5 numerically and experimentally investigates far-field imaging of conducting obstacles through a nonuniform array of ENNZ-lined apertures mounted on the mouth of a TEM horn antenna, to build a near-field imaging probe that magnifies the information to the far-field. Furthermore, fully printed ENNZ-lined apertures are developed through replacing discrete loading inductors with printed, dual-arm spiral inductors, and are used for the realization of this imaging device. A novel complementary metafilm design based on MNNZ-lined metallic discs is studied through full-wave transmission and eigenmode studies in chapter 6. Generalized Sheet Transition Conditions (GSTCs) are used for extracting the susceptibilities of the proposed metafilm unit cell, which exhibit an electric-dipole-like behaviour at resonance. These studies are followed by experimental validation of the transmission behaviour of the proposed metafilm. Chapter 7 combines the metafilm technology based on MNNZ-lined discs presented in chapter 6 with another technology based on μ-positive (MPL)-lined discs to propose novel dual-band and polarization-selective metafilm designs. To conclude, chapter 8 proposes a number of potential future directions of research, including investigation of homogeneous sheet models for the proposed metascreen designs using GSTCs for metascreens, beam-shaping through the proposed metafilm designs, applying mode-matching techniques to explain the Fano profile of transmission/reflection, as well as extending all aspects of the present work to the design of optical devices. The use of

proposed metascreen/metafilm unit cells for dielectric sensing may also be explored as a future direction of this work.

Chapter 2

Background

2.1 Bethe's Aperture Theory

Diffraction of electromagnetic waves through an electrically small (i.e., small compared to the wavelength) circular aperture was studied theoretically in [19], commonly referred to as Bethe's aperture theory. This study obtains the transmission through a single circular aperture in a perfectly conducting (PEC) screen by applying Maxwell's equations and appropriate boundary conditions assuming a plane-wave excitation. The boundary conditions essentially enforce the tangential electric field to vanish on the PEC screen. Furthermore, as the holes are subwavelength, the electromagnetic fields can be assumed constant over the hole area. Fictitious magnetic charges and currents are used to model the effect of the hole in [19], and their value are adjusted so as to give the correct normal electric and tangential magnetic field components in the hole. It was concluded in [19] that an electrically small aperture diffracts the incident electromagnetic wave isotropically in

all directions, with minimal power radiated to the far-field.

The study in [19] investigates the transmission through a single subwavelength aperture. This study is extended in [20], for an array of subwavelength apertures in an infinitely thin PEC screen. It is shown that, in the small-aperture limit, the magnetic field of the lowest-order evanescent TM mode diverges for a finite electric field at the frequencies where the spacing of apertures approaches one wavelength, and therefore, this single mode dominates the transmission mechanism near its cutoff frequency in the regime where Bethe's theory is applicable. This information is used to replace the aperture with an equivalent magnetic polarization current proportional to the magnetic field of the lowest-order TM mode. This problem is then treated as solving for the transmitted field as excited by an array of magnetic polarization currents. The corresponding formulation shows a passband with 100% transmission at the frequencies below Wood-Rayleigh anomaly, as well as zero transmission at Wood-Rayleigh anomaly. The Wood-Rayleigh anomaly occurs at the frequency where the spacing of the apertures is equal to one wavelength [21, 22]. This corresponds to the lowest order diffracted wave from a grating, where the scattered wave emerges tangential to the screen, and produces a minimum in the transmission spectrum (more background on Wood-Rayleigh anomaly can be found in Appendix B). The analysis in [20] allows for a physical description of the total transmission phenomenon through an array of subwavelength apertures: the lowest order mode dominates the magnetic field at the surface, which is rescattered by the aperture array to

allow for total transmission.

2.2 Extraordinary Transmission

Experiments at optical frequencies have observed unusual transmission of light through periodic arrays of subwavelength apertures [3], and through single subwavelength apertures surrounded by 2D periodic grooves [5, 7]. As this phenomenon could not be rationalized using more well-known aperture-theoretical mechanisms, it was referred to as "extraordinary transmission" (ET). The prevailing understanding of these ET phenomena in most instances invokes diffraction-grating anomalies [8–11], which suggests that such ET is dominated by the periodicity of the apertures or grooves, rather than their dimensions, provided that they are subwavelength. In [8], Medina et al also offered a concise and accurate explanation of ET using modal equivalent circuits, which led to circuit-like approaches to control the induced surface currents and reduce the ET frequency, in regimes as high as the mid-infrared (see, for example, [23]). Similar efforts have led to the demonstration of ET at microwave and millimeter-wave frequencies [16, 17], where metals are essentially PEC and plasmonic effects cannot be relied upon. An alternate interpretation for the ET mechanism is offered in the concept of the so-called spoof surface plasmons (SSPs), which are essentially surface Bloch modes of the periodic structure that mimic the natural surface plasmon-polariton (SPP) response of imperfect metals [24]. This perspective suggests that ET occurs due to the excitation and coupling of SSPs, whose resonance

is given by the aperture's resonance frequency, but also strictly requires that the apertures be subwavelength in size. Whereas these two conditions would be at odds with each other for empty, unperturbed apertures, they could be reconciled by engineering the aperture's geometry or dielectric environment to lower its natural resonance frequency [12, 25]. Many recent approaches have involved covering the apertures with artificial media such as metamaterials (MTMs), whose function is similar to that of SPPs in that they promote coupling into and/or out of the aperture to enhance transmission. These include using an ϵ-near-zero (ENZ) material or an effective medium of nano-wires to couple incident waves into the aperture and radiate them as a highly directive beam [26–28], or employing bilayers with conjugately matched (i.e. positive- and negative-valued) material parameters to support a compact resonance across the aperture [29]. However, these techniques require either that the transverse dimensions of the MTM covers extend beyond the aperture or that they are extremely thick, and do not typically allow the apertures to be permeable. The above drawbacks limit the functionality of the above-mentioned approaches. The MTM liner used in this work, however, occupies a thin region at the edge of each hole, and no extra thickness or transverse size is added.

2.3 Frequency Selective Surfaces

Frequency Selective Surfaces (FSSs) are 2D periodic structures that are composed of shaped conductive patches or aperture elements designed to selectively reflect, transmit or absorb

EM waves at their operating frequency [30]. Patches refer to metallic scatterers of various shapes, which can be modeled using electric currents, while slots (or apertures) can be modeled using magnetic currents [30, 31]. Furthermore, according to Babinet's principle, complementary FSS designs are expected to demonstrate complementary transmission/reflection behaviour [30].

FSSs can be viewed as passive spatial filters to microwave and optical signals [32]. Similar to microwave filters, FSSs can have low-pass, high-pass, bandpass or bandstop frequency responses. However, their response not only depends on the frequency of the incoming electromagnetic wave, but also on its polarization and angle of incidence [33]. A simple equivalent circuit model presented in [33] shows the effect of different periodicities and angles of incidence on the effective circuit-model parameters of an FSS. FSSs have been extensively investigated during the past few decades, and find interesting applications in the design of reflectarrays, radomes, polarizers, beam splitters, microwave absorbers, and electromagnetic interference (EMI) reduction devices [30, 32, 34, 35]. They are also commonly used to increase the communication capabilities of satellite systems [36]. Although the use of traditional FSSs may be sometimes limited because of their narrow bandwidth and/or poor filtering response, a wide variety of solutions have been investigated in the literature for improving the characteristics of traditional FSSs, such as the use of active FSSs [37], fractal FSSs [38], as well as embedded and sandwiched FSSs

[39]. Multilayered FSSs have also been widely studied in order to overcome the shortcomings of single-layer designs [40–45].

The EM performance of an FSS is known to depend on the element type, geometry, substrate and spacing [30]. Traditional FSSs use simple geometries like loop, dipole, cross and patch type unit cells. Four basic groups of FSS elements are shown in Fig.2.1, which can be categorized into four basic groups [31]. N-poles or center-connected elements are shown in Fig.2.1(a), which include dipoles, tripoles, square spirals and Jerusalem crosses. Loop type elements, such as circular, square and hexagonal loops, are shown in Fig.2.1(b). Common patch-type elements are shown in Fig.2.1(c), and combinations of these three unit cells are shown in Fig.2.1(d).

There are two general classes of FSSs: resonant and non-resonant. The latter are often used when a broadband response is required. These two FSS classes are briefly discussed below.

2.3.1 Resonant FSSs

Resonant FSSs are 2D arrays of patches or slots that reflect or transmit, respectively, at the resonance frequency of their constituent elements [30]. The resonance frequency and bandwidth of resonant FSSs strongly depend on the resonance frequency and shape of the constituent resonant element (patch or slot); however, they are also substantially affected by the element spacing and the angle of incidence [46].
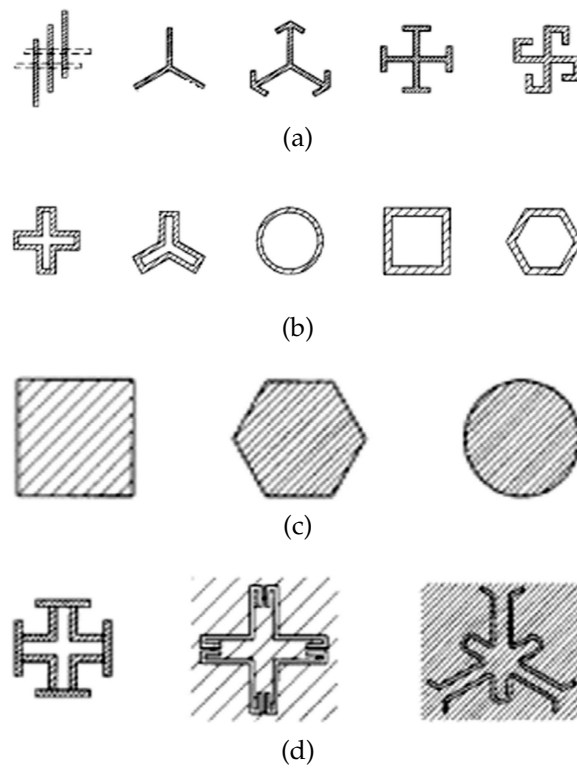
FIGURE 2.1: The four major FSS element geometries, including center connected or N-pole types, loop types, patch types, and combinations of these three shapes [30, 31]

Many applications, such as satellite systems, benefit from a dual-band FSS design. Multi-band FSSs are usually realized by stacking single-layer resonant FSSs with a quarter wavelength spacing, perturbation of a single-layered FSS, or the use of multi-band resonant-element FSSs [33, 36]. In general, the use of multi-band FSS elements is preferred to a multi-band FSS realized by stacking single layer FSSs, as the latter adds undesired extra thickness (especially at low frequencies), and causes stronger dependence of the response to the angle of incidence.

2.3.2 Non-Resonant FSSs

Non-resonant FSSs refer to structures consisting of both patches and slots placed on the two different sides of a substrate. In such designs, patches and slots are not individually resonant; however, they form capacitive and inductive grids, respectively, acting as a parallel LC circuit, which demonstrates a bandpass response [47]. One example of such FSS structures in shown in Fig. 2.2.

2.4 Metamaterials

Artificially constructed materials, or metamaterials (MTMs), have generated considerable interest during the last few decades. MTMs consist of periodically arranged inclusions which are small with respect to the incident EM wavelength. These materials can manipulate electromagnetic waves in surprising ways, and may be employed to achieve
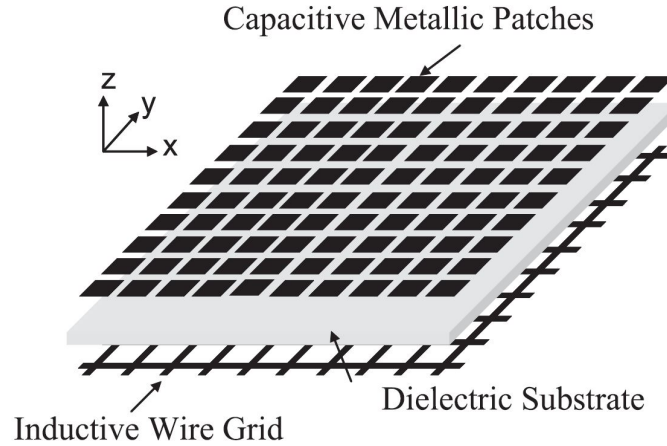
FIGURE 2.2: Topology of a band-pass, nonresonant FSS composed of a periodic array of metallic patches on one side of a dielectric substrate and an inductive wire grid on the other side [47].

intriguing propagation phenomena that are difficult or impossible to achieve with natural materials, such as a negative index of refraction. When an electromagnetic wave, consisting of oscillating electric and magnetic fields, and characterized by a wavelength, propagates through a conventional material, it sees an effective permittivity and permeability. As the wavelength is many times larger than the atoms of the material, we can conceptually replace the otherwise inhomogeneous medium by a homogeneous material characterized only by two macroscopic electromagnetic parameters: the electric permittivity, ϵ, and the magnetic permeability, μ [48]. In practice, any collection of particles whose size and spacing are much smaller than the wavelength can be described by an equivalent ϵ and μ. The values of ϵ and μ are determined based on scattering properties of the synthesized objects [48]. Most conventional materials have positive values of ϵ and μ, while MTMs can take a wide range of inhomogeneous (spatially varying) and anisotropic

(polarization-dependent) positive or negative parameters, through proper design procedures. Therefore, different classes of MTMs can be realized, including ϵ-positive ($\epsilon > 0$) or EPS materials, μ-positive ($\mu > 0$) or MPS materials, double-positive ($\epsilon > 0$ and $\mu > 0$) or DPS materials, ϵ-negative ($\epsilon < 0$) or ENG materials, μ-negative ($\mu < 0$) or MNG materials, and double-negative ($\epsilon < 0$ and $\mu < 0$) or DNG materials. In DNG MTMs, the refractive index ($n = \sqrt{\epsilon_r \mu_r}$) becomes negative. A negative refractive index (NRI) allows unique phenomena such as backward wave propagation and focusing.

MTMs are used in a variety of applications, including but not limited to the design of superlenses for imaging beyond the diffraction limit [49–52], invisibility cloaks [53, 54], tunneling of electromagnetic power and transparency [55], antenna miniaturization [56, 57], antenna gain/bandwidth improvement [58, 59], and beam-shaping [60, 61].

2.4.1 Realization

Split-ring resonators (SRRS) and thin wires are commonly used to implement MTMs in a wide frequency range from the microwave to the THz and optical regimes [62–65]. Nevertheless, many other forms of MTM implementations exist, which are obtained through judicious arrangements of metallic and dielectric objects in linear, planar, or volumetric fashions. One well-known class of MTMs are transmission-line (TL) MTMs, where negative permittivity and/or permeability is realized based on *L-C*-loaded TLs [66–68]. Other examples of MTM implementations are also studied in numerous works [68–75], some of

which are demonstrated in Fig. 2.3.

2.4.2 Modeling

MTMs may be modeled through various homogenization approaches, which introduce a generally dispersive, effective medium model for bulk properties (i.e., $\epsilon(\omega)$ and $\mu(\omega)$) of the volumetric MTM. Examples of these homogenization approaches include field averaging [76–80], scattering (S) parameter extraction method [81–84], and the dispersion-equation method [85]. Among these, the S-parameter inversion method is very popular, as it allows extraction of the permittivity and permeability from numerically or experimentally obtained S parameters [86]. The dispersive profile of permittivity/permeability of a MTM is often approximated through a Drude- or Lorentz-type dispersion model [87]. The simple Drude/Lorentz model description cannot model bianisotropic MTMs as it does not take the magnetoelectric coupling effects into account [88]. More complicated parameter extraction methods are available for bianisotropic MTMS (see, for example, [89]). The assumed Drude/Lorentz type dispersion of the effective parameters is in fact a limitation of many homogenization methods. However, studies show that the extracted parameters of MTMs often possess such a profile due to the strong resonant behaviour [83, 90, 91]. Lossy Drude profiles for permittivity and permeability are used in multiple works (see, for example, [92–94]), and may be described as:
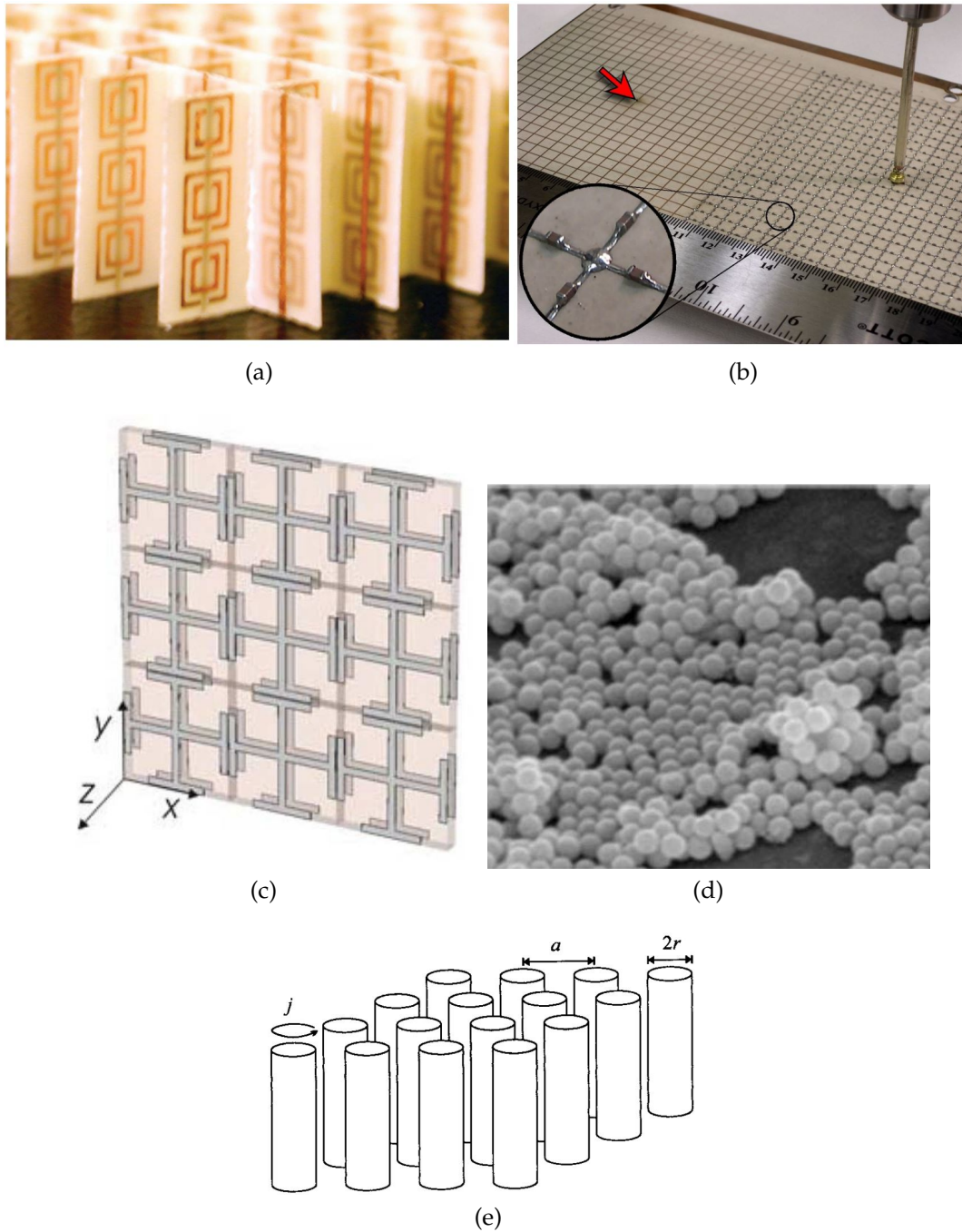
FIGURE 2.3: Various implementations of MTMs at frequency regimes ranging from the microwave to the optical: (a) SRRs and copper wire strips on fiber glass [75], (b) NRI-TL MTMs [68], (c) a periodic array of tightly coupled Jerusalem cross pairs [74], (c) spherical nanoparticles [71], and (e) a square array of metallic cylinders [70].

$$\epsilon(\omega) = \epsilon_0(1 - \frac{\omega_{pe}^2}{\omega(\omega - j\Gamma_e)}) \tag{2.1a}$$

$$\mu(\omega) = \mu_0(1 - \frac{\omega_{pm}^2}{\omega(\omega - j\Gamma_m)}) \tag{2.1b}$$

where ω_p refers to the corresponding plasma frequency and Γ denotes the the corresponding damping frequency. Other works, such as [75, 95–98] have used the Lorentz model and its derivatives to model dispersive electric and magnetic behaviour of MTMs, which may be describe as follows:

$$\epsilon(\omega) = \epsilon_0(1 + \frac{\omega_{pe}^2}{\omega_{0e}^2 - \omega^2 + j\Gamma_e\omega}) \tag{2.2a}$$

$$\mu(\omega) = \mu_0(1 + \frac{\omega_{pm}^2}{\omega_{0m}^2 - \omega^2 + j\Gamma_m\omega}) \tag{2.2b}$$

in these equations, ω_{0e} and ω_{0m} denote the electric and magnetic resonance frequencies, respectively.

2.5 Metasurfaces

Metasurfaces (MTSs) are the two-dimensional equivalents of MTMs, and can replace them in many applications [1]. They occupy less physical space than bulk, volumetric (3D)

MTMs, and are used in a wide frequency range from the microwave to the optical [63, 99–108]. By judiciously choosing the shape of their constituent scatterers, MTSs can be beneficial in many applications including, but not limited to, wavefront manipulation and the design of flat lenses [61, 109–114], high-resolution color printing [115–119], linear to circular polarization conversion [120–123], surface-wave coupling [24, 124, 125], polarization rotation [123, 126–128], the realization of zero-index properties [129, 130], shielding [131, 132], and switching [133, 134].

MTSs may be further classified into two topologies: a fishnet topology referring to apertures placed periodically in a metallic screen, which are called metascreens, or a cermet topology, referring to a 2D array of isolated metallic scatterers, called metafilms [135]. Other kinds of MTSs might be designed that lie somewhere between these two extremes [1]. Figure 2.4 illustrates the general shape of a metascreen and a metafilm consisted of arbitrarily shaped apertures/scatterers [136].

Nonuniform MTSs are commonly used for beam shaping through simultaneous control of magnitude and phase of transmitted/reflected waves. Such designs are commonly called transmitarrays/reflectarrays [137–141]. Although complete control over the beam requires adjustability of both magnitude and phase of the transmission/reflection parameter, varying the amplitude usually results in undesired loss of power, which is unwanted [142]. Consequently, in such applications, the MTS unit cells are usually designed to possess equal transmission/reflection magnitudes, and introduce a constant phase gradient

(a)

(b)
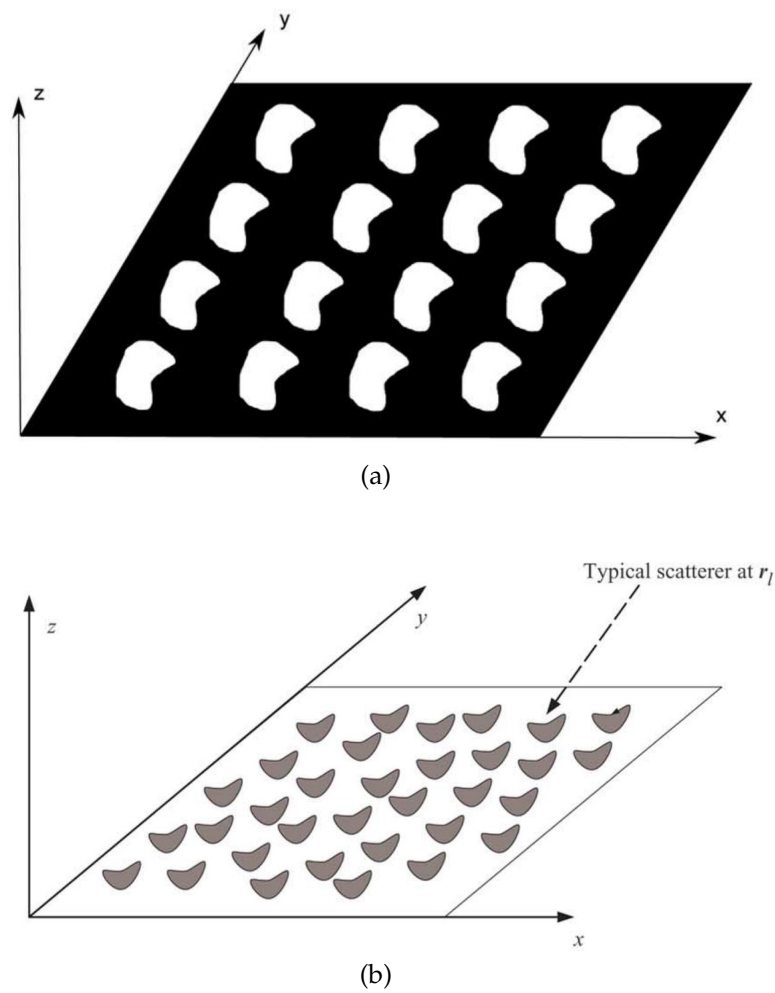
FIGURE 2.4: Topologies of (a) a metascreen and (b) a metafilm, consisted of arbitrarily shaped apertures/scatterers [136].

vector at a particular frequency, which provides an effective wavevector along the interface [103]. The effective wavevector introduced through the phase-gradient MTS imparts momentum to transmitted/reflected waves, causing the desired re-direction of the beam. Generalized laws of reflection and refraction are derived in [143, 144] to calculate the redirection angle based on the interfacial phase gradient as well as the refractive indices of the surrounding media. It is worth mentioning that this beam redirection effect is analogous to the effect of conventional optical elements such as prisms that use thickness variation to induce a phase gradient. However, MTSs facilitate the realization of arbitrary phase distributions using planar arrays of subwavelength elements that can be easily fabricated through a single-step lithography process [145]. Phase control is generally achieved through the choice of shape and dimensions of MTS unit cells [143, 146–149]. One of the most well-known demonstrations of beam-shaping MTSs has been done through the use of V-shaped antenna elements [143, 148], as shown in Fig. 2.5.

Similar to FSSs, MTSs may utilize resonant or non-resonant elements.

2.5.1 Resonant MTSs

Resonant MTSs are obtained when the scatterer size and their periodicity in the array are small compared to the wavelength, but the individual scatterers are made resonant by means of modifying their shape/material properties [1]. As both the scatterer and the periodicity are electrically small, an effective-medium model can be defined in this regime;
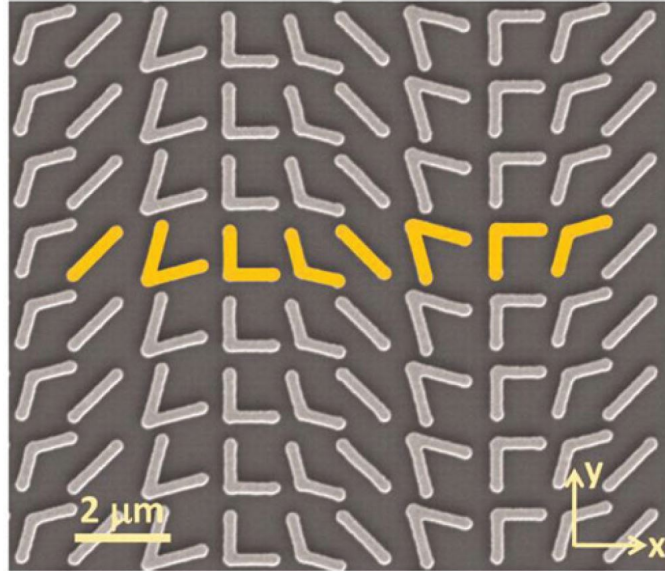
FIGURE 2.5: A beam-shaping MTS utilizing V-shaped nanoantennas [143].

however, this model would be strongly dispersive due to expectedly different responses at and away from the resonance frequency. This regime of operation presents interesting possibilities, as it provides functionality for a wide range of applications while allowing compact scatterer and array dimensions.

2.5.2 Non-Resonant MTSs

In this regime, both the scatterer size and their spacing (i.e., array periodicity) are very small compared to the free-space wavelength, and the scatterers are non-resonant. In this regime, a non-dispersive or weakly dispersive effective-medium model can be defined for the array.

Therefore, MTSs are preferred to ET or FSS designs in terms of compactness, as in

the ET/FSS regime of operation either the periodicity of scatterers inside the array is on the order of one wavelength (the ET regime), or the scatterers are electrically large, and therefore, resonant (as in resonant FSSs).

2.6 Far-Field Imaging/Magnification

Far-field imaging is limited by the diffraction limit [18], which expresses that the smallest feature size that can be imaged using a wave with wavelength of λ is $\lambda/(2n)$, where n is the refractive index of the medium in which imaging is performed (Abbe's limit, 1873). This results in a maximum resolution of $\lambda/2$ in free space. These constraints have prompted the development MTM-based devices such as hyperlenses. Hyperlenses are near-field imaging devices that magnify subdiffraction details by creating diverging resonant paths through an anisotropic, inhomogeneous, and potentially lossy medium, which may then be imaged in the far-field using conventional optical means [50, 87, 150, 151]. More conventionally, near-field probes - essentially electrically small receiving antennas - are used to discern subwavelength details. Such probes must be scanned from location to location to obtain the full image of an object/environment, since any parallel imaging arrangement would be limited by high coupling between adjacent probes. This series imaging scheme can be very time-consuming as compared to parallel approaches, which provide information about multiple locations at once. Therefore, development of parallel, beyond-the-diffraction-limit imaging schemes becomes necessary.

2.7   Generalized Sheet Transition Conditions (GSTCs)

Recently, GSTCs have widely been used to characterize MTSs [135] by relating the jump in the electromagnetic fields at the two sides of a MTS to the average fields on the MTS through surface susceptibility tensors $\bar{\bar{\chi}}$. GSTCs are equivalent boundary conditions that explain the interactions of MTSs with incident electromagnetic waves. These boundary conditions were named GSTCs by Senior and Volakis [152–154], who used such conditions to approximately describe simple structures.

There are distinctions between metascreens and metafilms in terms of the value of surface currents that necessitate separate studies of the two topologies. The first set of GSTC conditions for a metafilm that take the interaction between the scatterers into account, and consider both electric and magnetic polarizabilities, are derived in [135]. These conditions also allow relating the transmission and reflection parameters of a metafilm to its polarization densities [135]. The susceptibility tensors of a metafilm assume a homogenized and dispersive model for the discrete (inhomogeneous) distribution of its electrically small scatterers, and are related to the electric and magnetic polarizabilities of the scatterers as well as their densities on the metafilm [135, 155, 156]. Although previous works had also modeled the interaction of EM waves with a surface, they lacked completeness as they either did not model the interactions between the equivalent electric/magnetic dipoles [157], or only considered the electric polarizabilities of the scatterers and failed to take the

magnetic polarizabilities into account [157–159]. The GSTCs obtained in [135] allow general shapes of scatterers, as long as the distribution of scatterers is dense with respect to the wavelength (so that the average fields can be approximated by continuous surface distributions of polarization and magnetization densities) and sparse compared to the size of the scatterers (so that the field acting on one of the scatterers can be obtained by replacing all the other ones by continuous polarization and magnetization densities).

The GSTC conditions for a metascreen are derived in [160], which use effective surface susceptibilities and surface porosities to model the geometry and distribution of apertures in a metallic screen (i.e., metascreen unit cells). The GSTCs obtained in [160] allow the apertures to be arbitrarily shaped, but their dimensions are required to be small in comparison with the wavelength in the surrounding medium. As mentioned earlier, the main distinction between GSTC conditions for metafilms and metascreens is that the isolated scatterers in a metafilm imply small surface currents between the scatterers, whereas metascreens possess nonzero currents along their surface that must be taken into account, even if the periodicity of the array is very small.

GSTCs may be used in numerical modeling of MTSs using FDTD [161–163] and FEM [164] methods, or to explain unique behaviours such as insensitivity of transmission and reflection parameters to the angle of incidence [165]. GSTCs also provide insight into the value and frequency behaviour of surface parameters, and how that affects the behaviour of the MTS [160], which is beneficial for synthesizing these parameters in order to obtain

the desired transmission and/or reflection response.

Chapter 3

Theory

3.1 The Analogy Between Circular Apertures and Circular Waveguides

Apertures are widely used in electromagnetics mainly for the coupling or radiation of electromagnetic waves. Circular apertures are common in many of these applications. On the other hand, many properties of these apertures can be studied in similarity to circular waveguides. For circular apertures placed in a conducting screen, the transverse boundary conditions are same as those in the cross section of a metallic circular waveguide. Moreover, if the metallic screen containing the apertures possesses an electrical thickness, the apertures are, in fact, very short circular waveguides. Therefore, the cutoff (resonance) frequency above which an aperture will effectively radiate/transmit power can also be evaluated by analyzing the equivalent circular waveguide. Air-filled waveguides

enclosed by perfect-electric-conducting (PEC) boundaries support a discrete spectrum of modes as is well known, each possessing a cutoff frequency. Below their cutoff frequency, waveguides are not capable of propagating power. One way to reduce these cutoff frequencies to miniaturize waveguides is homogeneously filling the vacuum region inside the waveguide with an isotropic dielectric material, which does not modify the corresponding transverse modal field distributions. However, this method of reducing the cutoff frequency does not allow access to the interior region of a waveguide. Another way of manipulating the cutoff frequency of a metallic waveguide is partially/inhomogeneously filling it with a dielectric. This can affect the modal field distributions significantly. Filling a PEC circular waveguide with two concentric dielectric regions is an example [166, 167]. This structure is capable of supporting hybrid electric (HE) and hybrid magnetic (EH) modes which are similar to the transverse electric (TE-) and transverse magnetic (TM-) modes of a similar homogeneously filled circular waveguide, respectively, except that longitudinal electric or magnetic field components do not vanish in the former. However, under certain conditions such as circularly symmetric field distributions or near cutoff, these hybrid modes can reduce to the TE and TM modes of a homogeneously filled circular waveguide (CWG) [166, 167]. The dielectric liner's permittivity, permeability, and thickness might be optimized to engineer the modal dispersion characteristics [168, 169].

Another approach for engineering the propagation constant and modal dispersion characteristics is metamaterial (MTM) loading of the waveguides. It has been shown that

propagation can be restored far below the cutoff frequency of waveguides by loading them using elements such as the split-ring resonator (SRR), complementary split-ring-resonator (CSRR), or wire-lines [169, 170]. The study in [2] investigated the intriguing effects of inhomogeneously filling circular waveguides with thin ϵ-negative and near-zero (ENNZ) MTM liners. This study established the possibility of below-cutoff propagation resulting in waveguide miniaturization, resonant tunneling of power, backward coupling of power, and field collimation. A rigorous hybrid-mode analysis was done to determine the MTM-lined waveguide's dispersion features, cutoff frequencies, and field patterns. A methodology to control the reduced cutoff frequencies through varying either the permittivity's dispersion profile and/or the liner's thickness was developed. The present work establishes the analogy between below-cutoff transmission through miniaturized MTM-lined CWGs and enhanced transmission through arrays of subwavelength apertures loaded using ENNZ MTM liners. Partially filled miniaturized apertures allow access to the interior region of the aperture, which is advantageous for shielding applications that require visual accessibility, or sensing of fluids and biological materials that require the substances to pass through the apertures. This miniaturization technique is presented in detail in the next section.

3.2 ENNZ MTM-Lined Apertures

A similar theory to the ENNZ-lined CWGs is developed in this section for miniaturizing circular apertures. Figure 3.1(a) presents the geometry of the structure under consideration, which is an MTM-lined circular aperture in a PEC screen. An inner vacuum region (ϵ_0, μ_0) of radius of a is surrounded by an outer MTM region of thickness $b - a$, which is assigned a dispersive relative permittivity $\epsilon_r(f)$ and a nonmagnetic response. This radially inhomogeneous aperture supports hybrid electric (HE-) and magnetic (EH-) mode resonances which are similar to the TE and TM modes of a homogeneously filled aperture except that the former generally exhibit longitudinal E- or H-field components, respectively, in order to satisfy the additional boundary conditions introduced by the inhomogeneity.

Similar to a CWG, the resonant modes of a circular aperture in a conducting screen are determined by the solutions of an equation recognized as Bessel's differential equation [171], which are called Bessel functions. The resonance frequencies of a homogeneously filled circular aperture in a conducting screen with a filling material possessing a permittivity of ϵ and a permeability of μ may therefore be calculated using the following formulas [171]:

$$f_{r_{nm}}^{TE} = \frac{P'_{nm}}{2\pi a \sqrt{\mu \epsilon}} \tag{3.1a}$$

$$f_{r_{nm}}^{TM} = \frac{P_{nm}}{2\pi a \sqrt{\mu \epsilon}} \tag{3.1b}$$

(a)

(b)

(c)
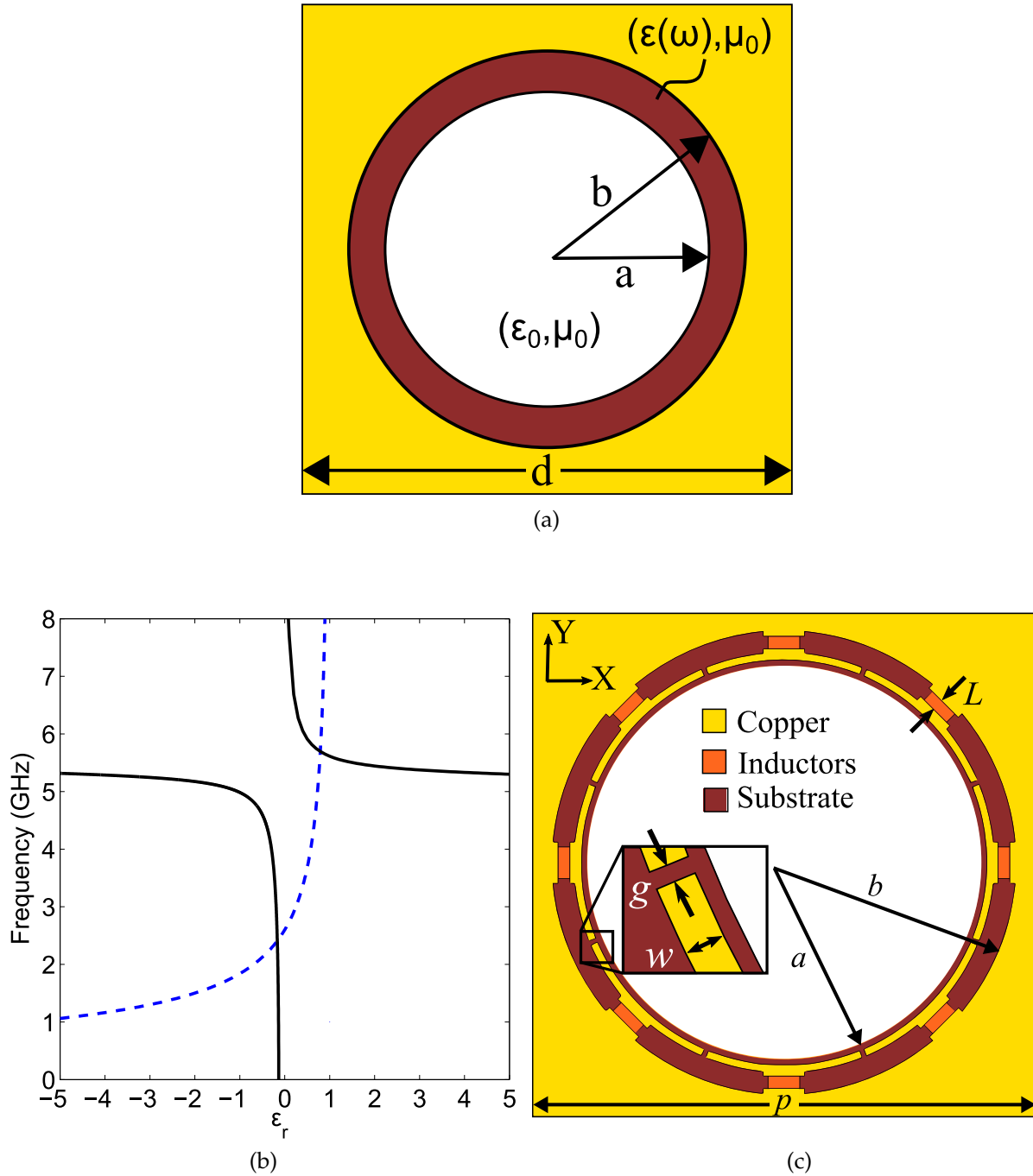
FIGURE 3.1: (a) Transverse cross-section of the MTM-lined circular aperture consisting of an inner vacuum region and a nonmagnetic outer liner region with a relative dispersive permittivity $\epsilon_r(f)$. (b) The HE_{11}-mode resonance frequency versus liner permittivity (solid black curve) along with the Drude dispersion profile of $\epsilon_r(f)$ (dashed blue curve). (c) A printed-circuit implementation of an ENNZ MTM-lined aperture.

where n refers to the number of variations in the azimuthal (ϕ) direction and m refers to the number of variations in the radial (ρ) direction, P_{nm} is the mth root of the Bessel function of the first kind (i.e., J_n) and P'_{nm} is the mth root of its derivative (i.e., J'_n). Table 3.1 shows the values of P_{nm} and P'_{nm} required for calculating the resonance frequencies of TM and TE modes, respectively, of a circular aperture in a conducting screen.

n	m	P_{nm}	P'_{nm}
0	1	2.405	3.832
0	2	5.520	7.016
0	3	8.654	10.174
1	1	3.832	1.841
1	2	7.016	5.331
1	3	10.174	8.536
2	1	5.135	3.054
2	2	8.417	6.706
2	3	11.620	9.97
3	1	6.380	4.201

TABLE 3.1: Values of P_{nm} and P'_{nm} for different values of n and m.

Figure 3.2 shows the distribution and magnitude of electric field vectors of the four lowest order modes of a representative circular aperture in a conducting screen, which
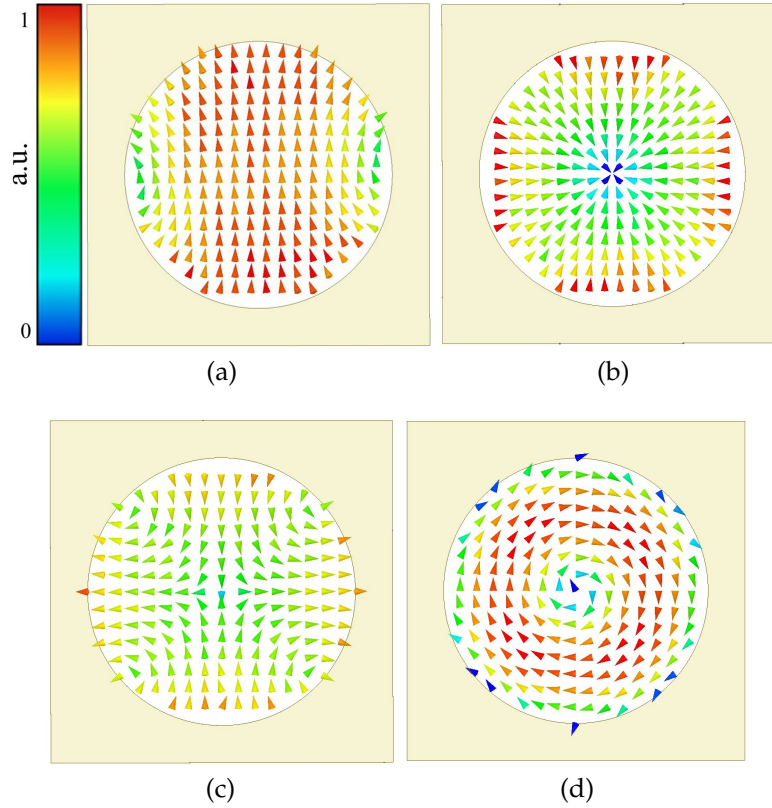
FIGURE 3.2: The distribution and magnitude (shown through colors) of total electric-field vectors of the four lowest-order modes of a circular aperture in a conducting screen: (a) TE_{11}, (b) TM_{01}, (c) TE_{21}, and (d) TE_{01}.

are the TE_{11}, TM_{01}, TE_{21}, and TE_{01} modes, respectively.

Obtaining the resonance frequencies of an inhomogeneously filled circular aperture, however, requires more complicated calculations. Here, the resonance frequency of a circular aperture in a conducting screen partially filled with a liner possessing anisotropic permittivity and permeability parameters will be obtained first, which will be then simplified for the case of the MTM liner shown in Fig. 3.1(a), which is assumed to possess an isotropic permittivity and a non-magnetic response. In general, longitudinal electric and

magnetic field vectors (E_z and H_z) in cylindrically anisotropic media may be written as [172]:

$$E_z = (C_1 J_\nu(\gamma_\rho^\epsilon \rho) + C_2 Y_\nu(\gamma_\rho^\epsilon \rho)) cos(n\phi) e^{(-\gamma z)} \tag{3.2a}$$

$$H_z = (C_3 J_\tau(\gamma_\rho^\mu \rho) + C_4 Y_\tau(\gamma_\rho^\mu \rho)) sin(n\phi) e^{(-\gamma z)} \tag{3.2b}$$

where J and Y are Bessel and Neumann functions, respectively, and γ is the complex propagation constant in the z direction, which will eventually be set to zero in order to find the resonance (cutoff) frequencies. n is the azimuthal mode index, and ν and τ are the (generally complex) orders of Bessel and Neumann functions, defined as $\nu = n\sqrt{\frac{\epsilon_\phi}{\epsilon_\rho}}$ and $\tau = n\sqrt{\frac{\mu_\phi}{\mu_\rho}}$, respectively, for $\gamma = 0$. γ_ρ^ϵ and γ_ρ^μ are the ρ-directed components of the propagation vector, which may be calculated as $\gamma_\rho^\epsilon = \omega\sqrt{\epsilon_z \mu_\phi}$ and $\gamma_\rho^\mu = \omega\sqrt{\mu_z \epsilon_\phi}$ at the resonance (i.e., cutoff) frequencies, and C_i coefficients are the excitation-dependent constants. A time-harmonic behavior ($e^{j\omega t}$) is assumed throughout these derivations. Further details of these derivations may be found in [172].

Using transverse decomposition of Maxwell's equations, the transverse electric and magnetic fields at the resonance frequencies may be written in terms of longitudinal E/H fields as:

$$E_\rho = -\frac{\gamma}{\gamma^2 + \omega^2 \epsilon_\rho \mu_\phi}\left(\frac{\partial E_z}{\partial \rho} + \frac{j\omega\mu_\phi}{\gamma\rho}\frac{\partial H_z}{\partial \phi}\right) \tag{3.3a}$$

$$E_\phi = -\frac{\gamma}{\gamma^2 + \omega^2 \epsilon_\phi \mu_\rho}\left(\frac{1}{\rho}\frac{\partial E_z}{\partial \phi} - \frac{j\omega\mu_\rho}{\gamma}\frac{\partial H_z}{\partial \rho}\right) \tag{3.3b}$$

$$H_\rho = -\frac{\gamma}{\gamma^2 + \omega^2 \epsilon_\phi \mu_\rho}\left(\frac{\partial H_z}{\partial \rho} - \frac{j\omega\epsilon_\phi}{\gamma\rho}\frac{\partial E_z}{\partial \phi}\right) \tag{3.3c}$$

$$H_\phi = -\frac{\gamma}{\gamma^2 + \omega^2 \epsilon_\rho \mu_\phi}\left(\frac{1}{\rho}\frac{\partial H_z}{\partial \phi} + \frac{j\omega\epsilon_\rho}{\gamma}\frac{\partial E_z}{\partial \rho}\right) \tag{3.3d}$$

The dispersion relation for the resonant modes of an MTM-lined circular aperture may be obtained through applying the appropriate boundary conditions. This includes enforcing the tangential electric fields to go to zero at the outer PEC boundary (i.e., $\rho = b$), as well as applying the continuity condition for tangential electric and magnetic field components between the MTM liner region and the inner vacuum region (i.e., at $\rho = a$), similar to the rigorous analysis in [172], resulting in:

$$A \cdot B = -\frac{K_0^2 n^2}{\gamma^2 a^2}\left[\frac{\mu_{\phi 2}\epsilon_{z2}}{(\gamma_{\rho 2}^\epsilon)^2} - \frac{\mu_{\phi 1}\epsilon_{z1}}{(\gamma_{\rho 1}^\epsilon)^2}\right]\left[\frac{\mu_{z2}\epsilon_{\phi 2}}{(\gamma_{\rho 2}^\mu)^2} - \frac{\mu_{z1}\epsilon_{\phi 1}}{(\gamma_{\rho 1}^\mu)^2}\right] \tag{3.4}$$

where,

$$A = \frac{\epsilon_{z1}}{\omega\sqrt{\epsilon_{z1}\mu_{\phi 1}}}\frac{J'_{\nu 1}(\omega\sqrt{\epsilon_{z1}\mu_{\phi 1}}a)}{J_{\nu 1}(\omega\sqrt{\epsilon_{z1}\mu_{\phi 1}}a)} - \frac{\epsilon_{z2}}{\omega\sqrt{\epsilon_{z2}\mu_{\phi 2}}}\frac{F'_{\nu 2}(\omega\sqrt{\epsilon_{z2}\mu_{\phi 2}}a)}{F_{\nu 2}(\omega\sqrt{\epsilon_{z2}\mu_{\phi 2}}a)} \tag{3.5a}$$

$$B = \frac{\mu_{z1}}{\omega\sqrt{\mu_{z1}\epsilon_{\phi1}}}\frac{J'_{\tau1}(\omega\sqrt{\mu_{z1}\epsilon_{\phi1}}a)}{J_{\tau1}(\omega\sqrt{\mu_{z1}\epsilon_{\phi1}}a)} - \frac{\mu_{z2}}{\omega\sqrt{\mu_{z2}\epsilon_{\phi2}}}\frac{G'_{\tau2}(\omega\sqrt{\mu_{z2}\epsilon_{\phi2}}a)}{G_{\tau2}(\omega\sqrt{\mu_{z2}\epsilon_{\phi2}}a)} \tag{3.5b}$$

in which

$$F_{v2}(\gamma^{\epsilon}_{\rho2}\rho) = Y_{v2}(\gamma^{\epsilon}_{\rho2}b)J_{v2}(\gamma^{\epsilon}_{\rho2}\rho) - J_{v2}(\gamma^{\epsilon}_{\rho2}b)Y_{v2}(\gamma^{\epsilon}_{\rho2}\rho) \tag{3.6a}$$

$$G_{\tau2}(\gamma^{\mu}_{\rho2}\rho) = Y'_{\tau2}(\gamma^{\mu}_{\rho2}b)J_{\tau2}(\gamma^{\mu}_{\rho2}\rho) - J'_{\tau2}(\gamma^{\mu}_{\rho2}b)Y_{\tau2}(\gamma^{\mu}_{\rho2}\rho) \tag{3.6b}$$

For the isotropic liner shown in Fig. 3.1(a) with a non-magnetic response, equation 3.4 reduces to:

$$A \cdot B = (\frac{\gamma n}{\omega a})^2(\frac{1}{K^2} - \frac{1}{k_0^2})^2 \tag{3.7}$$

where,

$$A = \frac{\epsilon_0}{k_0}\frac{J'_n(k_0a)}{J_n(k_0a)} - \frac{\epsilon_0\epsilon_r}{k}\frac{F'_n(ka)}{F_n(ka)} \tag{3.8a}$$

$$B = \frac{\mu_0}{k_0}\frac{J'_n(k_0a)}{J_n(k_0a)} - \frac{\mu_0}{k}\frac{G'_n(ka)}{G_n(ka)} \tag{3.8b}$$

and

$$F_n(k\rho) = Y_n(kb)J_n(k\rho) - J_n(kb)Y_n(k\rho) \qquad (3.9a)$$

$$G_n(k\rho) = Y_n'(kb)J_n(k\rho) - J_n'(kb)Y_n(k\rho) \qquad (3.9b)$$

in which $k_0 = \omega\sqrt{\mu_0\epsilon_0}$ is the free-space propagation constant. Equation 3.7 reduces to two separate equations at cutoff (i.e., $\gamma = 0$), each of which determine the resonance (cutoff) frequencies of a certain set of modes. The roots of (3.8a) determine the resonance (cutoff) frequencies of EH modes, while the roots of (3.8b) determine those of HE modes. Therefore, HE_{nm}-mode resonances (cutoffs) can be obtained from the following characteristic equation:

$$\frac{J_n'(k_0 a)}{J_n(k_0 a)}) = \frac{1}{\sqrt{\epsilon_r}}\frac{G_n'(k_0\sqrt{\epsilon_r}a)}{G_n(k_0\sqrt{\epsilon_r}a)} \qquad (3.10)$$

In fact, the solutions of (3.10) reveal a spectrum of HE modes whose resonance frequencies are a function of the MTM liner's permittivity. Since the fundamental mode of the empty circular aperture is TE_{11}, this work focuses on the corresponding HE_{11} mode. Figure 3.1(b) shows the relationship between the HE_{11} mode's resonance frequency and the MTM liner's relative permittivity, (solid black curve). The representative circular aperture investigated has physical dimensions $b = 15.65$ mm and $a = 13.69$ mm. These dimensions were chosen to place the resonance at microwave frequencies. Indeed, when $\epsilon_r = 1$, the

mode's resonance frequency reverts to that of a homogeneously vacuum-filled aperture, namely $f = 5.613$ GHz. As ϵ tends to large values, the resonances are only marginally reduced, which is to be expected by partially filling an aperture with a high-permittivity dielectric. More interestingly, as $\epsilon \to 0$, dramatic shifts are observed in the resonance frequency: whereas ϵ-positive and near-zero (EPNZ) values strongly increase the resonance frequencies, ENNZ values strongly reduce them. A reduced cutoff frequency implies a miniaturized aperture. However, to realize these desired ENNZ values, material dispersion must be taken into account. To this end, the liner's permittivity is assigned a lossless Drude profile with $(\epsilon_r(f) = 1 - f_{ep}^2/f^2)$, in which $f_{ep} = 2.6$ GHz is the assigned plasma frequency. The dashed blue curve in Fig. 3.1(b) shows the defined Drude profile, in which two intersections with the resonance-frequency curve can be observed: the lower intersection at 2.41 GHz corresponds to the frequency-reduced HE_{11}-mode resonance for which $\epsilon_r = -0.1654$, and the upper intersection at $f = 5.696$ GHz is akin to the conventional TE_{11}-mode resonance except that $\epsilon_r = 0.7916$ instead of unity. For MTM-lined CWGs, the lowered resonance established the cutoff frequency of a frequency-reduced backward-wave passband in which the CWG exhibited strong transmission [2] and its open-ended variant produced radiation from the fundamental HE_{11}-mode [173]. Both phenomena were enabled by the ENNZ MTM liner well below the CWG's natural cutoff. In analogy, an aperture in a PEC screen lined using ENNZ MTMs exhibits a strongly

frequency-reduced fundamental-mode resonance, which describes the onset of a continuous radiation spectrum that may be predicted by conventional aperture-antenna theory. In should be noted that conventional empty apertures only resonate when they are electrically large, while the MTM-lined apertures studied here can be made to resonate even though they are electrically small, and are nearly empty.

To this point, the MTM liner was treated as an effective medium with isotropic and homogeneous permittivity. However, MTMs are often anisotropic in practice. Therefore, it is necessary to study the behavior of a practical implementation of MTMs used to line the apertures. In the microwave regime, negative permittivities are easily obtained using arrays of thin wires which exhibit a Drude-like permittivity dispersion for electric fields aligned parallel to the wire axes [73]. Thin wires are a common implementation of negative permittivities at low frequencies, and can be easily fabricated using printed circuit techniques. To interact with the electric-field polarizations of the HE_{11} mode, a printed-circuit implementation based on azimuthally and radially directed copper traces that are loaded using discrete inductors in the radial direction and capacitive gaps in the azimuthal direction was presented in [173]. The thin wire media, when unloaded, do not provide the strong inductances required to achieve ENNZ properties. This can be attributed to the finite size of copper traces in the ρ and ϕ directions. The addition of discrete loading inductors in the ρ-direction causes a strong reduction of the effective plasma

frequency. The main purpose of the ϕ-directed capacitive gaps symmetrically placed between each two inductors is to avoid the unwanted resonances in the azimuthal direction. This practical implementation is anisotropic and can be homogenized using an anisotropic effective permittivity tensor. However, the dispersion features studied through full-wave eigenmode simulations demonstrate that similar dispersion characteristics and miniaturization properties to those of an isotropic homogeneous liner can be achieved through this anisotropic MTM liner, providing the appropriate choice of geometrical parameters and loading elements [173].

3.3 MNNZ MTM-Lined Discs

According to Babinet's principle, dual/complementary arrays are expected to demonstrate complementary transmission/reflection behaviour [30]. That is, the reflection spectrum of one would resemble the transmission spectrum of the other, and vice versa. This property is applied to the ENNZ-lined circular apertures presented above, and an array of miniaturized μ-negative and near-zero (MNNZ)-lined metallic discs is obtained. Presented studies show that the resonance frequency of the fundamental mode of an MNNZ-lined circular metallic disc can be reduced in a similar manner to ENNZ-lined circular apertures in a metallic screen.

Figure 3.3 shows the MNNZ-lined disc geometry, possessing an inner metal region of radius a surrounded by an outer MTM region of thickness $b - a$ that exhibits a dispersive
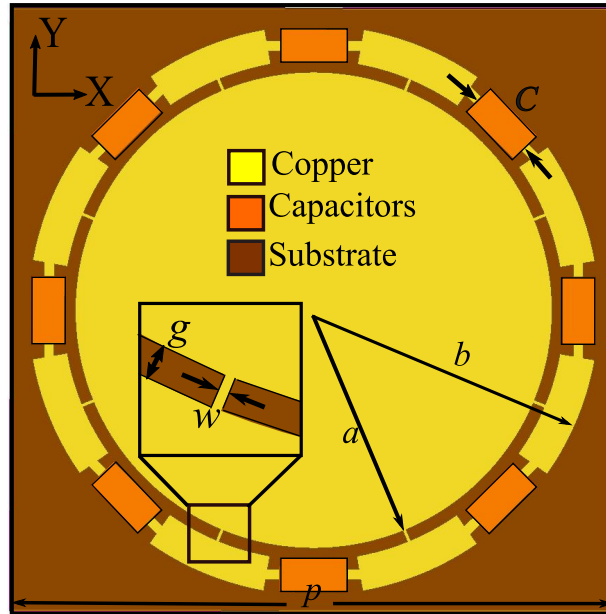
FIGURE 3.3: The practical, MNNZ-lined metallic disc unit cell design possessing a complementary structure compared to the ENNZ-lined aperture shown in Fig. 3.1(c)

relative permeability and nonelectric response. This practical MTM liner design possesses a printed-circuit-board (PCB) implementation, and is obtained by interchanging the metal and vacuum/dielectric regions of the aperture design shown in Fig. 3.1(c), and replacing the discrete, radially directed loading inductors with discrete, *azimuthally* directed capacitors, which affect the MNNZ response.

As the studies in chapter 4 and 6 will show, the response of the MNNZ-Lined disc unit cell is the dual of that of the ENNZ-lined aperture design; that is, the presence of an MNNZ liner reduces the resonance frequency of the metallic disc in the same way that the ENNZ liner loading reduces the resonance frequency of an aperture. Therefore, this MNNZ-lined disc supports hybrid electric (HE) and magnetic (EH) resonant modes.

Similar to the ENNZ-lined apertures, the amount of capacitive loading determines the effective permeability of the liner, including its MNNZ frequency regime, and therefore, the degree of miniaturization. While apertures show increased transmission at resonance, with a Fano lineshape exhibiting a maximum followed by a minimum, the discs show a Fano-shape reflection behaviour at resonance. These results are shown in subsequent chapters (chapter 4 shows the scattering parameters of the ENNZ-lined apertures, while the scattering parameters of the MNNZ-lined discs are presented in chapter 6). Generally, The Fano-shape of the transmission/reflection parameter is known to be caused by constructive and destructive interference of different scattering mechanisms [174]: one resonant (also called discrete) and one or more nonresonant (also called continuous or flat). In this work, the reduced resonance of the aperture/disc provides the resonant mechanism, while the nonresonant mechanism can be provided by the incident electromagnetic wave and/or the higher order modes that weakly exist in the near-field of the resonator, causing complex near-field patterns [175]. Further understanding of the origin of this lineshape requires rigorous mode-matching studies, which was out of the scope of this work.

Transmission-line (TL) models are presented for the ENNZ/MNNZ MTM liners in the next section, and will be used in the next chapters to validate the ENNZ/MNNZ behaviour of the utilized MTM liners.
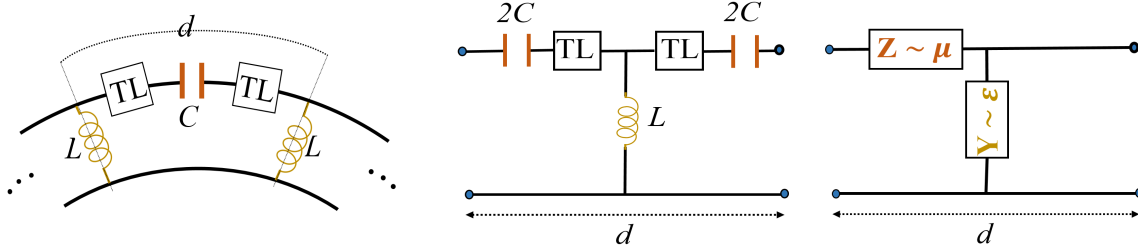
FIGURE 3.4: Evolution of the *L*-*C*-loaded TL model for the ENNZ/MNNZ liners, similar to that shown for ENNZ liners in [176].

3.4 TL Studies of MTM Liners

The practical ENNZ and MNNZ liner implementations presented in figures 3.1(c) and 3.3, respectively, can be viewed as an azimuthally directed transmission lines (as was done in [176]) periodically loaded using series capacitors (C) and shunt inductors (L), as shown in Fig. 3.4. This model is applicable to both liner implementations, although only one of the two loadings need to be strong for obtaining the desired ENNZ or MNNZ property, as will be discussed below.

In the ENNZ-lined aperture design, L refers to the discrete, radially directed loading inductors and C refers to the capacitance introduced through azimuthally directed gaps (g) in the inner ring. For the MNNZ-lined disc design, the label C refers to the discrete, azimuthally directed loading capacitors and L refers to the inductance introduced by the radial stubs of width w. The well-known negative-refractive-index transmission-line (NRI-TL) theory can therefore be used to extract the effective permittivity/permeability response of these MTM liners [177]. This extraction is shown below for each MTM liner.
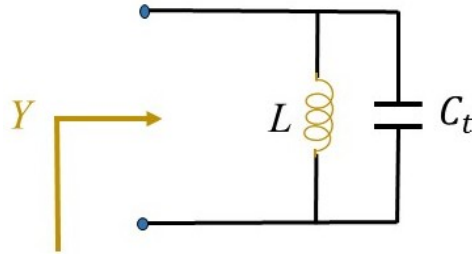
FIGURE 3.5: Shunt branch of the TL model shown in Fig. 3.4, representing the shunt loading inductor, and a parallel capacitor caused by the intrinsic TL capacitance plus the parasitic capacitance introduced by the loading inductor (if present).

3.4.1 Effective Permittivity and Electric Plasma Frequency of the ENNZ Liner

It was discussed in [177] that the electric plasma frequency (i.e., f_{ep}) of the proposed L-C-loaded TL model is equal to the resonance frequency of an equivalent parallel L-C circuit representing the shunt branch, as exhibited in Fig. 3.5. In this model, inductance is introduced by the shunt inductive loading shown in yellow in Fig. 3.4 (i.e., L), and capacitance (C_t) is introduced by the intrinsic TL capacitance plus the parasitic capacitive effects added by the lumped inductive loading, if present. This parasitic capacitance is particularly important for fully printed dual-arm spiral inductors that will be introduced in this work, as they are realized through closely spaced printed traces and gaps, and the gaps would introduce parasitic capacitive effects. The total capacitance may be called C_t.

For this parallel *L-C* circuit, the admittance can be written as follows [178]:

$$Y = j\omega C_t - \frac{j}{\omega L}.$$ (3.11)

The above equation does not allow the isolation of L in terms of Y, as C_t is also unknown. However, if $\frac{\partial Y}{\partial \omega}$ is obtained and subtracted from equation (3.11), an equation only in terms of L, Y and its derivative is obtained:

$$Y - \omega \frac{\partial Y}{\partial \omega} = -\frac{2j}{L\omega}$$ (3.12)

and therefore, L can be calculated as:

$$L = -\frac{2j}{\omega(Y - \omega \frac{\partial Y}{\partial \omega})}.$$ (3.13)

By inserting (3.13) in (3.12), C_t may also be obtained as:

$$C_t = \frac{Y + \frac{j}{\omega L}}{j\omega}$$ (3.14)

implying

$$f_{ep} = \frac{\omega}{2\sqrt{2}\pi} \sqrt{\frac{\omega \frac{\partial Y}{\partial \omega} - Y}{Y + \frac{j}{\omega L}}}$$ (3.15)
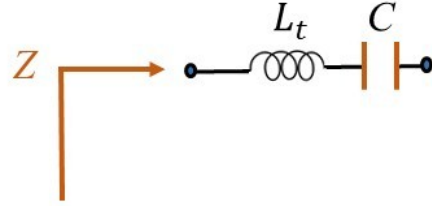
FIGURE 3.6: Series branch of the TL model shown in Fig. 3.4, representing the series loading capacitor and a series inductor introduced by the intrinsic TL inductance plus the parasitic inductance of the loading capacitor (if applicable).

where ω is the angular frequency. Furthermore, ϵ_r may be calculated from the parallel L-C circuit using the following formula:

$$\epsilon_r = \frac{Yg}{j\omega\epsilon_0 d} \tag{3.16}$$

where d is the periodicity of the loaded TL model in the azimuthal direction, and the geometrical factor g is a scalar quantity representing the effect of the 2D arrangement and electrical properties of TL conductors and dielectrics on its per-unit-length parameters [177].

3.4.2 Effective Permeability and Magnetic Plasma Frequency of the MNNZ Liner

The magnetic plasma frequency (f_{mp}) of the proposed L-C-loaded TL model may be calculated in a similar manner as above. In fact, f_{mp} is equal to the resonance frequency of an equivalent series L-C circuit representing the series branch, as shown in Fig. 3.6. In this

model, capacitance is introduced by the lumped capacitive loading shown in brown in Fig. 3.4 (i.e., *C*), and inductance is caused by the intrinsic TL inductance plus the parasitic inductive effects added by the loading capacitor, if any. These parasitic effects need to be taken into account for the case of fully printed interdigitated capacitors that will be used in this work. The total inductance may be named L_t. For the series *L-C* circuit shown in Fig. 3.6, the overall impedance can be written as follows [178]:

$$Z = j\omega L_t - \frac{j}{\omega C}. \tag{3.17}$$

Once again, $\frac{\partial Z}{\partial \omega}$ should be calculated and subtracted from Z, so that an equation only containing C, Z and its derivative is obtained:

$$Z - \omega\frac{\partial Z}{\partial \omega} = -\frac{2j}{C\omega} \tag{3.18}$$

and therefore, C can be obtained as:

$$C = -\frac{2j}{\omega(Z - \omega\frac{\partial Z}{\partial \omega})}. \tag{3.19}$$

L_t may also be calculated as:

$$L_t = \frac{Z + \frac{j}{\omega C}}{j\omega} \tag{3.20}$$

implying

$$f_{mp} = \frac{\omega}{2\sqrt{2}\pi} \sqrt{\frac{\omega\frac{\partial Z}{\partial \omega} - Z}{Z + \frac{j}{\omega C}}}.$$ (3.21)

Consequently, μ_r may be calculated from the series *L-C* circuit using the following for-

mula:

$$\mu_r = \frac{Z}{j\omega\mu_0 gd}$$ (3.22)

where definitions of ω, d and g are same as sec. 3.4.1.

Chapter 4

Metascreen Based on ENNZ-Lined Apertures Designed for Obtaining ET at Microwave Frequencies

In chapter 3, the mechanism of reduced-frequency resonance in miniaturized circular apertures in a metallic screen by means of applying thin ϵ-negative and near-zero (ENNZ) metamaterial (MTM) liners was described. In this chapter, a novel approach is offered for extraordinary transmission (ET) based on this analogy. ET through a periodic array of sub-wavelength apertures on a perfect metallic screen has been studied extensively in recent years, and has largely been attributed to diffraction effects, for which the periodicity of the apertures, rather than their dimensions, dominates the response. Therefore, although apertures/slits are subwavelength in conventional ET devices, the arrays are not com-pact as spacings are on the order of one wavelength. The transmission properties of the

apertures at resonance, on the other hand, are not typically considered 'extraordinary' because they may be explained using more conventional aperture-theoretical mechanisms. Furthermore, resonant apertures are typically electrically large ($\sim \lambda/2$) and lie in the frequency selective surface (FSS) operating regime. This work describes a novel approach for achieving ET through a metascreen design in which subwavelength apertures are made to resonate by lining them using thin, ENNZ MTMs. The use of ENNZ MTMs has proven successful in miniaturizing circular apertures by strongly reducing their natural resonance frequencies as presented in chapter 3. The theory is adopted in this chapter for the design of identical subwavelength apertures in a metallic screen. We present simulations and measurements at microwave frequencies that demonstrate ET for apertures measuring one-quarter of a wavelength in diameter and suggest the potential for further miniaturization simply by engineering the ENNZ MTM liner's dispersion. The results exhibit a Fano-like transmission profile (i.e., a maximum in transmission followed by a minimum) whose frequency varies with the properties of the MTM liner, but is independent of period. This suggests that the apertures can be closely spaced, resulting in a compact device.

4.1 Numerical Investigations of ENNZ-Lined Circular Apertures

4.1.1 Transmission Studies

Although the theory presented in chapter 3 discussed the miniaturization of a single ENNZ-lined aperture, this aperture needs to be used in an array to provide an appreciable level of transmission in the reduced resonance regime. Moreover, an array of apertures provides better control over the incident electromagnetic waves as the apertures interact with the incoming waves over a larger spatial area. Figure 3.1(c) shows a representative unit cell of a periodic MTM-lined aperture array designed for placing the reduced resonance (cutoff) frequency at 2.4 GHz. This printed-circuit implementation for the ENNZ MTM liner has an inner radius a (13.69 mm), outer radius b (15.65 mm), aperture period p (40 mm), trace width w (0.45 mm), and gap size g (0.1 mm). In this design, Coilcraft 0908-12N air-core, wire-wound inductors were chosen, which have an inductance of $L = 14.61$ nH and a quality factor of $Q = 463$ at $f = 2.4$ GHz. These design parameters were chosen to achieve a Drude-like ENNZ response similar to that of an isotropic homogeneous liner shown in Fig. 3.1(b).

An aperture in a PEC screen lined using ENNZ MTMs exhibits a strongly frequency-reduced fundamental-mode resonance, which causes a maximum in radiation that may be predicted by conventional aperture-antenna theory. In this work, ET is achieved for

nearly-empty apertures that are simultaneously subwavelength and resonant, at frequencies which are determined by the aperture and liner properties and which are independent of period.

The unit cell previously described and depicted in Fig. 3.1(c) is used here to build an infinite array of apertures, by means of applying periodic boundary conditions to the transverse boundaries of the model. The screen containing the apertures is chosen to be Rogers/Duroid 5880 substrate (ϵ_r = 2.2, $tan\delta$ = 0.0009) of 1.55 mm thickness, which is metallized on one side by gold-immersed copper. This design was simulated using Ansoft's HFSS, a full-wave, finite-element-method simulator, in which all practical losses, including conductor and dielectric losses, are included.

Figure 4.1 presents the scattering (S-) parameters for an infinite array of both the MTM-lined apertures and unlined apertures of the same outer radius illuminated using a normally incident plane wave. It is worth noting that this unit cell exhibits negligible polarization sensitivity at normal incidence, due to its symmetry as well as the fact that the azimuthal periodicity is much smaller than a wavelength, allowing a homogenized perspective. Since these frequencies are far below the first grating anomalies (7.5 GHz – more details to be presented later in this section) and occur where copper is effectively a PEC, the unlined apertures are not expected to exhibit ET. Indeed, the unlined aperture's transmission (dashed magenta curve) and reflection (dashed green curve) do not show any resonant behaviour. However, introduction of the printed-circuit ENNZ MTM

(a)

(b)
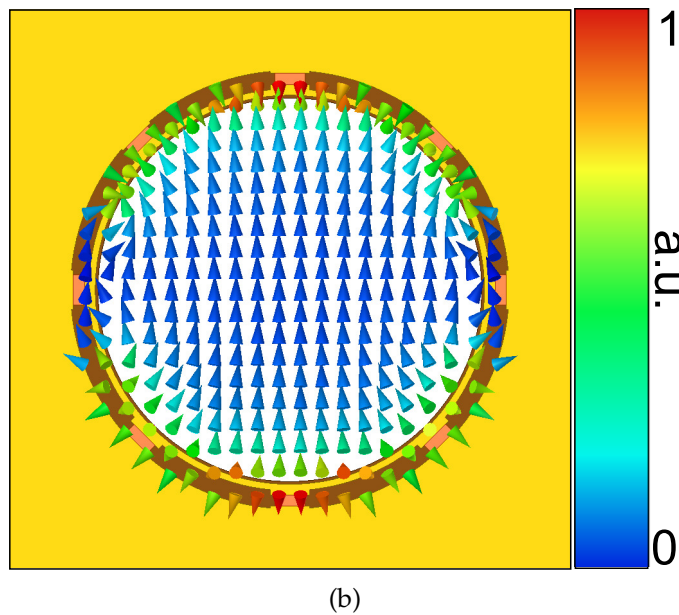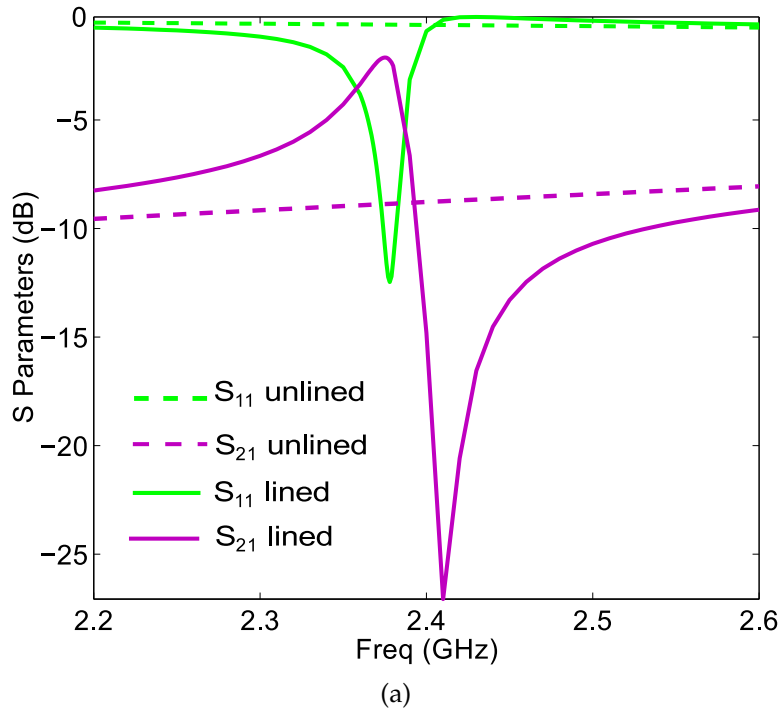
FIGURE 4.1: (a) The scattering parameters for an infinite array of ENNZ MTM-lined and unlined apertures with periodicity $P = 40$ mm. (b) Simulated normalized complex electric field vectors corresponding to the HE_{11}-mode resonance at $f = 2.37$ GHz

liner dramatically changes the response. The transmission profile (solid magenta curve) exhibits a Fano lineshape, where the transmission peak of -2.12 dB at $f = 2.37$ GHz is followed by a distinct antiresonance achieving -27 dB at $f = 2.41$ GHz. The transmission peak demonstrates a 6.77 dB improvement over that of the unlined apertures, which suggests the occurrence of ET. These data also imply insertion losses as low as 2 dB. While this particular design exhibits ET for aperture diameters of $\lambda/4$, it should be noted that using stronger inductance values would enable even further miniaturization by further depressing the plasma frequency of the Drude ENNZ response and lowering the corresponding intersection frequency in Fig 3.1(b). It is noteworthy to mention that at the antiresonance frequency, the MTM-lined apertures offer up to 18.25 dB better shielding properties than the unlined screen. This may enable their use for narrow-band shielding or filtering applications, which for this design would occur most usefully in the ISM band ($2.400 - 2.4835$ GHz). At optical frequencies, Fano profiles with such a high contrast ($\sim 25\, dB$) are highly advantageous in lasing, switching, nonlinear and slow-light devices, and the design of high-sensitivity sensors [175].

Figure 4.1(b) presents the normalized transverse electric-field vectors inside the aperture at $f = 2.37$ GHz. The electric fields exhibit an HE_{11}-mode pattern inside the aperture, which features a collimation of the electric fields in the vacuum region and a higher discontinuous field concentration in the liner region. Notably, the normal components of the electric-field vectors change direction at the vacuum-liner interface, which further
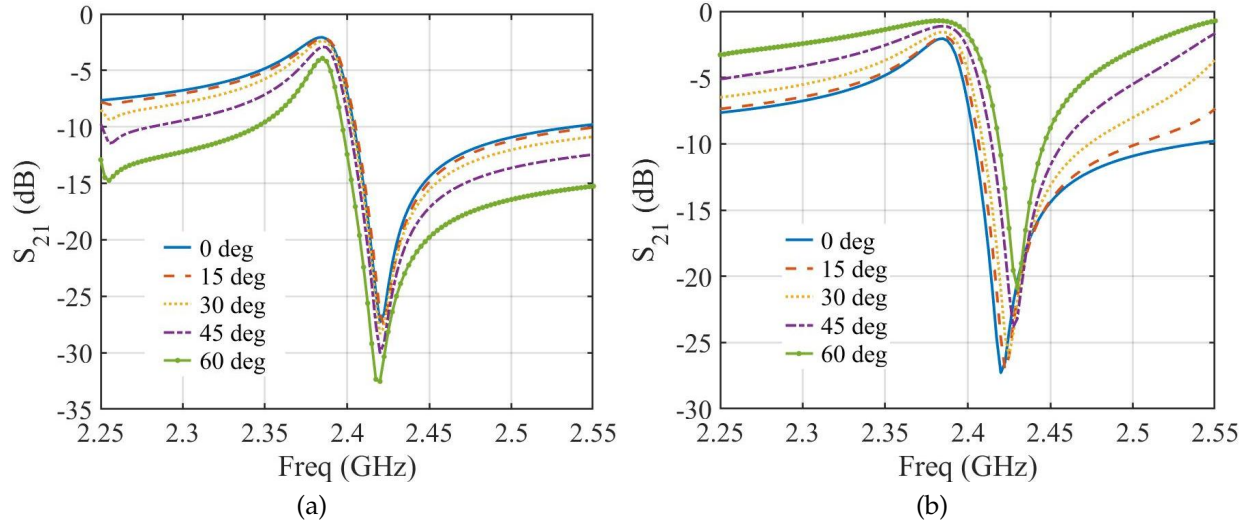
FIGURE 4.2: Transmission (S_{21}) versus incident angle through the ENNZ MTM-lined aperture possessing the nominal parameters presented in section 4.1.1 for (a) TE and (b) TM polarizations of incidence.

validates its ENNZ response. These phenomena become more prominent and more extreme with higher degrees of miniaturization, which, as previously mentioned, could be achieved through stronger inductive loading [2].

4.1.2 Oblique Incidence Studies

Figure 4.2 presents the angular dependence of the transmission (S_{21}) through the ENNZ-lined aperture array for both TE- and TM polarizations of incident wave as their incident angle is swept from $0°$ to $75°$. In both cases, the level of transmission gradually changes as the angle increases towards grazing incidence, but the resonance frequency remains unchanged. Stable response with respect to the angle of incidence is owed to the miniaturization of the unit cells, as well as the fact that transmission mechanism in this work

does not rely on diffraction effects.

4.1.3   Parametric Studies

To verify that the mechanism of ET is strongly tied to the resonance of the aperture, the following parametric studies are presented: Figure 4.3(a) presents the transmission through the array as the aperture period varies. Similar to the angle dependence, the transmission's resonance and antiresonance frequencies do not change, but the level of transmission decreases. In this case, this is attributed to the reduction in the density of apertures in the screen, which, in the language of aperture-antenna theory, implies a reduction in the directivity. These two studies suggest that the transmission resonance and antiresonance frequencies are only weakly dependent on the interaction between the apertures.

Two possible methods to control the resonance frequency of the printed-circuit MTM-lined aperture are 1) through altering the loading inductance (L) and 2) by varying the trace width (w). Figures 4.3(b) and 4.3(c) present the transmission through the array as L and w are increased. In both cases, the HE_{11} mode's resonance decreases, which leads to an observed downshift in the transmission resonance and antiresonance frequencies. This emphasizes that the aperture's resonance plays a dominant role in the ET. Furthermore, it highlights that L and w are two design variables that may be used to control the frequency locations of the ET resonance and antiresonance. However, it should be understood that the use of higher-valued inductors is typically accompanied by lower quality
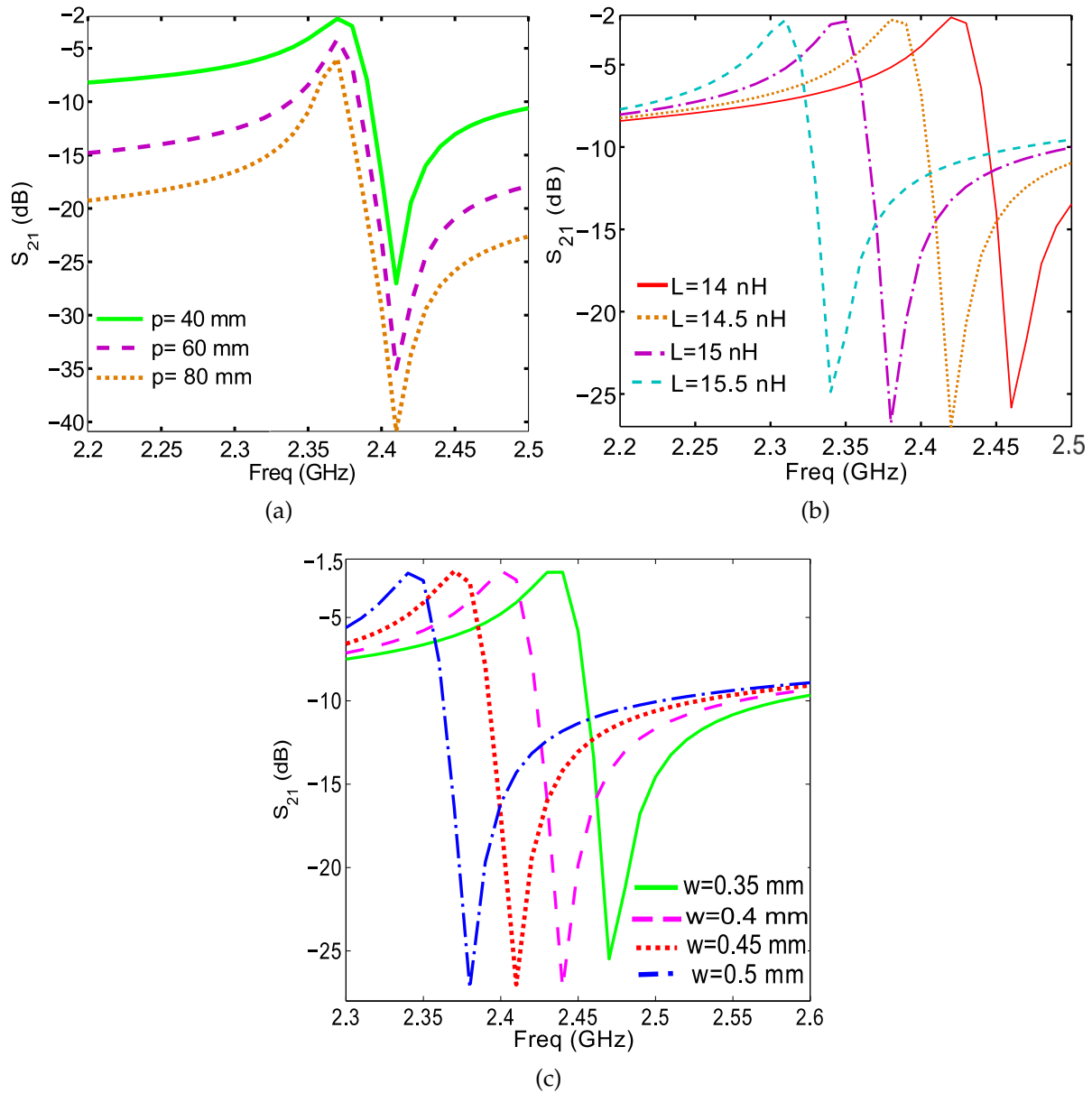
FIGURE 4.3: Transmission (S_{21}) through the ENNZ MTM-lined aperture array as (a) periodicity (P), (b) loading inductance (L), and (c) trace width (w) are varied
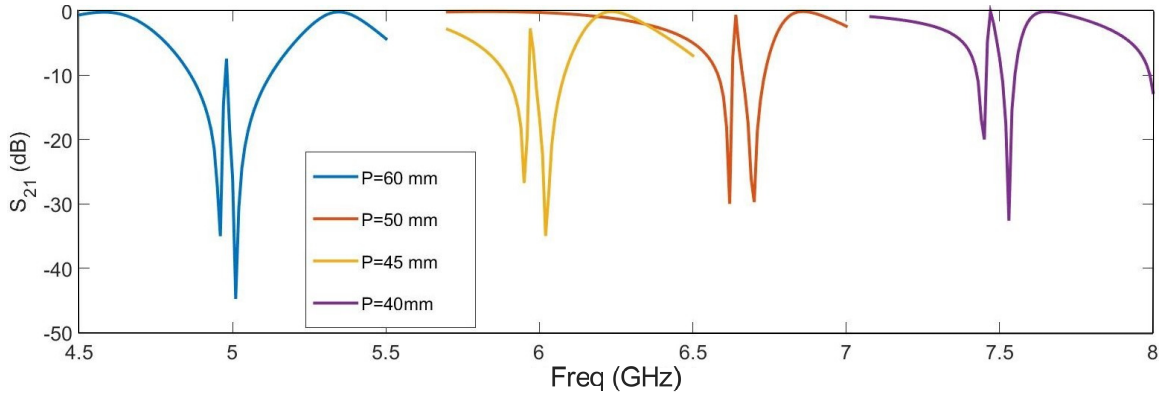
FIGURE 4.4: Transmission through an array of ENNZ-lined apertures near the Wood-Rayleigh anomaly, as periodicity (*P*) is varied.

factors, which would lead to decreased levels of transmission.

To further confirm the difference between ET mechanism presented here and periodicity-based ET, we have looked at the transmission behavior of our designed array at the transmission frequencies expected by Wood-Rayleigh anomalies. Since $P = 40$ mm, this sort of transmission peak is expected to occur at 7.5 GHz. Simulating the designed array at higher frequency regimes in fact shows the existence of periodicity-based ET at 7.5 GHz, whose frequency varies with (even incremental) changes in P, as expected, and shown in Fig. 4.4.

4.2   Fabrication and Measurement

Whereas traditional approaches to ET have required very large arrays of apertures [179], the insensitivity of the proposed ET approach to periodicity has the distinct advantage of allowing more compact structures. Hence, Fig. 4.5(a) presents the fabricated prototype of

a 5 by 5 uniform array of printed-circuit MTM-lined apertures. The apertures share the same geometrical and electrical parameters as presented in the simulation section, and the resulting screen has outer dimensions of 308 mm by 308 mm. A single fabricated aperture is shown in Fig. 4.5(b). Although not shown, a similar screen of unlined holes of the same radius ($b = 15.65$ mm) is fabricated as a reference case. The front side of the screen is illuminated using a shielded-loop probe antenna placed 16 mm from the screen's face, which produces magnetic-dipole-like fields. This distance corresponds to a numerical aperture of 0.995 which mitigates the effects of finite size and minimizes the diffraction from the edges. The fields transmitted by the screen are sampled using a WR-430 open-ended waveguide (OEWG) probe connected to an automated nearfield scanner inside a shielded anechoic chamber and a Keysight Technologies PNA-X N5244A network analyzer. Figure 4.6 shows the experimental setup. Extruded foam panels that are transparent at microwave frequencies are fixed to the outer edge of the screen to provide rigid support.

This experimental setup was used to measure the directivity of the screen through a scan of the electromagnetic near-fields over a cylindrical window. The near-fields obtained by the OEWG are first probe-corrected and then used to calculate the far-fields via a Fourier transform, which yields the radiation pattern and directivity. However, the cylindrical near-field window is limited by the height of the anechoic chamber and therefore is

(a)   (b)
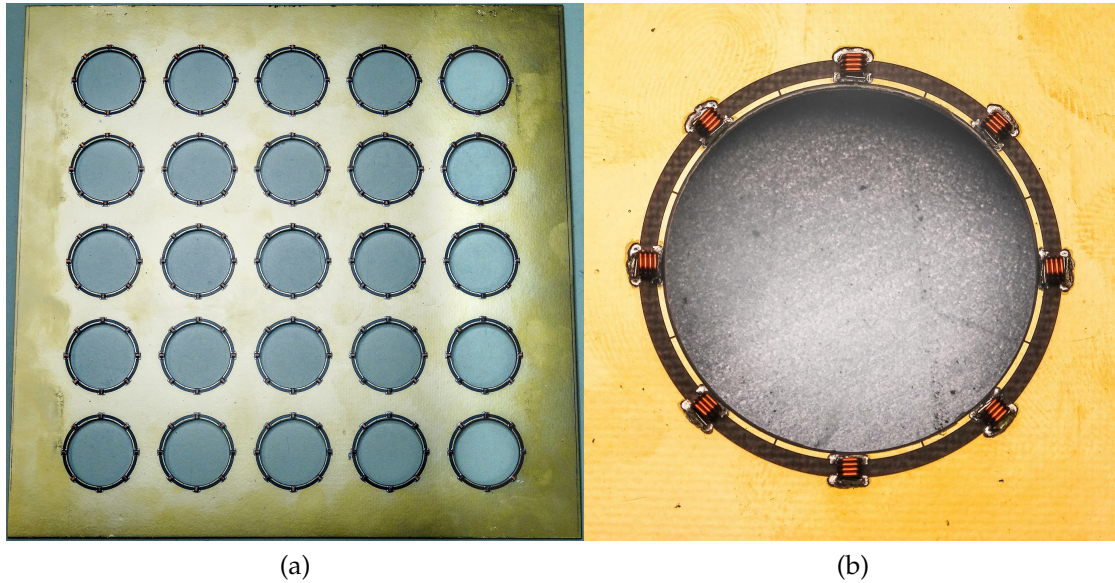
FIGURE 4.5: The (a) 5×5 array and (b) single unit cell of the fabricated proto-
type ENNZ MTM-lined apertures.
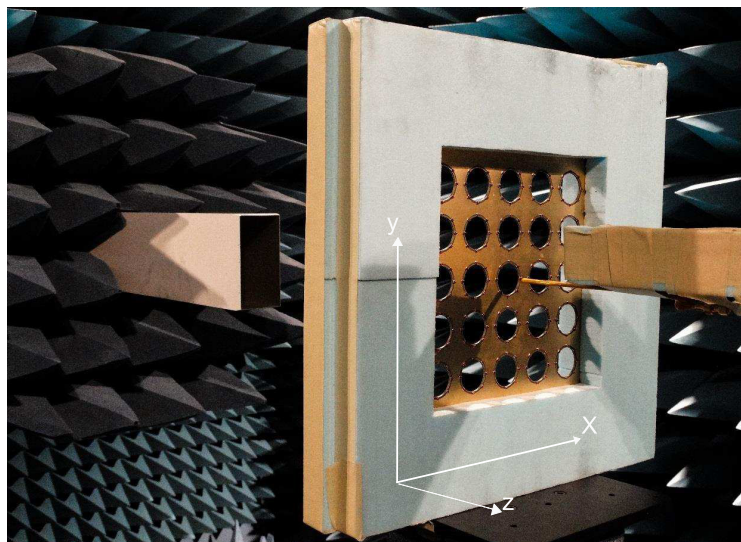
FIGURE 4.6: The experimental setup inside the shielded anechoic cham-
ber used to measure the far-field directivity. Shown is the ENNZ MTM-
lined aperture screen placed between the transmitting shielded-loop antenna
(right) and the receiving OEWG probe (left).

unable to capture all of the radiated power. As a result, the raw measured directivity values are not meaningful. Instead, the measured broadside directivities (directivities along the Z axis) of both the MTM-lined and unlined screens are normalized to the former, so that the overall maximum is at 0 dB, and the relative difference in values and trends may be evaluated. Also, since the screen measured here is finite in size, the measured directivity cannot be expected to match the scattering parameters presented in the previous section for the infinite screen, except in the general trend and frequency location of the transmission peak. To enable a comparison between experimental results and simulation, an identical 5 by 5 array of MTM-lined apertures is also simulated using HFSS, and the resulting simulated directivity is normalized in the same fashion.

The results are presented in Fig. 4.7, with solid curves representing the measured data, and dashed/dotted curves presenting the simulated directivities. Some broadening in the peak and antiresonance relative to the previous S-parameter data is observed in both experimental results (solid magenta curve) and simulation data (dotted blue curve), which may be expected due to the finite size of the screen but also due to illumination using a point-like source, which excites the aperture array nonuniformly. The data exhibit a distinct resonance and antiresonance, with the resonance providing more than 6 dB improvement in transmission over the unlined case. The measured antiresonance also shows up to 18 dB better shielding compared to that of the unlined holes. Although these trends in the measured results prove to be consistent with simulation, there is an apparent down- (red-)
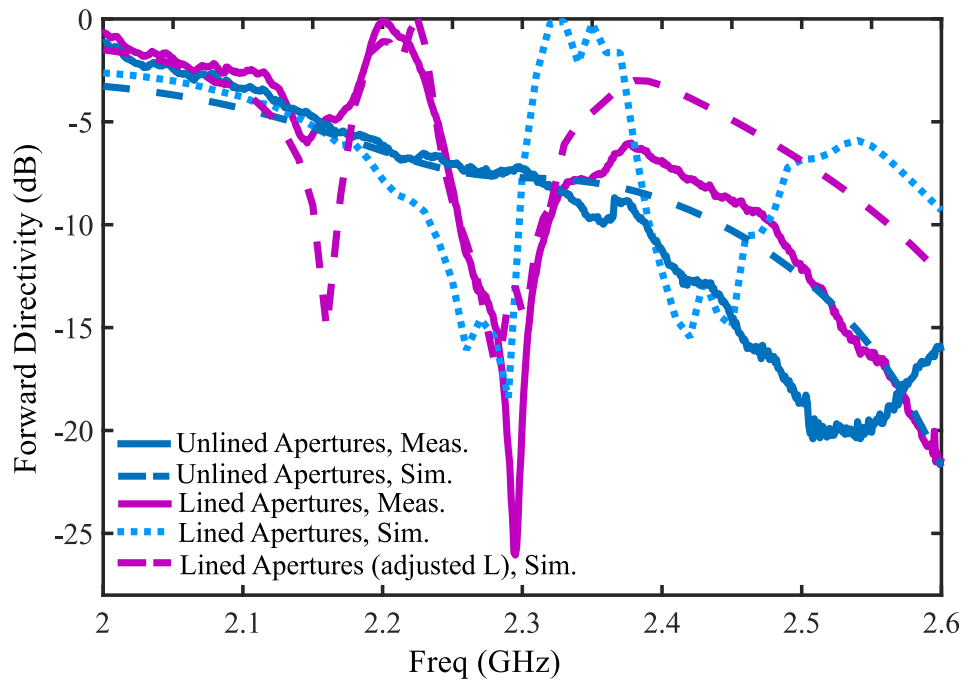
FIGURE 4.7: The measured and simulated broadside directivity of the ENNZ MTM-lined and unlined aperture screens. The simulation result employing an adjusted inductor value of $L = 15.4$ nH is also shown.

shift in the measured peak and antiresonance frequencies. This may be attributed largely to the inductors used in fabrication, which possess a 2 percent tolerance. Furthermore, soldering and the requirement for inductor pads may also contribute to a larger effective inductance value. Consequently, an upshift in the inductance values may be expected from the parametric study in Fig. 4.3(b) to cause a downshift in the peak frequency. In that study, it was observed that the peak frequency downshifted approximately linearly with increasing inductance value, at a rate of 80 MHz/nH. These data may be employed to estimate the effective inductance value (accounting for all fabrication and component tolerances) responsible for the experimentally observed redshift. Therefore, the simulation is repeated with a calculated effective inductance value of 15.4 nH (5.4% larger), and the updated results are shown in Fig. 4.7 in the dashed magenta curve. The agreement between these new data and the measured data âĂŞ particularly in the locations of the peak and antiresonance âĂŞ is evident, and validates the role of the larger effective inductance in causing a redshift. The remaining discrepancies between the measured and simulated data, particularly at high frequencies, may be attributed to the frequency dependence of both parasitic and the loading inductors, whose self-resonance frequency occurs above 3 GHz.

The screens discussed in this chapter generally fall into the category of MTSs or miniaturized-element FSSs, as they possess resonant elements. However, the fact that the elements possess subwavelength dimension and spacing suggests that their transmission may indeed

be considered "extraordinary", even moreso than the Wood-Rayleigh anomalies, as they rely on spacings that are on the order of one wavelength.

4.3 Applications

The proposed resonant metascreen structure possesses properties that may benefit many existing applications of ET and introduce other novel applications over a wide range of frequencies. At microwave/millimeter-wave frequencies, for instance, the combination of a high-contrast peak/antiresonance can be used to create novel partially reflecting surfaces for antennas, and the antiresonance can be employed for shielding or filtering of electromagnetic interference while still allowing visual accessibility through the empty apertures. Scaling the ENNZ liners to THz and optical frequencies could prove useful in achieving ET in optically thick screens that allow some degree of visual transparency through the apertures, particularly if they are densely arranged. Since the ENNZ liner can be made thin and only partially fills each aperture, such screens could be made permeable for optical sensing or characterization of fluids or biological materials. Moreover, the high-contrast Fano profile may be highly advantageous for applications such as lasing and optical switching. As mentioned, the proposed approach allows compact screens, and the peak/antiresonance locations are easily controlled using the aperture and liner properties.

Chapter 5

Far-field Magnification of Subdiffraction Conducting Features using MTM-Lined Aperture Arrays

Although chapter 4 studied arrays of identical subwavelength apertures with the purpose of achieving ET at microwave frequencies, inhomogeneous aperture arrays are also beneficial in a variety of applications. For example, they may be used to design superstrates for engineering the aperture magnitude and phase distributions of underlying antennas. In such applications, the use of miniaturized, densely packed apertures provides higher spatial resolution for shaping the radiation pattern of the underlying antenna. Here, we study a novel approach for imaging beyond the diffraction through the use of inhomogeneous miniaturized apertures that are densely packed at subwavelength intervals.

This chapter offers a new approach for far-field high-resolution imaging of conducting

obstacles based on arrays of frequency-multiplexed subwavelength resonant elements. The have been similar attempts in the past to perform imaging in a frequency-multiplexed scheme, an example of which is magnetic-resonance imaging (MRI) [180]. In this work, subdiffraction imaging is performed through a direct space-frequency map between the resonance frequency of an aperture and its location. The underlying idea in the imaging scheme used in this work (see, for example, [181, 182]) is that each location in the environment can be addressed by the unique resonance frequency in the transmission/reflection spectrum of a resonator placed at that location. Then, changes in the frequency response of this resonator array can be used to obtain information about objects at the corresponding resonator locations. Therefore, several resonators with different resonance frequencies are cascaded, where each resonator is a circular aperture in a metallic screen that is strongly miniaturized by means of loading by a thin ϵ-negative and near-zero (ENNZ) metamaterial (MTM) liner. Each MTM-lined aperture, as demonstrated earlier, exhibits a Fano-shape transmission profile, and the resonance frequencies of different apertures are chosen such that the resonance of one lies within/very close to the antiresonance of the other, to ensure strong decoupling. Multiple decoupled resonances are observed in the transmission spectrum of the resulting array, each corresponding to a particular resonator. It is shown that blocking an aperture using a conducting disc removes the corresponding resonance peak/minimum from the transmission/far-field amplitude spectrum, enabling

far-field detection of any distribution of such obstacles with a spatial resolution determined by the aperture sizes, which measure less than one-sixth of the free-space wavelength at their respective resonance frequencies (i.e., three times better than the constraint imposed by the diffraction limit, as discussed in sec. 2.6). The proposed imaging mechanism is verified through full-wave HFSS simulations as well as far-field measurements. Some challenges associated with this approach are then discussed.

Although frequency selective surface (FSS) and extraordinary transmission (ET) devices also employ resonant transmission through aperture arrays, these technologies require aperture sizes and/or spacing to be electrically large as discussed before, and therefore, would not be suitable for sampling subdiffraction details in a frequency-multiplexed imaging scheme. To sample subdiffraction spatial information, an aperture array would require deeply subwavelength apertures that can be closely spaced. Therefore, the proposed metascreen design is perfectly suitable for a frequency-multiplexed imaging scheme. Examples of the use of MTM slabs or MTSs to perform high-spatial-resolution imaging may also be found in [183, 184].

Here, a one-dimensional (1D) array consisting of five subwavelength MTM-lined apertures with diameters measuring smaller than one-sixth of a free-space wavelength at an operating frequency of 3 GHz are used to image subwavelength conducting obstacles. In order for these apertures to have different resonance frequencies, the aperture radii

are kept constant and the liner properties are changed by varying the degree of inductive loading (see [185, 186] for an alternative method). In this application, subwavelength apertures and their varying inductive loading are realized in a fully printed fashion. These apertures are then applied to the mouth of a custom-designed TEM horn antenna in order to build a near-field probe capable of magnifying subdiffraction spatial information to the far-field.

5.1   Aperture Design

As discussed in previous chapters, the ENNZ MTM-lined aperture may be implemented using a printed-circuit process based on inductively loaded copper traces as was depicted in Fig. 3.1(c). The lumped inductors used to load the liner can be implemented using either discrete, surface mount inductors or fully printed (e.g. meandered) inductive traces. Here, the design procedure for the proposed imaging principle will be explained on the basis of discrete inductor loading, but will ultimately be realized using printed inductors for reasons that will be discussed later. Therefore, the inductors are given a representative inductance and quality factor of 24 nH and 400, respectively, for an anticipated resonance in the vicinity of 3 GHz. Other important parameters are labeled in Fig. 3.1(c), and their design values are as follows: inner radius ($a = 4.31$ mm), outer radius ($b = 7$ mm), hole periodicity ($P = 20$ mm), trace width ($W = 0.35$ mm), and gap size ($g = 100$ μm). An
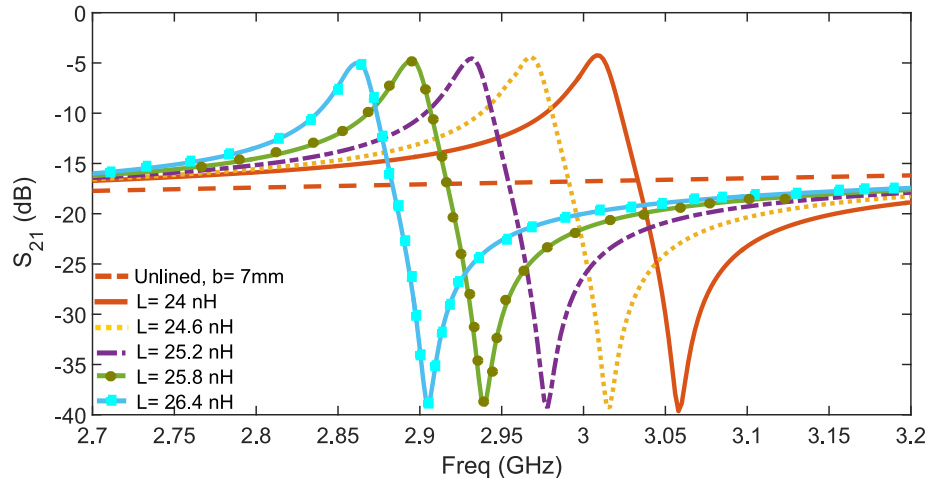
FIGURE 5.1: S_{21} for an infinite array of MTM-lined circular apertures as inductive loading increases in increments of 0.6 nH. The dashed curve shows S_{21} for an identical screen of unlined apertures.

infinite array of these apertures is then simulated using Ansoft HFSS, and the transmission parameter (S_{21}) is obtained, as shown in the solid orange curve in Fig. 5.1. The dashed orange curve in the same figure represents the transmission level in the absence of the ENNZ MTM liners, as a reference. A Fano-like resonance-antiresonance profile is observed for the MTM-lined apertures (the solid orange curve) at 3.01 GHz corresponding to the reduced HE_{11} resonance frequency of this aperture, while there is no resonant behaviour in the dashed curve.

The proposed imaging scheme requires subwavelength resonators possessing distinct resonance frequencies. To modify the resonance frequency of the MTM-lined aperture, either radius or inductive loading can be changed [187]. The design procedure presented

here utilizes varying inductive loading with fixed radius so as to achieve fixed spatial resolution. The remaining curves in Fig. 5.1 show the change in the reduced HE_{11} resonance frequency as the inductive loading is increased in increments of 0.6 nH, causing a change only in the MTM-liner properties. Therefore, $L_1 = 26.4$ nH, $L_2 = 25.8$ nH, $L_3 = 25.2$ nH, $L_4 = 24.6$ nH, and $L_5 = 24$ nH. It is worth noting that these apertures measure approximately $\lambda/7.5$ at the center resonance frequency, as size was kept fixed at $b = 7$ mm. Indices 1 to 5 are chosen such that 1 always indicates the lowest-frequency aperture. It should be noted that higher degrees of miniaturization such as $\lambda/8$ and smaller can be achieved by means of stronger inductive loading [185, 186].

5.2   The Design of Discrete-Inductor Aperture-Array

The apertures described above are now cascaded with a spacing of 20 mm ($\lambda/5$) as shown in Fig. 5.2(a), and the resulting 1D array is periodically repeated in both transverse directions. The particular increment in inductance was chosen in order to place the resonance of each aperture within the antiresonance of the adjacent aperture in order to obtain strongly decoupled resonances when the apertures are cascaded. The aperture screen is illuminated by a normally incident plane wave, and the resulting transmission data is presented in Fig. 5.2(b). There are five distinct peaks observed in the transmission spectrum with a resonance-antiresonance contrast of $5 - 15$ dB, each corresponding to a particular aperture in the array, and labeled accordingly. As previously noted, one can design for the

(a)

(b)
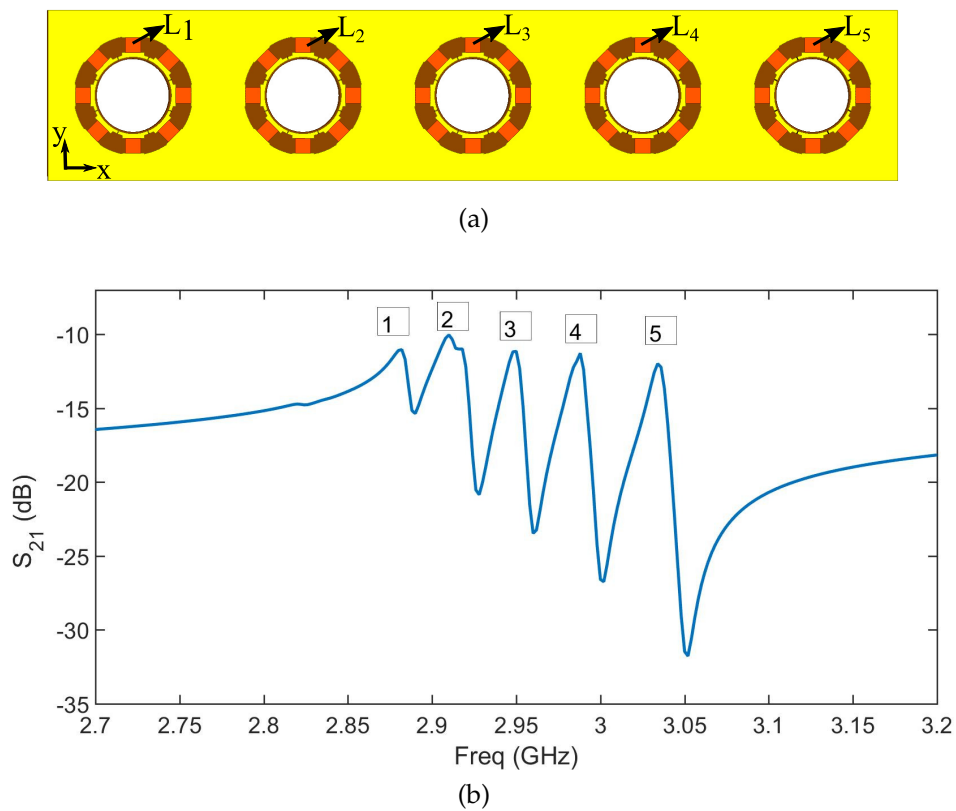
FIGURE 5.2: (a) Arrangement of five adjacent apertures whose inductive loading elements are varied in increments of 0.6 nH; (b) simulated S_{21} for an infinite 2D array of apertures obtained by periodically repeating the five apertures shown in part (a) in both transverse directions.

same behaviour by changing the radius and keeping the inductive loading fixed, as was done in [185, 186].

5.3   The Design of Fully Printed Aperture-Array

The above design procedure focused on apertures loaded with discrete inductors in order to illustrate the principle and simplify the design process. However, one challenge associated with designing with discrete loading inductors is the possibility of inductance value shifts as a result of soldering and the presence of inductor pads [187]. Mutual coupling between the inductors, both within a single aperture and also between adjacent apertures, particularly for high-quality wirewound surface-mount inductors, has also been observed to shift or diminish the resonances [186]. To overcome the practical challenges associated with the discrete-inductor design, a fully printed implementation for the ENNZ MTM liner is now considered, and is shown in Fig. 5.3(a). This implementation employs fully printed dual-arm spiral inductors realized using meandered conductive traces on Rogers 5880 dielectric substrate, and has several advantages over employing discrete inductors, including simplified fabrication using established PCB techniques, lower cost, broader-band resonances (as a result of larger parasitic effects), as well as higher predictability, as any mutual coupling between elements is fully accounted for in full-wave simulations. However, the degree of miniaturization is reduced from $\lambda/7.5$ to $\lambda/6.4$ as a result of

(a)

(b)
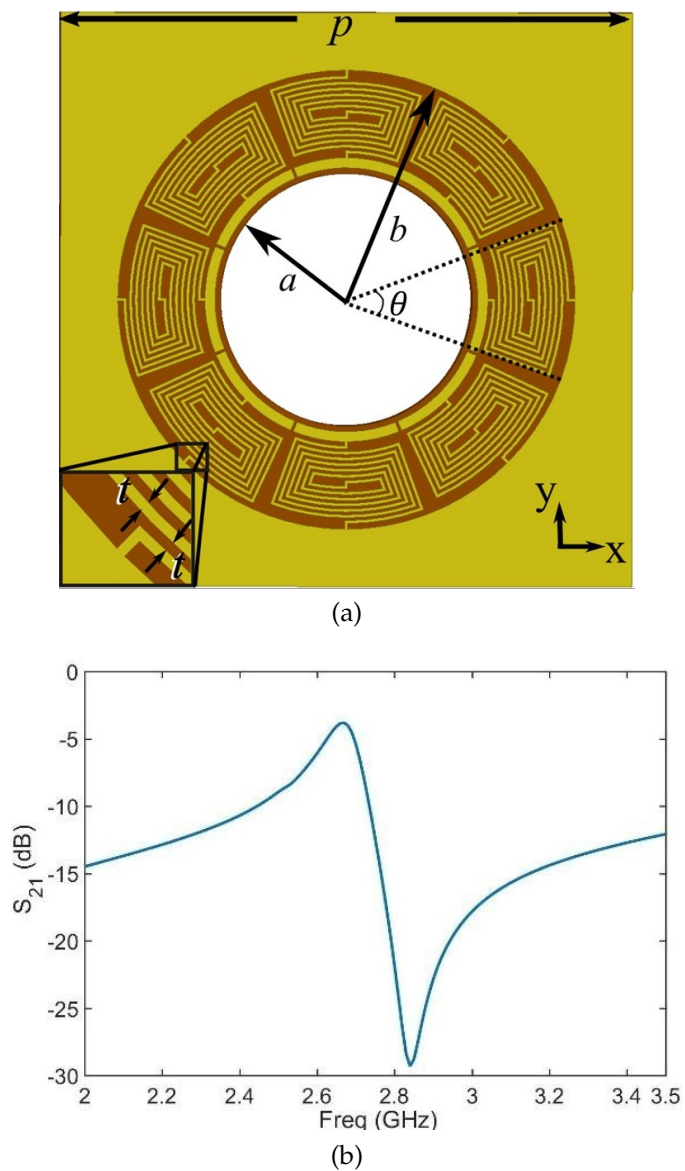
FIGURE 5.3: (a) Fully printed MTM-lined aperture; (b) far-field transmission
spectrum for an infinite array of the unit cells shown in part (a).

(a)

(b)
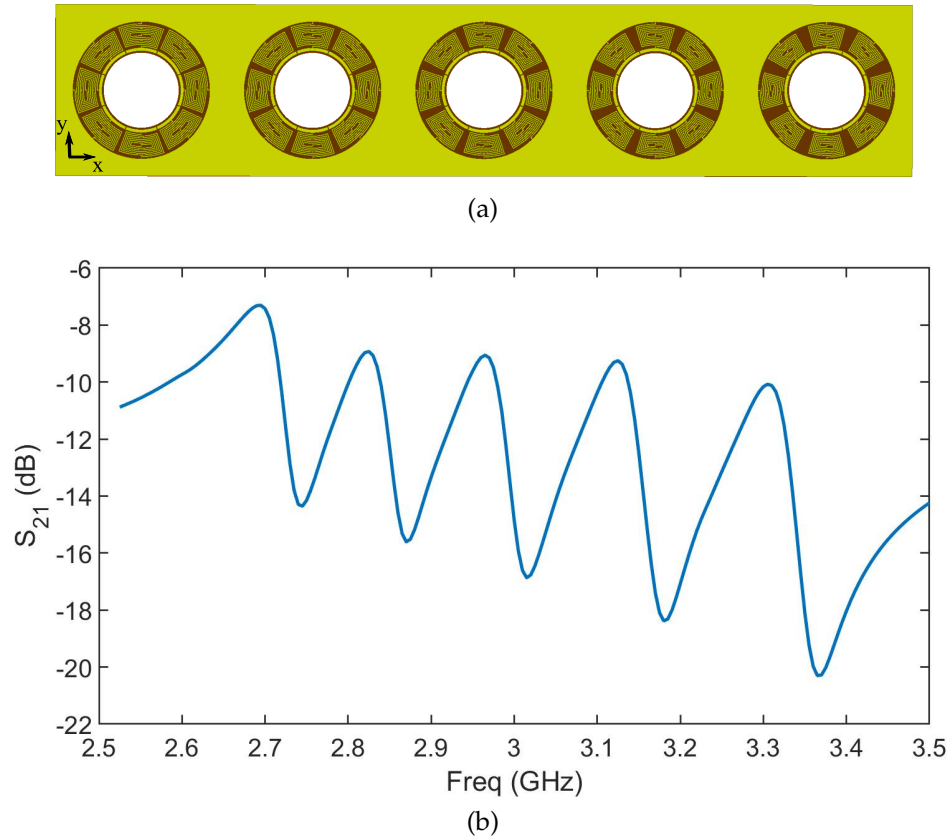
FIGURE 5.4: (a) Five cascaded fully printed MTM-lined apertures with different printed loading inductors; (b) simulated S21 for an infinite 2D array of apertures obtained by periodically repeating the 1D array shown in part (a) in both transverse directions.

lower effective inductive loading compared to the discrete loading elements. As previously noted, more extreme miniaturization levels, such as $\lambda/8$ or smaller, can be achieved using stronger inductive loading (e.g. with finer printed features, increasing the angular span [θ] of the dual-arm spiral inductors, and/or by increasing the thickness of the liner region). The fully printed implementation of this MTM-lined aperture shown in Fig. 5.3(a) employs 100 μm-wide traces and gaps to realize the dual-arm spiral inductors. The transmission spectrum for an infinite array of a single such aperture is shown

in Fig. 5.3(b), which possesses the characteristic Fano lineshape as previously observed in Figs. 5.1-5.2, but with a lower insertion loss, higher contrast, and a much broader-band resonance/antiresonance profile. As such, this unit cell can be employed in an identical way as presented in previous studies for the proposed imaging scheme. In addition to the advantages listed above, the resonance frequency of this new aperture design is much easier to control by changing the parameters of the spiral inductors, such as their angular span (θ), while keeping the outer radius, b, fixed. In fact, Fig. 5.4(a) shows an example of such a design where each printed inductor's angular span, θ, is changed in uniform increments of $2°$, resulting in five apertures sharing the same size ($b = 8$ mm), but different inductor spans of $40°$, $38°$, $36°$, $34°$, and $32°$. Figure 5.4(b) shows the corresponding transmission spectrum for an infinite array obtained by periodically repeating this 1D array in both transverse directions. As confirmed in Fig. 5.4(b), the fully printed MTM-lined apertures exhibit the cascaded resonances previously seen, and this fully printed structure is hereafter used to verify the proposed imaging scheme in the continuation of this work.

To verify that each of the peaks observed in the transmission spectrum corresponds to the resonance of a single aperture, the complex electric-field (phasor) magnitudes are plotted at each resonance (peak) frequency, as shown in Fig. 5.5, starting from the lowest resonance frequency (part (a)) to highest resonance frequency (part (e)). As these data demonstrate, the fields are strongly localized at each aperture at its respective resonance

(a)

(b)

(c)

(d)

(e)
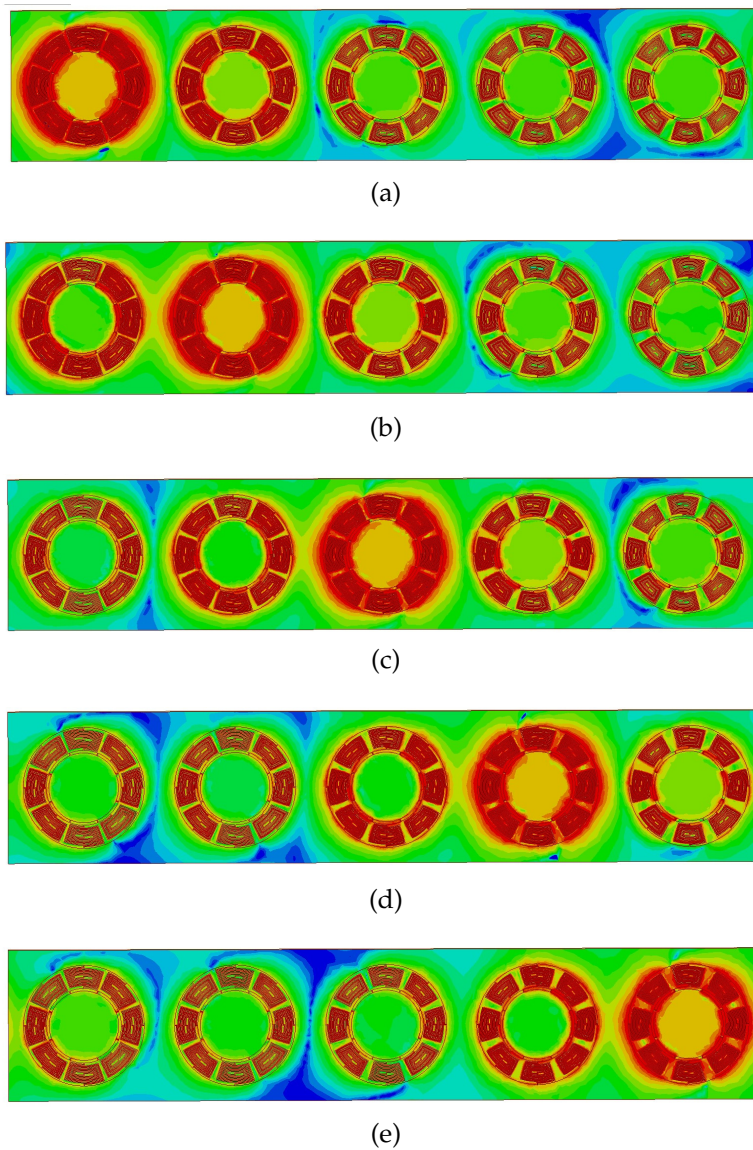
FIGURE 5.5: Complex electric-field magnitudes at successive resonance frequencies: (a) 2.695 GHz, (b) 2.82 GHz, (c) 2.965 GHz, (d) 3.12 GHz, and (e) 3.30 GHz.

frequency, establishing a one-to-one correspondence between aperture location and aperture resonance frequency.

5.4   Imaging of Conducting Obstacles

Figure 5.6 shows the transmission spectrum when each of the individual apertures are successively blocked by conducting discs. The curve shown in Fig. 5.4(b) is repeated here as the solid blue curve for reference. The data in Fig. 5.6 confirm that obstruction of each resonant aperture by a conducting disc causes the corresponding resonance-antiresonance to disappear from the transmission spectrum, while leaving the transmission behaviour at other frequencies relatively unaffected. Consequently, the presented approach enables far-field identification of conducting obstacles as small as $\lambda/6.4$ with a spacing as small as $\lambda/5$, determined only by the size of the resonators and period of the array, respectively, in the frequency range of 2.5 GHz-3.5 GHz.

One straightforward method for evaluating the data in Fig. 5.6, other than following the trend of each curve, is evaluating the difference (in log) between each curve and the reference curve obtained in the absence of obstacles (or the ratio if expressed in linear terms). The difference can be plotted so as to emphasize either the resonance or the antiresonance of the aperture. Our studies show that there is a higher such difference caused by the disappearance of antiresonances. Therefore, the curves in Fig. 5.7 plot the difference between the transmission data in the following two cases: i) a conducting obstacle
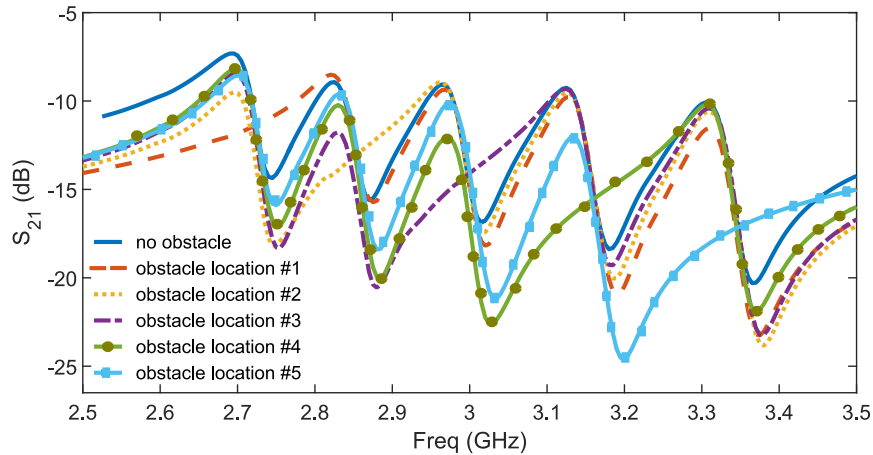
FIGURE 5.6: Transmission spectra showing the effect of blocking one aperture
at a time using a conducting obstacle.

blocking one aperture at a time and, ii) no obstacle in the vicinity of the aperture array,
which results in maxima in difference curves at the location of the (now absent) antireso-
nances. It can be seen how the maximum location changes from one frequency to another
among these difference curves as the obstacle's location is varied, resulting in unique iden-
tification of an obstacle's location. It must be noted that the simulations presented in Fig.
5.6 and Fig. 5.7 create the infinite array using periodic boundary conditions, but this also
periodically replicates the conducting discs, resulting in an unrealistic imaging scenario.
Thus, study of a finite array of these apertures becomes necessary for practical verification
of this imaging scheme. Therefore, the remainder of this paper focuses on a finite 1D array
of the proposed five fully printed apertures. To obtain proper excitation of this 1D array of
apertures using a suitably polarized plane-wave-like excitation, a custom-designed TEM
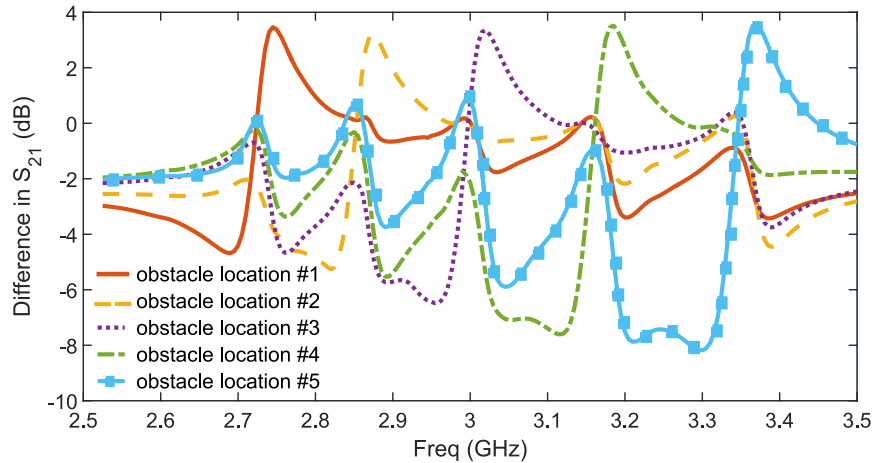
FIGURE 5.7: Difference between each of the curves presented in Fig. 5.6 and the reference data (no obstacles), resulting in maxima in the locations of antiresonances of the different apertures.

horn antenna is used to obtain the boresight far-field transmission spectrum using measurements in an anechoic chamber. The following subsection presents the design of the TEM horn antenna in the desired frequency range.

5.5 TEM Horn Antenna+1D Aperture Array

The design of the customized TEM horn antenna that will be used to excite the 1D aperture array is presented in Appendix A. This custom-designed TEM horn antenna possesses multiple matching regions at frequencies corresponding to its length being an integer multiple of half wavelengths. The desired matching region is demonstrated through the general agreement of the simulated and measured S_{11} data shown in Fig. 5.8, which is designed so as to accommodate the resonance frequency range of the fully printed design
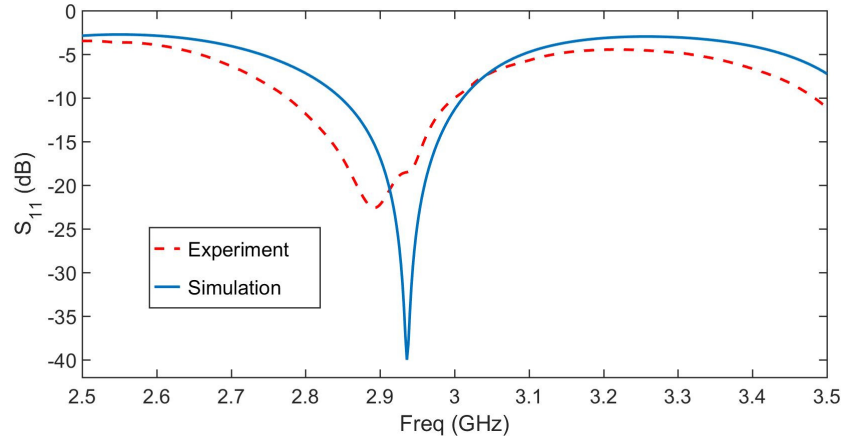
FIGURE 5.8: Simulated S_{11} (solid blue curve) and measured S11 (dashed red curve) for the TEM horn antenna.

(i.e., 2.7 GHz-3.3 GHz). As the resonances of the fully printed design are fairly broadband, the 10-dB return-loss bandwidth of the horn does not fully accommodate them. However, as will be shown in the simulation and experimental data, the resonances are still excited strongly enough to enable demonstration of the proposed imaging scheme.

The designed 1D array of apertures is integrated with the TEM horn antenna as shown in Fig. 5.9(a) in order to construct a practical near-field probe that can scan a 1D subdiffraction distribution of subwavelength obstacles and magnify their locations to the far-field transmission spectrum. The simulated far-field behaviour of this device is shown in the solid blue curve in Fig. 5.9(b), along with the response of the infinite array illuminated by a plane wave previously shown in Fig. 5.4(b) (dotted orange curve), appropriately normalized for comparison. This comparison shows that although the size of the imaging device is reduced from an infinite array to a finite array of five apertures measuring $\lambda/5$ by , where λ is the free-space wavelength at 3 GHz, the high contrast observed from
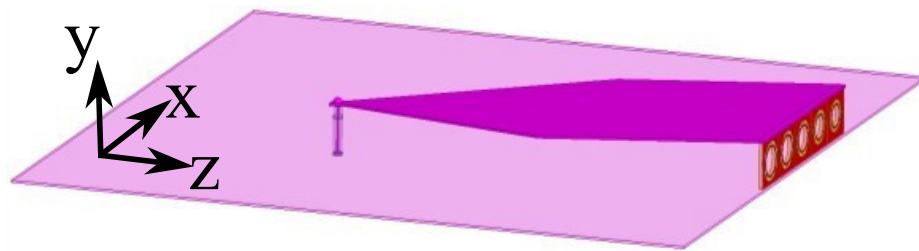
(a)
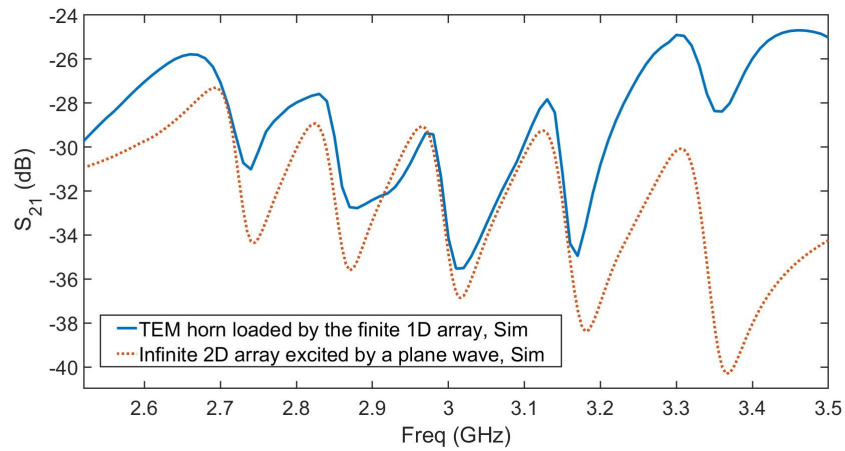
(b)

FIGURE 5.9: (a) TEM horn antenna with integrated nonuniform aperture array, and (b) simulated far-field behaviour of the proposed device; S_{21} of the infinite array previously shown in Fig. 5(b) is repeated in dotted orange for comparison (levels appropriately normalized to enable comparison).

plane-wave illumination of an infinite array of apertures is almost fully realized by using the TEM horn to excite a finite aperture array. This is caused by the PEC parallel-plate-waveguide-like environment of the TEM horn antenna, which establishes boundary conditions in the vertical direction that mimic the response of a vertically infinite array by means of image theory. These data also confirm that illumination using the TEM horn antenna does not cause a frequency shift, but affects the trend/level of transmission across the operating band, consistent with the varying return loss of the horn (that is, the trend of the curves matches best near the matching region of the TEM horn). This is also caused by the production of multiple resonances within the TEM horn antenna due to strong reflection from the apertures away from their resonance frequencies, which affects the radiated pattern of the TEM horn antenna.

5.6   Fabrication and Measurement

The fully printed MTM-lined aperture array presented in Fig. 5.4(a) is fabricated using an LPKF ProtoMat S62 mechanical milling machine, which employs milling bits at high RPM to remove copper cladding from a microwave substrate. The use of 100 µm features was motivated by the diameter of the finest available milling bit, and an error of up to 6% was allowed so as to obtain a continuous milling path. The milling was done on a Rogers 5880 substrate with a rotation speed of 62000 rpm and a travel speed of 0.5 mm/s, and the milling depth was adjusted for each of the 40 inductors individually so as to avoid

(a)

(b)
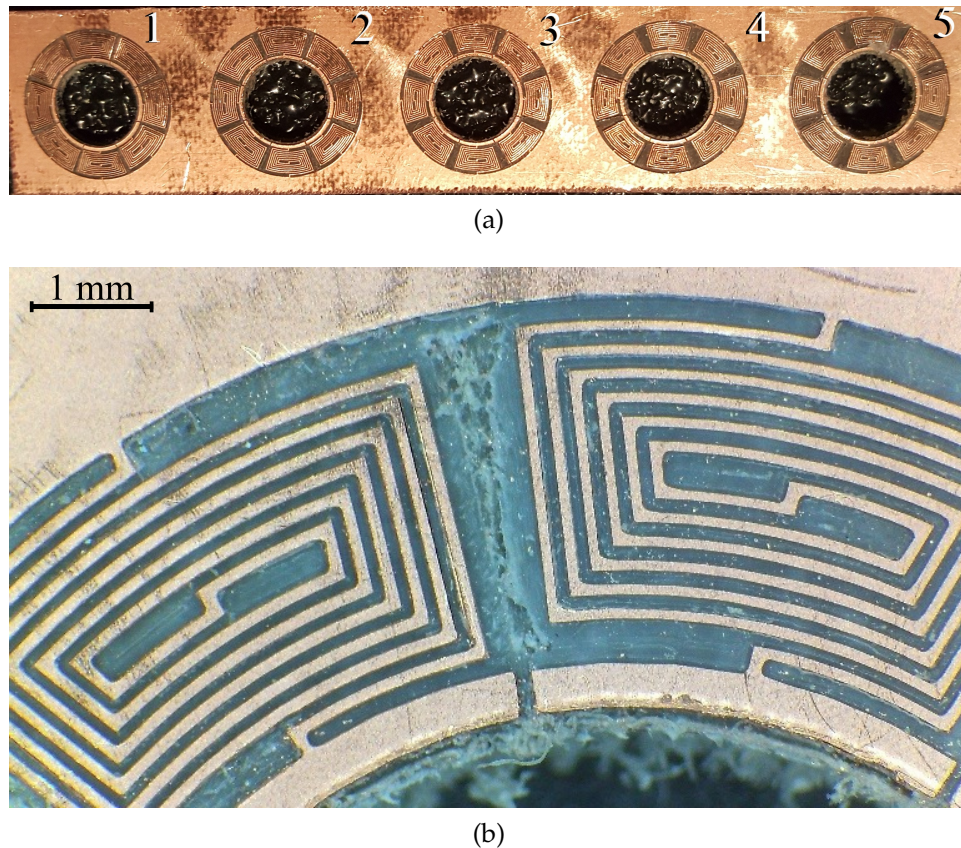
FIGURE 5.10: (a) Fabricated fully printed aperture array, and (b) magnified view of two adjacent dual-arm spiral inductors in a single unit cell.

overmilling that could result in bending of the fine traces.

The anticipated fabrication error of up to 6% implies the possibility of slight frequency shifts and/or a frequency dilation in the resonance frequency spectrum of these resonators. Fig. 5.10(a) shows the fabricated fully printed aperture array, and Fig. 5.10(b) a magnified view of two adjacent dual-arm spiral inductors, which also demonstrates slightly different trace widths as a result of the nonuniform milling error. Using other technologies such as laser milling for future fabrication of such fine features should mitigate these errors.

Figure 5.11(a) shows the fabricated single-sided TEM horn antenna with ground plane,
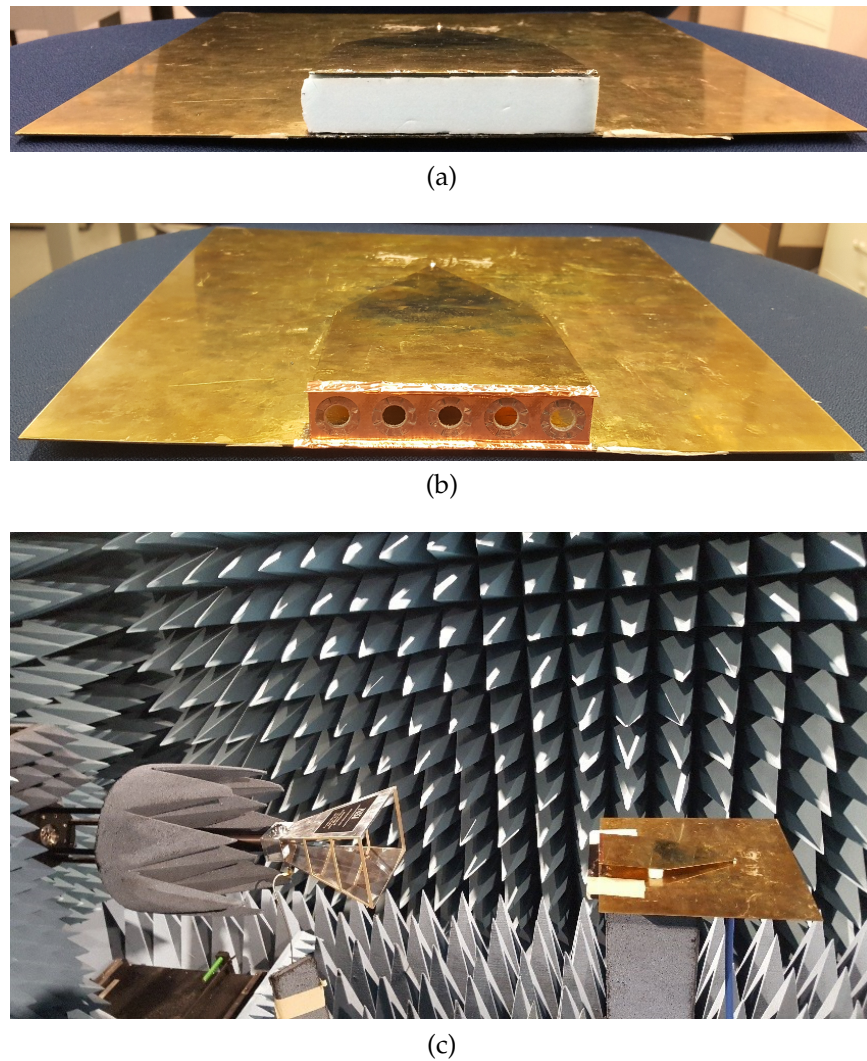
FIGURE 5.11: (a) Fabricated TEM horn antenna with foam spacer; (b) fabricated TEM horn probe with integrated nonuniform aperture array; and (c) experimental setup including the double-ridged horn probe (left) and the TEM horn probe under test (right).

and the dashed red curve in Fig. 5.8 represents the measured S_{11} of this antenna along with the simulated S_{11} (solid blue curve) so that a comparison is possible. The agreement in these data and radiation-pattern measurements (not shown here) establish that the TEM horn works as expected. The 1D MTM-lined aperture array is applied to the mouth of TEM horn antenna as shown in Fig. 5.11(b), and the boresight far-field amplitude is measured in an anechoic chamber according to the measurement setup shown in Fig. 5.11(c), which pictures the double-ridged horn probe antenna on the left-hand side and the TEM horn antenna under test on the right-hand side, placed at a distance of 397 mm apart (4λ at the center frequency).

The obtained far-field data is presented in Fig. 5.12(a). The simulated response of this device was previously shown in Fig. 5.9(b), which may be considered the ideal response expected from the aperture-array-loaded TEM horn, neglecting other non-idealities such as fabrication error/tolerances. Although there seem to be some additional ripples in the measured data, possibly because of the imperfect measurement environment (e.g., reflections from the positioners and associated apparatus supporting the TEM horn antenna), the five main peaks can still be distinguished in the measured data, with varying contrasts of between 2 and 6 dB. The nonuniform contrast of these Fano-shape resonances is to be expected due to the nonuniform excitation of the resonances based on the varying S_{11} and boresight directivity of the TEM horn antenna across the frequency band. This lower contrast can also be observed in the simulated data at high frequencies. Although

the measured response exhibits the same general trend as the simulated response, there is the expected slight frequency shift/dilation of resonances in the measured spectrum caused by the imperfect fabrication of the fully printed $100\,\mu$m spiral inductors, as discussed above.

The possibility of using this device for imaging of conducting obstacles is examined in measurements by placing a PEC obstacle in the vicinity of each aperture. The resulting measured raw amplitudes are plotted in Fig. 5.12(b). As is evident from following the trend of each far-field transmission curve, covering one aperture using a conducting obstacle removes the corresponding resonance-antiresonance from the far-field transmission spectrum. Once again, it is beneficial to plot the difference between the following two cases: i) a conducting disc present in front of one aperture at a time, and ii) no conducting disc in the vicinity of this device. This difference is expected to emphasize the disappearance of antiresonances similar to the simulation data presented in Fig. 8 for an infinite array. As noticeable in the difference curves plotted in Fig. 5.12(c), the antiresonance (i.e., peak in the difference curve) location shifts from higher to lower frequencies as the location of a conducting disc is varied from aperture 1 to aperture 5. It should be noted that suppression of isolated resonances requires that the conducting obstacle be placed very near to the aperture array; increasing this distance creates the possibility of exciting adjacent apertures, albeit more weakly. Although such effects could be mitigated by increasing the spacing between resonators, this would result in lower spatial resolution

as well as a larger overall size of the array. Therefore, detection of conducting obstacles experiences a trade-off between detectable spacing of the obstacle from a resonator and resolution/overall size of the imaging device with respect to wavelength.

To verify that this method works in the presence of multiple obstacles, the application of two conducting obstacles to the vicinity of two randomly chosen apertures is experimentally studied. Apertures 3 and 5 are blocked using conducting obstacles, and the resulting measured far-field amplitude is plotted in Fig. 5.13(a). The reference far-field amplitude data previously presented in Fig. 5.12(a) is repeated here for comparison. As is evident from these data, resonances corresponding to apertures 3 and 5 disappear from the far-field spectrum. Once again, the difference between these two cases is plotted in the same manner as before, and shown in Fig. 5.13(b). It can be easily seen that maxima appear at the corresponding locations of the (now absent) antiresonances in the difference curves. The reader may note that the local maximum at 2.92 GHz is much smaller than the other two maxima and more importantly, below 0 dB, and therefore, cannot correspond to the disappearance of an antiresonance.

An independent set of experimental data is presented here to verify that the resonance location moves across the operating frequency range from one resonator to another, and to confirm that the right frequencies are chosen when identifying the resonances in Fig. 5.12(a). This new experiment is performed using two electrically small loop antennas. The loops are placed at a center-to-center distance of 9 mm, and the aperture array is inserted
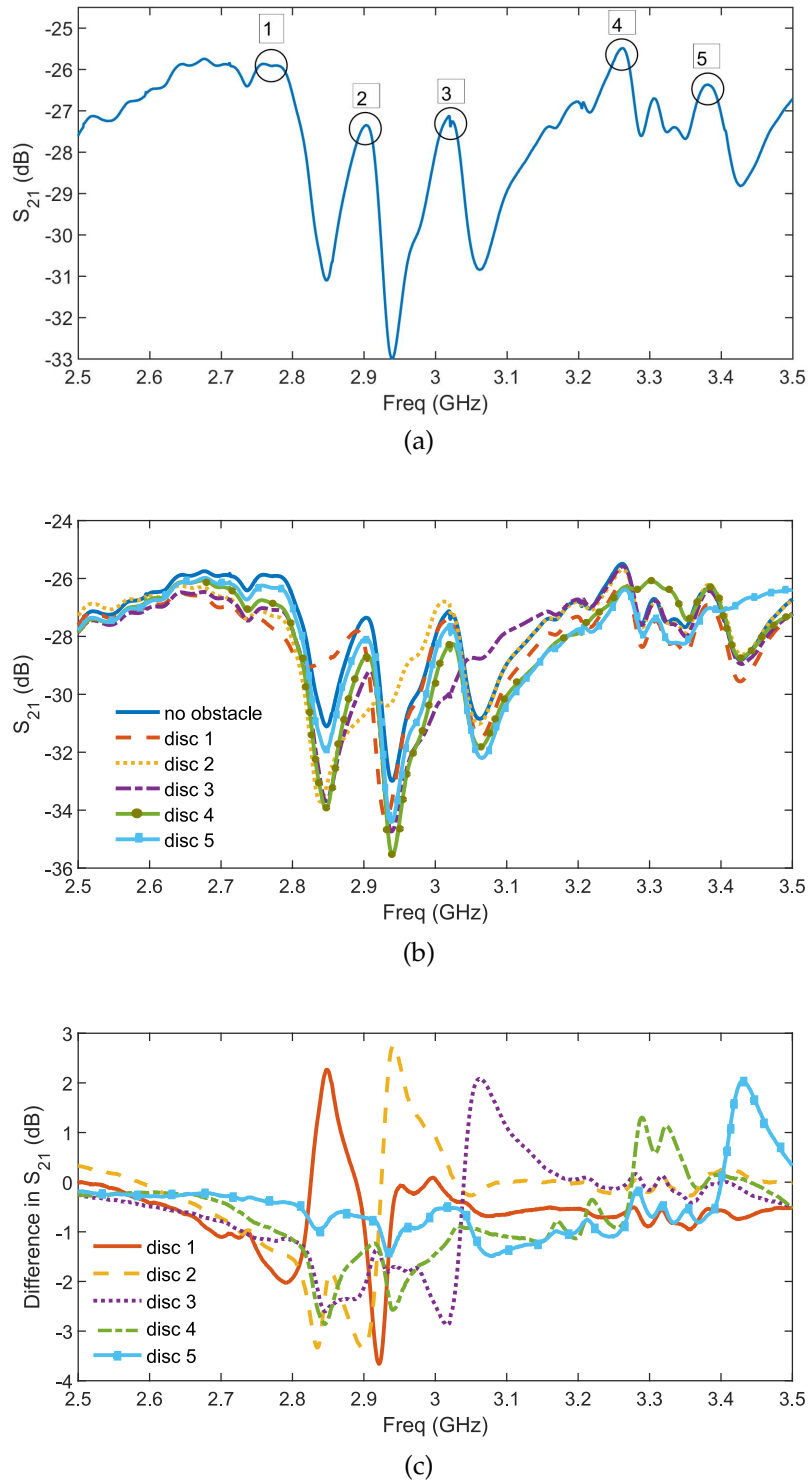
FIGURE 5.12: (a) Measured far-field behaviour of the proposed device; (b) effect of applying conducting discs to each aperture; (c) difference in the measured far-field amplitudes in each case.
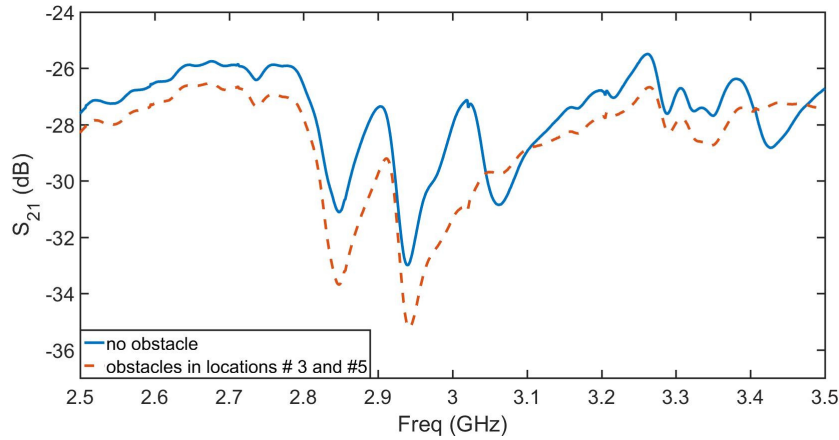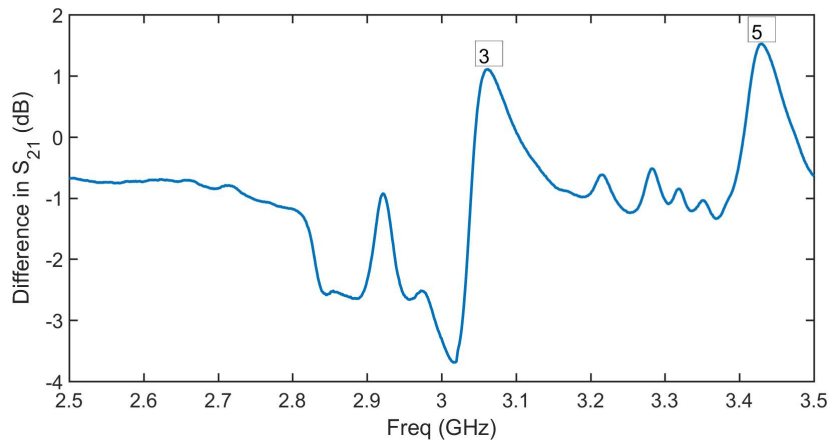
FIGURE 5.13: (a) Measured far-field behaviour in the presence of conducting discs at locations of aperture 3 and aperture 5, along with the reference far-field transmission when no discs are present; (b) difference between the two curves shown in part (a).
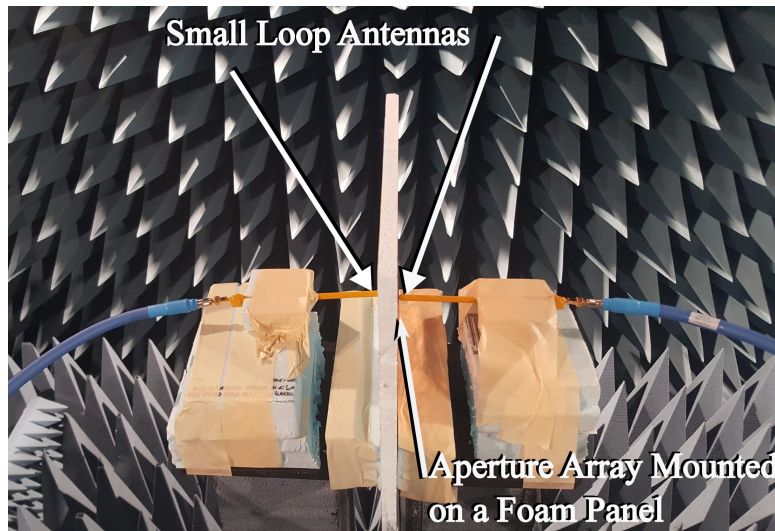
(a)
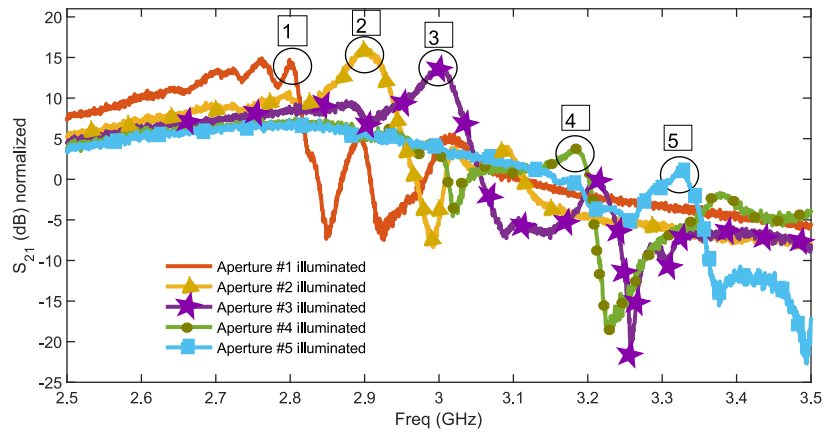
(b)

FIGURE 5.14: (a) Experimental setup including the aperture array mounted on foam and two small loop antennas; (b) measured transmission between two loop antennas as they are moved from aperture to aperture.

symmetrically between the two loop antennas as shown in Fig. 5.14(a). An amplifier is used to improve the signal levels, as these small loops are very poor radiators. This experimental setup is used to obtain the transmission between the two loop antennas as they are moved across the screen from one then resonator to another. The acquired transmission data are normalized to the transmission between two loop antennas in the absence of the screen, over the same loop-to-loop distance. As is evident from the resulting normalized transmission data presented in Fig. 5.14(b), the transmission peak location moves from higher to lower frequencies as the loop antennas are scanned from one resonator to another, with transmission peaks occurring at exactly the same locations as the peaks identified in Fig. 5.12(a). This independent experimental result affirms that the peaks marked in Fig. 5.12(a) are the actual transmission resonances for which this device was designed, and not additional diffraction effects caused by the TEM horn and/or experiment environment.

Chapter 6

Metafilm Design Used for Shielding

In this chapter, a novel, extremely miniaturized metafilm unit cell is introduced. This design is motivated by the complementary *metascreen* technology previously presented in chapter 4, where the miniaturization of a circular aperture in a metallic screen was achieved by means of lining the aperture using a thin layer of ϵ-negative and near-zero (ENNZ) metamaterial (MTM) liner. Here, we show that if the metallic and gap regions in Fig. 6.1(a) are interchanged, and the shunt (radially directed) loading inductors are replaced with series (azimuthally directed) loading capacitors as was shown in Fig. 3.3, a metafilm is obtained that demonstrates dual transmission/reflection behaviour. Based on the notion of duality, the metafilm structure consists of a metallic disc lined using a μ-negative and near-zero (MNNZ) MTM liner, and supports modes with interchanged transverse electric- and magnetic-field distributions as compared to the metascreen design. Such discs undergo resonance at sizes of $\lambda/7$ or smaller and exhibit interesting transmission/reflection behaviour. When an array of these resonators is illuminated using a

normally or obliquely incident plane wave, a Fano-shape reflection profile is obtained, exhibiting a high degree of reflection at resonance followed by strong transmission. Just like the metascreen design, these resonators may be closely packed since the resonance mechanism does not rely on diffraction effects, resulting in a compact metafilm design. This technology, like its metascreen counterpart, lends itself to a variety of applications ranging from shielding to imaging to antenna beamforming. Given the large number of applications that may benefit from the proposed metafilm technology, this chapter presents the detailed study of its unit-cell design and resonance mechanism.

6.1 Transmission Studies

The metascreen unit cell and its complementary metafilm design previously studied in chapter 3 are repeated here in Fig. 6.1. Similar to the metascreen design, there are multiple benefits in using fully printed loading elements in the implementation of the metafilm unit cell including lower cost, easier single-step fabrication (as soldering of surface mount components would not be required), precise control of the resonance frequency by simply varying the capacitor's span and/or number of interdigitations, larger resonance contrast, as well as broader-band response due to added parasitic effects. Therefore, the discrete, azimuthally directed loading capacitors shown in Fig. 6.1(b) are replaced by their fully printed interdigitated counterparts as shown in Fig. 6.2(a). Important design parameters are labeled in this figure, and their values are chosen as follows: $b = 8.5$ mm, $a = 5.15$ mm,
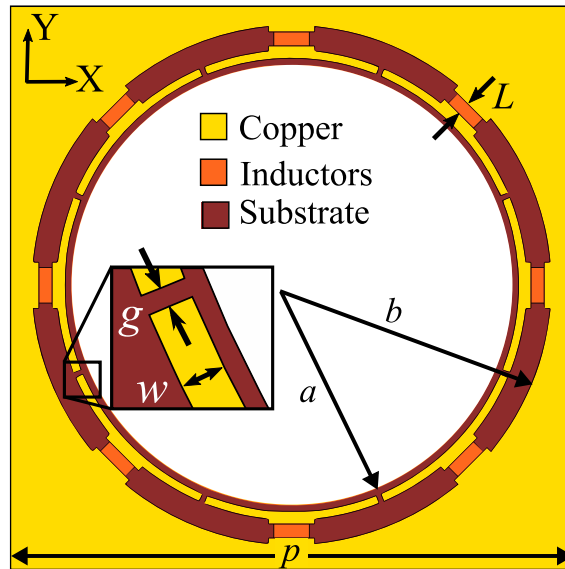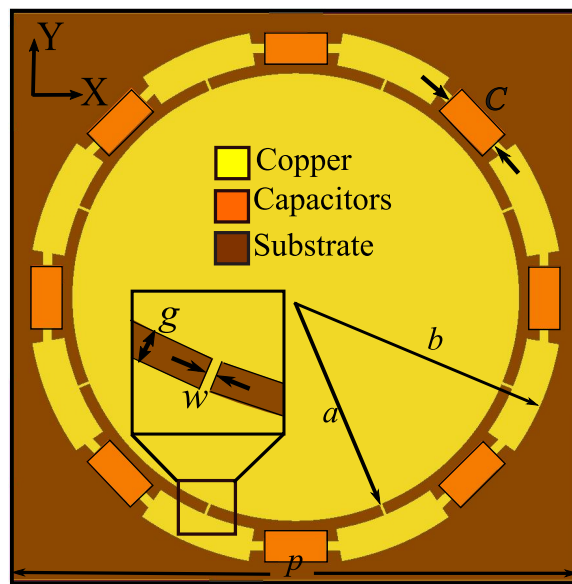
FIGURE 6.1: (a) The unit cell of ENNZ MTM lined metascreen unit cell, and (b) the complementary metafilm topology.

$\theta = 40°$, $w = 0.1$ mm, and $t = 0.1$ mm, so that the fully printed metafilm unit cell resonates at 2.45 GHz.

Figure 6.3 shows transmission and reflection parameters obtained through full-wave HFSS simulations for an infinite array of the following two unit cells, each illuminated using a normally incident plane wave: i) the fully printed MNNZ-loaded disc shown in Fig. 6.2(a), and ii) an unloaded metallic disc unit cell with an outer radius of $b = 8.5$ mm, plotted for reference. The screen used in each array is a Rogers/Duroid 5880 substrate ($\epsilon_r = 2.2$, $\tan \delta = 0.0009$) of 1.524-mm thickness, metallized on one side with copper of thickness 17 μm. As is evident from the data in Fig. 6.3, no resonance effect is observed for the unloaded metallic-disc array (dot markers), since these frequencies are far below the first grating anomalies or structural resonances of the metallic disc. Dramatic changes in the response are observed as the MNNZ liner loading is introduced. A resonance effect is observed at 2.44 GHz in the curves corresponding to the fully printed metafilm, where the discs are extremely subwavelength and measure approximately $\lambda/7.4$ in diameter. The S_{11} parameter (dashed blue curve) experiences a resonant enhancement at 2.44 GHz, providing 4.7-dB (almost three times) better reflection compared to the unloaded-disc array. This reflection peak is followed by a minimum in reflection (i.e., a maximum in transmission) at 2.52 GHz, where a transmission improvement of 1.2 dB (32% better) compared to the unloaded design is achieved, resulting in a transmission level of -0.28 dB. Enhanced transmission levels are maintained towards higher frequencies. The Fano lineshape in the

(a)

(b)
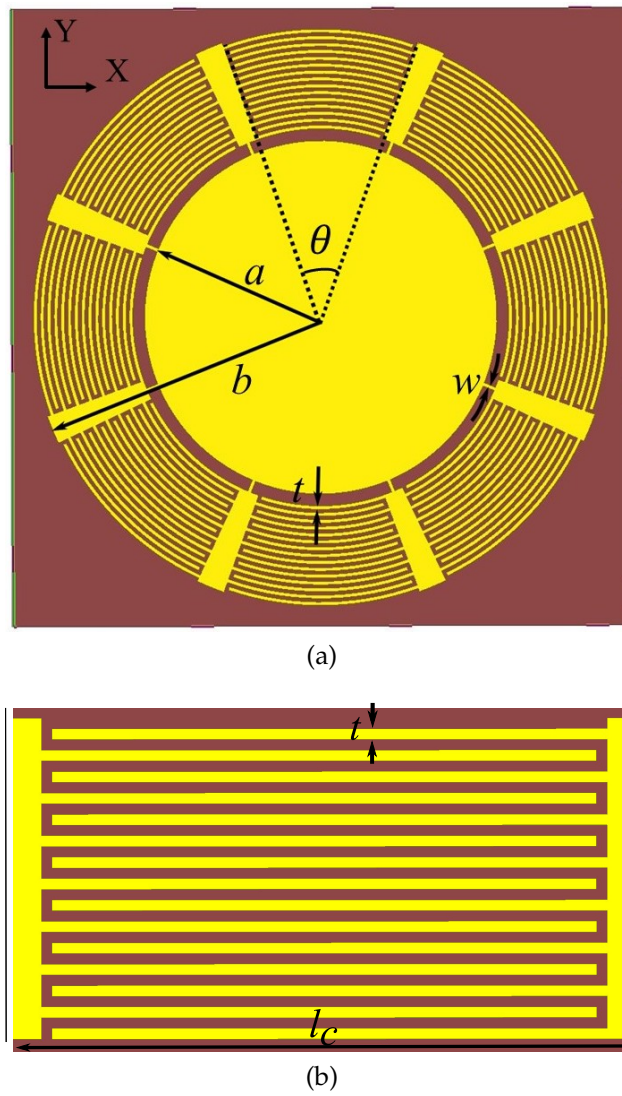
FIGURE 6.2: (a) The metafilm unit cell with a practical liner realized using fully printed interdigitated capacitors and strip inductors, and (b) the straightened out layout of one interdigitated capacitor.
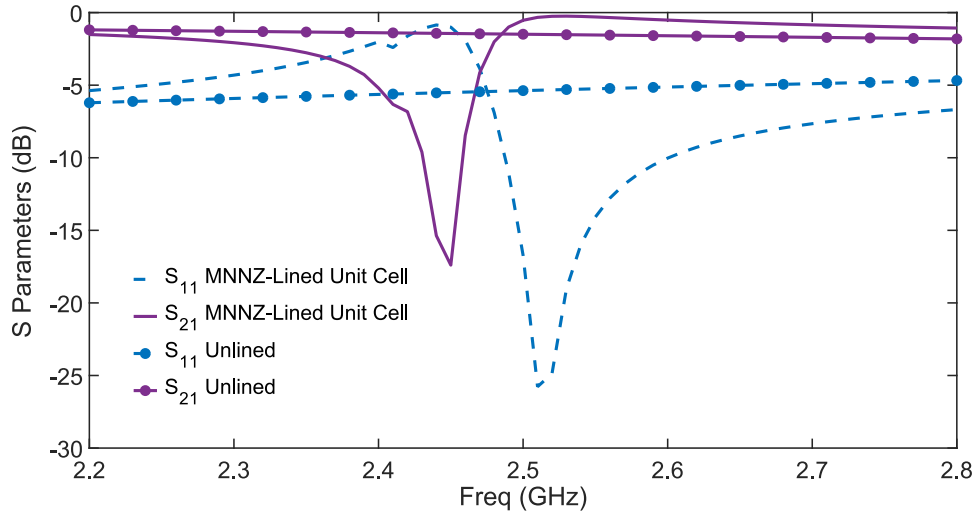
FIGURE 6.3: Scattering parameters of an infinite 2D array of metafilm unit cells shown in Fig. 6.2(a) with design values $b = 8.5$ mm, $a = 5.15$ mm, $w = 0.1$ mm, $t = 0.1$ mm, $\theta = 40°$. Transmission and reflection parameters of an array of unloaded metallic discs with the same outer radius b are plotted in curves with dot makers as reference.

S_{11} of the metafilm design, demonstrating a peak followed by a minimum, is consistent with the observed trend in the S_{21} parameter of the complementary metascreen structure.

6.2 MNNZ Behaviour

To confirm that the occurrence of this resonance is due to the MNNZ properties of the liner, the plasma frequency of the effective permeability of this liner (f_{mp}) can be calculated, which may easily be done using the TL model shown in Fig. 3.4. To simplify the calculation, the straightened-out interdigitated capacitor model shown in Fig. 6.2(b) is used, which possesses the same trace/gap width of $t = 0.1$ mm, the same number of interdigitations as the printed capacitors utilized in the implementation of the MNNZ liner

in Fig. 6.2(a), and an effective length chosen as $l_c = 5.08$ mm, obtained from the weighted average of all interdigitated trace lengths based on the relative strength of surface currents on each trace at the resonance frequency as determined through HFSS simulations. To extract f_{mp} using equations 3.17-3.21, the equivalent $L - C$ impedance of the series TL branch needs to be extracted through full-wave studies. Full-wave HFSS simulations of the capacitor in Fig. 6.2(b) yield $Z(\omega)$. At $\omega = 2\pi \times 2.44$ GHz, $C = 1.27$ pF and $L_t = 1.96$ nH, implying $f_{mp} = 3.19$ GHz. This extraction provides insight into the design of the liner through lumped loading capacitors. To calculate μ_r through 3.22, d (the periodicity of the loaded TL model in the azimuthal direction) and g (the geometrical factor of the TL) need to be calculated. These calculations yield $d = 4.18$ mm, and $g = 0.31$. Therefore, at 2.44 GHz, (3.22) yields $\mu_r = -0.83$, confirming a negative and near-zero value of permeability (i.e., MNNZ behaviour).

6.3 Eigenmode Studies

Eigenmode studies are performed on the fully printed design shown in Fig. 6.2(a) to obtain information about the relevant reduced-frequency resonant modes. Whereas the transverse fields of the metascreen aperture resonances were described in terms of the modal cutoffs of an equivalent ENNZ-lined PEC waveguide, here, we deal with resonances in which the discs support electric fields perpendicular to the inner disc (metallic) region. To facilitate description, we refer to these modes as the hybrid modes of an
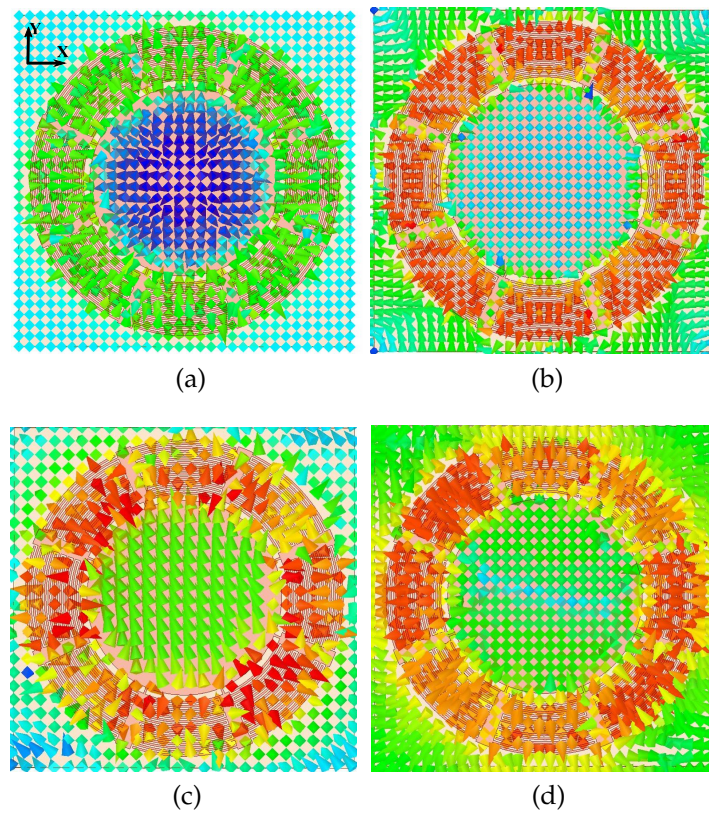
FIGURE 6.4: (a) Vector magnetic fields of the HE_{01} mode, (b) vector electric fields of the HE_{01} mode, (c) vector magnetic fields of the EH_{11} mode, and (d) vector electric fields of the EH_{11} mode of the fully printed design obtained through eigenmode studies. The coordinate system for the unit cell is shown at the top-left corner in part (a) of this figure.

analogous, inhomogeneously filled PMC circular waveguide, which essentially exchanges the roles of the electric and magnetic fields and, therefore, the hybrid-mode descriptors EH and HE, while retaining the mode indices. It is worth noting that the reduced-frequency resonant modes occur in a reverse order compared to the natural modes of a PMC waveguide, as was the case with the ENNZ-lined PEC waveguide [2]. Here, in analogy to the HE_{11} and EH_{01} modes of the ENNZ-lined metascreen apertures, we concentrate on the EH_{11} and HE_{01} modes of the MNNZ-lined metafilm discs, for which the reduced-resonance frequencies obtained through eigenmode study are $f_{01} = 3.26$ GHz and $f_{11} = 2.39$ GHz. Figure 6.4 demonstrates the vector magnetic- (H-) and electric- (E-) fields of the fully printed metafilm unit cell at f_{01} and f_{11}, respectively. A generally radial transverse-field distribution for vector H-fields can be observed in Fig. 6.4(a) at f_{01}, which exhibits the expected zero azimuthal variation. Vector E-fields are perpendicular to the metallic disc region and are all co-directed, as suggested by the distribution shown in Fig. 6.4(b). Figures 6.4(c) and 6.4(d) show the modal H- and E-field distributions at f_{11}. Vector H-fields are strongly collimated in the inner disc region, which is consistent with the collimation of vector E-fields at the reduced HE_{11} mode of the complementary aperture design [187]. Vector E-fields possess the expected purely normal distribution on the inner disc, and the direction of these fields switches in the middle of the metallic region. A closer look at these fields shows mostly radial electric fields in the azimuthal gap between the metallic disc and MTM liner regions, validating the L-C-loaded TL description of the

MNNZ liner region.

It was argued in [176] that the EH_{01} cutoff frequency of an ENNZ-lined circular waveguide coincides with the plasma frequency of the Drude dispersion profile of the liner. In fact, the permittivity of the liner approaches zero at the plasma frequency, which implies an infinite-wavelength condition in the TL mode, and therefore, no azimuthal variation. This condition is satisfied by the resonant field distribution of the EH_{01} mode. Based on the duality observed in the resonance mechanism as well as the modal field distributions between the metafilm and metascreen unit cells, it is proposed that f_{01} in this work corresponds to the magnetic plasma frequency of the MNNZ liner. Assuming a Drude dispersion (i.e., $\mu = \mu_0(1 - f_{mp}^2/f^2)$) for the effective permeability of the liner with $f_{mp} = f_{01} = 3.26$ GHz suggests $\mu_r = -0.78$ at the resonance frequency of 2.44 GHz, very close to the value of -0.83 obtained through TL studies. The values extracted through the two different studies follow Drude-like dispersions that match very well throughout the frequency band, as shown in Fig. 6.5.

6.4   Homogenization and Parameter Extraction

Here, the surface susceptibility parameters are extracted for the proposed metafilm unit cell so as to provide insight into the electric-magnetic-dipole mechanism of resonance and introduce an equivalent homogenized model for this metafilm unit cell. As will be noted in Sec. 6.8, one of the most important applications of the proposed metafilm unit cell is
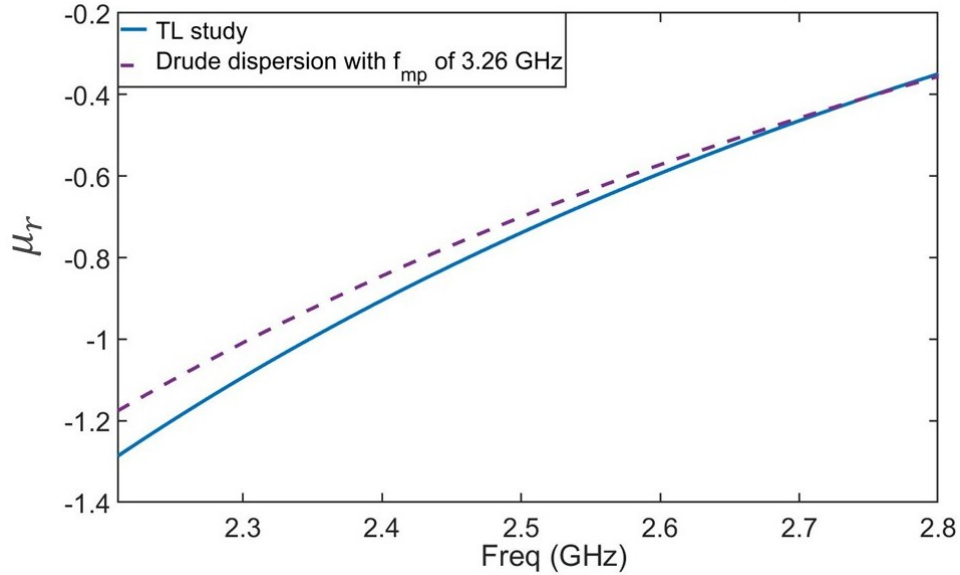
FIGURE 6.5: Dispersion profile of the permeability of the liner obtained through TL and eigenmode studies

beam-shaping through inhomogeneous partially transmitting/reflecting surfaces. However, the accurate study of the proposed unit cell using numerical simulators requires a very fine mesh, which entails time-consuming simulations and prohibitively costly computational resources. This would make the simulation of a finite, inhomogeneous surface difficult even when possible. Consequently, the introduction of an equivalent, homogenized model that can be quickly studied using numerical simulators is essential.

To characterize the proposed metafilm unit cell by obtaining the susceptibility tensors, (6.1a)–(6.1b) may be used [188], which assume that the components of the susceptibility tensors perpendicular to the surface of the metafilm (i.e., in the Z direction) are zero. These equations also assume the general case of a bianisotropic unit cell.

$$
\begin{bmatrix} \Delta H_y \\ -\Delta H_x \end{bmatrix} = j\omega\epsilon \begin{bmatrix} \chi_{ee}^{xx} & \chi_{ee}^{xy} \\ \chi_{ee}^{yx} & \chi_{ee}^{yy} \end{bmatrix} \begin{bmatrix} E_{x_{av}} \\ E_{y_{av}} \end{bmatrix} +
$$
$$
j\omega\sqrt{\mu\epsilon} \begin{bmatrix} \chi_{em}^{xx} & \chi_{em}^{xy} \\ \chi_{em}^{yx} & \chi_{em}^{yy} \end{bmatrix} \begin{bmatrix} H_{x_{av}} \\ H_{y_{av}} \end{bmatrix}
$$
(6.1a)

$$
\begin{bmatrix} -\Delta E_y \\ \Delta E_x \end{bmatrix} = j\omega\mu \begin{bmatrix} \chi_{mm}^{xx} & \chi_{mm}^{xy} \\ \chi_{mm}^{yx} & \chi_{mm}^{yy} \end{bmatrix} \begin{bmatrix} H_{x_{av}} \\ H_{y_{av}} \end{bmatrix} +
$$
$$
j\omega\sqrt{\mu\epsilon} \begin{bmatrix} \chi_{me}^{xx} & \chi_{me}^{xy} \\ \chi_{me}^{yx} & \chi_{me}^{yy} \end{bmatrix} \begin{bmatrix} E_{x_{av}} \\ E_{y_{av}} \end{bmatrix}
$$
(6.1b)

As this unit cell shows highly decoupled polarizations, it can be assumed that the susceptibility tensors are diagonal, which implies that all χ^{yx} and χ^{xy} components are zero. Furthermore, as the metafilm unit cell is essentially transversely symmetric, χ^{xx} and χ^{yy} are identical, resulting in the number of unknown parameters being reduced to four: χ_{ee}^{xx}, χ_{em}^{xx}, χ_{me}^{xx} and χ_{mm}^{xx}. ΔH and ΔE in (6.1a)–(6.1b) refer to the jump in the E-/H-field values at the two sides of the metafilm, and E_{av}/H_{av} refer to the average values of these fields [135]. Therefore, the following definitions can be used to simplify these equations (superscripts i = incident; r = reflected; t = transmitted):

$$E_{av} = \frac{E^t + (E^i + E^r)}{2} \tag{6.2a}$$

$$\Delta E = E^t - (E^i + E^r) \tag{6.2b}$$

$$H_{av} = \frac{H^t + (H^i + H^r)}{2} \tag{6.2c}$$

$$\Delta H = H^t - (H^i + H^r). \tag{6.2d}$$

Consequently,

$$\frac{E_{av}}{E_i} = \frac{T + (1 + R)}{2} \tag{6.3a}$$

$$\frac{\Delta E}{E_i} = T - (1 + R) \tag{6.3b}$$

$$\frac{H_{av}}{H_i} = \frac{T + (1 - R)}{2} \tag{6.3c}$$

$$\frac{\Delta H}{H_i} = T - (1 - R), \tag{6.3d}$$

where T and R are the transmission and reflection parameters of the metafilm, respectively, obtained at normal incidence. Inserting (6.3) in (6.1) results in the extraction of the susceptibility parameters as follows:

$$\chi_{ee} = -\frac{2}{j\omega\epsilon\eta}$$

$$\frac{(T_{TM} + R_{TM} - 1)\frac{T_{TM}-R_{TM}+1}{T_{TE}-R_{TE}+1} + (T_{TE} + R_{TE} - 1)}{(T_{TM} + R_{TM} + 1)\frac{T_{TM}-R_{TM}+1}{T_{TE}-R_{TE}+1} + (T_{TE} + R_{TE} + 1)}$$

(6.4a)

$$\chi_{em} = -\frac{2}{j\omega\sqrt{\mu\epsilon}}$$

$$\frac{(-T_{TM} - R_{TM} + 1)\frac{T_{TE}+R_{TE}+1}{T_{TM}+R_{TM}+1} + (T_{TE} + R_{TE} - 1)}{-(T_{TE} - R_{TE} + 1)\frac{T_{TE}+R_{TE}+1}{T_{TM}+R_{TM}+1} + (-T_{TM} + R_{TM} - 1)}$$

(6.4b)

$$\chi_{me} = -\frac{2}{j\omega\sqrt{\mu\epsilon}\eta}$$

$$\frac{(-T_{TM} - R_{TM} - 1)\frac{T_{TM}+R_{TM}+1}{T_{TE}+R_{TE}+1} + (T_{TE} - R_{TE} - 1)}{(T_{TM} - R_{TM} + 1)\frac{T_{TM}+R_{TM}+1}{T_{TE}+R_{TE}+1} + (T_{TE} - R_{TE} + 1)}$$

(6.4c)

$$\chi_{mm} = -\frac{2}{j\omega\mu}$$

$$\frac{(-T_{TM} + R_{TM} + 1)\frac{T_{TE}-R_{TE}+1}{T_{TM}-R_{TM}+1} + (T_{TE} - R_{TE} - 1)}{(T_{TE} + R_{TE} + 1)\frac{T_{TE}-R_{TE}+1}{T_{TM}-R_{TM}+1} + (T_{TM} + R_{TM} + 1)}.$$

(6.4d)

In these equations, TE and TM refer to the two different polarizations of excitation assuming an X-Z plane of incidence. Thereafter, scattering parameters obtained for the fully printed unit cell through full-wave simulations are supplied to (6.4a)–(6.4d), and the susceptibility parameters are extracted. The extracted parameters presented in Fig. 6.6 show values of χ_{ee} that are between 1 and 5 orders of magnitude greater as compared to other susceptibility components at resonance, and are in agreement with the electric-dipole-like current distribution in Fig. 6.7, plotted at the resonance frequency. Furthermore, the reversed directions of the electric currents between the disc and liner regions are consistent
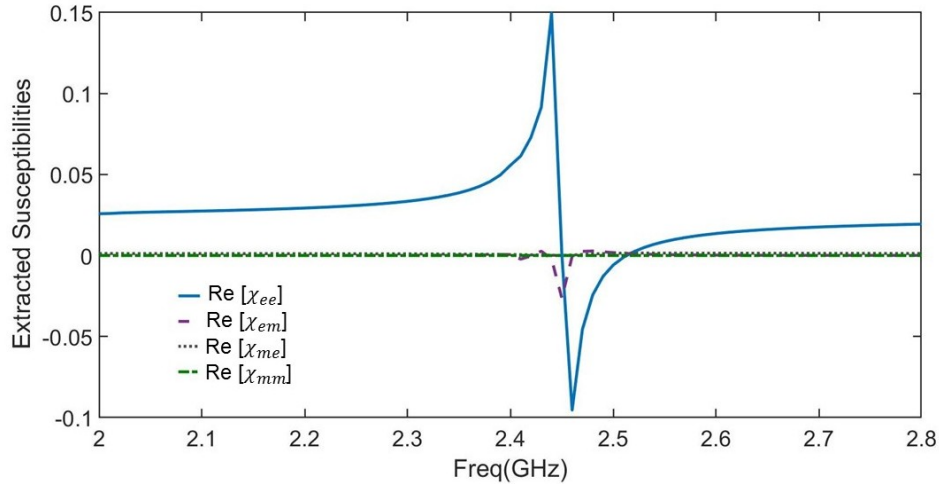
FIGURE 6.6: Extracted susceptibility parameters using (6.4a)–(6.4d) for the
fully printed metafilm unit cell shown in Fig. 6.2 (a).

with the assumption that the transmission-line mode is the dominant mode in the liner

region. The data in Fig. 6.6 also imply that this unit cell shows only negligible levels of

bianisotropy.

To validate the extracted susceptibilities shown in Fig. 6.6, a homogenized slab of an

electrically very small thickness of $d = 2$ mm ($\sim\lambda/62$ at 2.44 GHz) whose parameters

are defined as $\epsilon = \epsilon_0(1 + \chi_{ee}/d)$, and $\mu = \mu_0(1 + \chi_{mm}/d)$ is simulated, and the corre-

sponding S-parameters are shown in Fig. 6.8 along with those of the fully printed design.

Both sets of data are obtained for an infinitely large metafilm illuminated by a normally

incident plane wave through full-wave HFSS simulations. The strong agreement between

the two sets of data validates the extracted parameters. Furthermore, as expected, this

homogenized sheet model is much easier and faster to simulate.
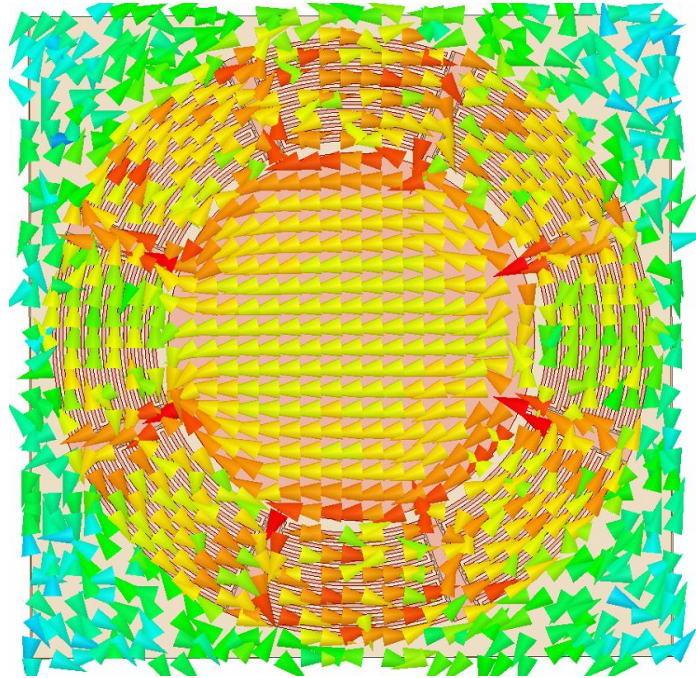
FIGURE 6.7: Vector electric currents plotted for the fully printed metafilm unit cell at the resonance frequency of 2.44 GHz.
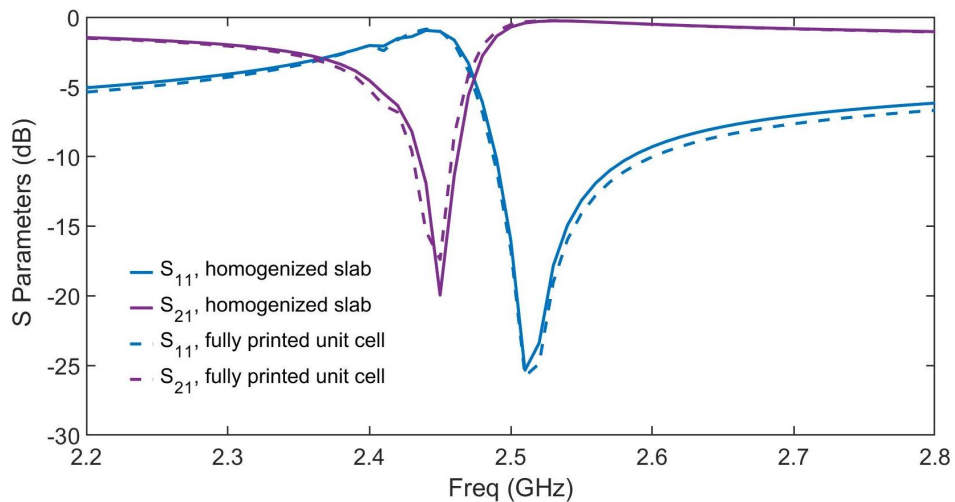
FIGURE 6.8: Scattering parameters obtained for a thin homogenized slab of thickness $d = 2$ mm ($\sim\lambda/62$ at 2.44 GHz) whose parameters are defined as $\epsilon = \epsilon_0(1 + \chi_{ee}/d)$, and $\mu = \mu_0(1 + \chi_{mm}/d)$ versus the S-parameters of the actual design plotted in dashed.

6.5 Parametric studies

Some parametric studies are performed on the design parameters of the proposed metafilm unit cell so as to provide insight into controlling the resonance frequency of this unit cell. Furthermore, these studies help in establishing a better understanding of the underlying mechanism of the observed resonance.

6.5.1 Periodicity

In this study, the periodicity P is varied from 18 mm to 22 mm in 2-mm steps, while the unit cell design is kept unchanged. The corresponding S_{11} data presented in Fig. 6.9 show that there is only a small frequency upshift when P is increased. Changing the periodicity has minimal effect on the resonance frequency because the proposed metafilm unit cells exhibit strongly isolated resonances. Increasing P also slightly decreases the level of reflection, as it implies smaller filling fraction of metal in each unit cell.

6.5.2 Unit-Cell Size

The data presented in Fig. 6.10 are obtained when the outer radius b is decreased from 8.5 mm to 6.5 mm in 1-mm steps. A decrease in b (keeping liner thickness unchanged) shifts the resonance frequency up for two different reasons: i) smaller resonator size, and ii) decrease in the amount of printed capacitive loading, which will push the f_{mp} of the
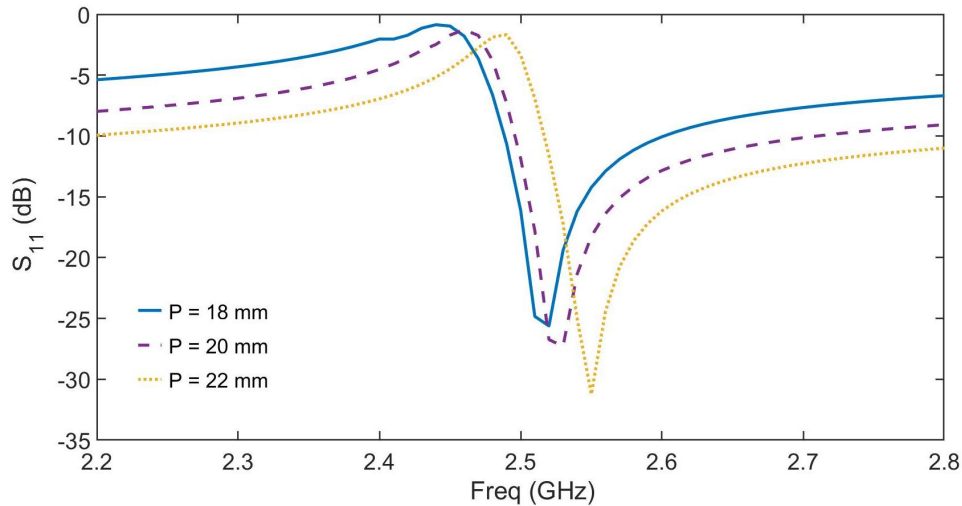
FIGURE 6.9: S_{11} of the metafilm design when periodicity (P) is varied from 18 mm to 22 mm, in 2-mm steps.

liner to higher frequency regimes. This study reveals that b is a major design parameter to control the operating frequency of the metafilm.

6.5.3 Capacitive Loading

Next, the effect of capacitive loading is studied by changing the printed capacitor's span θ from $32°$ to $40°$ in $4°$ steps. As is evident from the data in Fig. 6.11, the amount of capacitive loading controls the resonance frequency as well as the degree of miniaturization (as outer radius b and unit-cell size P are kept constant). These data also emphasize that capacitor span (θ) is another major parameter for controlling the resonance frequency of
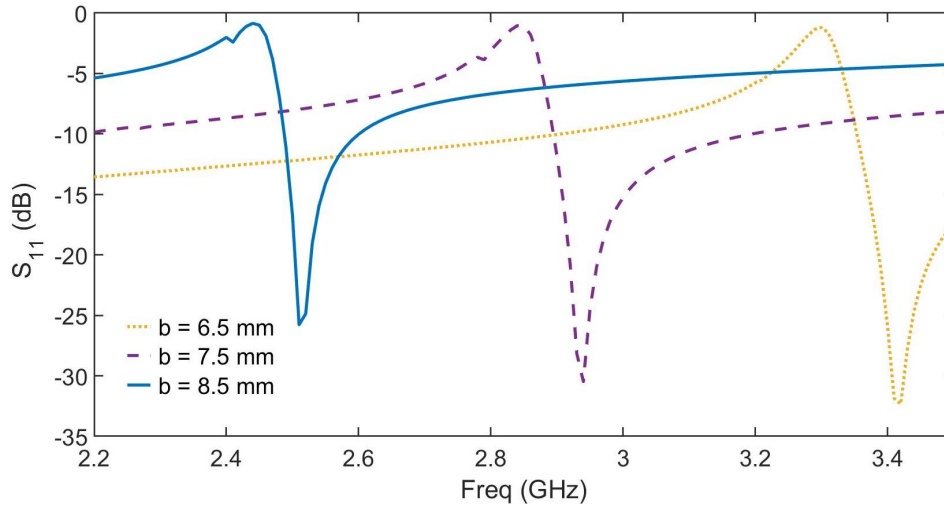
FIGURE 6.10: S_{11} of the metafilm design when outer radius (b) is varied from 6.5 mm to 8.5 mm, in 1-mm steps.

the proposed metafilm design. By increasing C, the plasma frequency in the Drude dispersion model of the permeability of the liner is reduced, resulting in lower MNNZ frequency regimes, and therefore, lower resonance frequencies (i.e., higher degrees of miniaturization). Utilizing fully printed capacitors provides precise control over the operating frequency.

6.6 Oblique Incidence Studies

Figures 6.12(a) and 6.12(b) show the reflection parameters of the proposed metafilm for TE- and TM-polarized incident waves, respectively, when the angle of incidence is swept from normal to 60° in steps of 15°. As the unit cells presented in this work are strongly miniaturized and measure $\lambda/7$ at resonance, they show a stable response when the angle
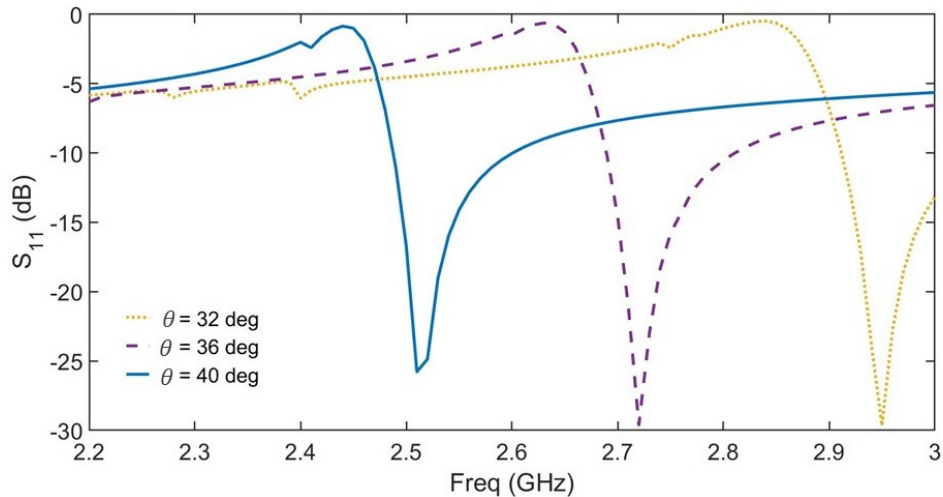
FIGURE 6.11: S_{11} of the metafilm design obtained when the capacitor span (θ)
is swept from $32°$ to $40°$, in $4°$ steps.

of incidence is increased towards grazing angles. This behaviour would not be achieved

through arrays with electrically large unit cells.

6.7   Fabrication and Measurement

To verify the shielding response of the proposed metafilm design, a 16×12 array was

fabricated using an LPKF ProtoLaser U3 laser-milling machine. Figure 6.13 shows the

fabricated prototype, along with an inset at the top-right corner magnifying one fabri-

cated unit cell. The number of unit cells in the array was chosen to maximize the use of

space on an available 9-in $\times$ 12-in substrate panel. The substrate used for fabrication is

Rogers RT/Duroid 5880 with 17-μm copper cladding thickness, which matches that used

in simulations. The fabricated structure measures $1.7\lambda \times 2.3\lambda$ at the resonance frequency.
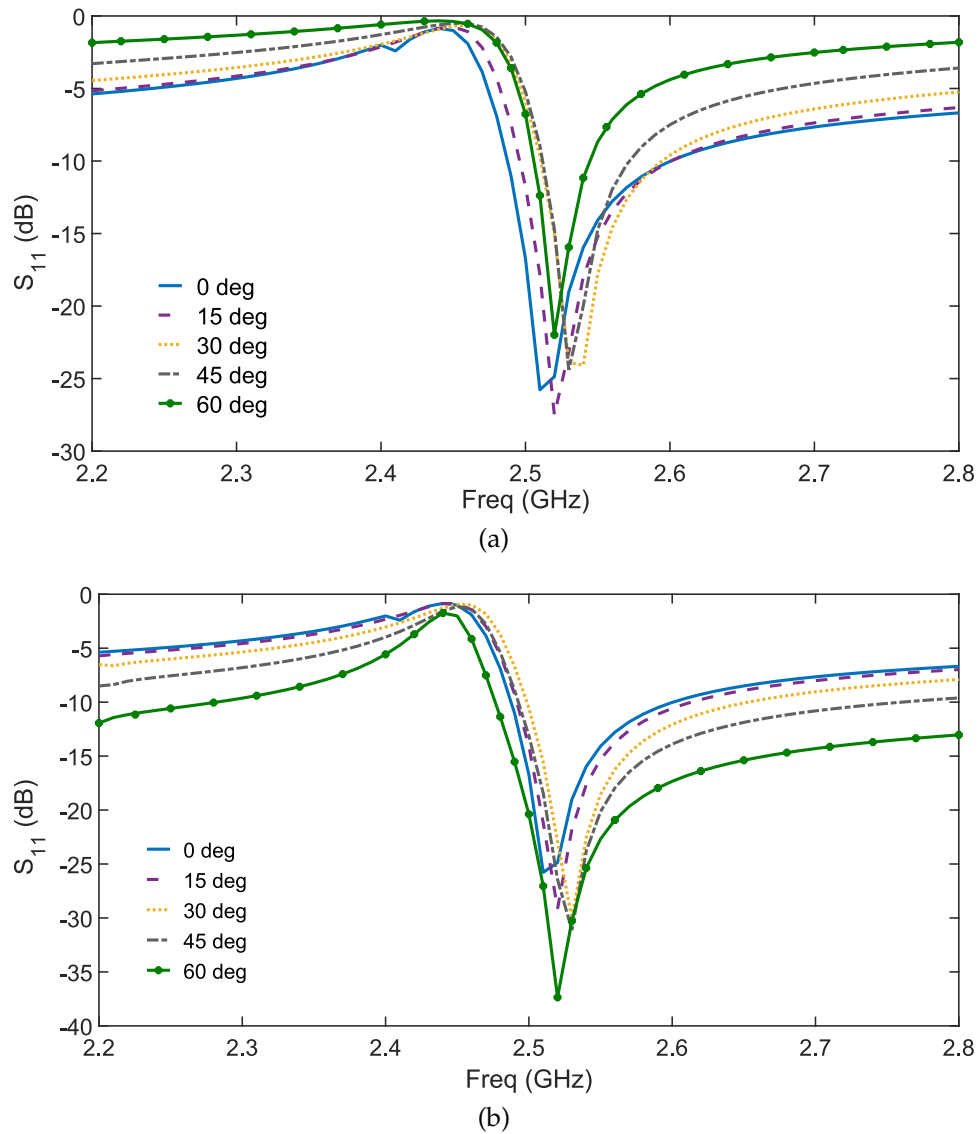
FIGURE 6.12: Reflection parameter of the fully printed metafilm when the angle of incidence is swept from normal to 60° in 15° steps for (a) TE-polarized incident waves, and (b) TM-polarized incident waves.
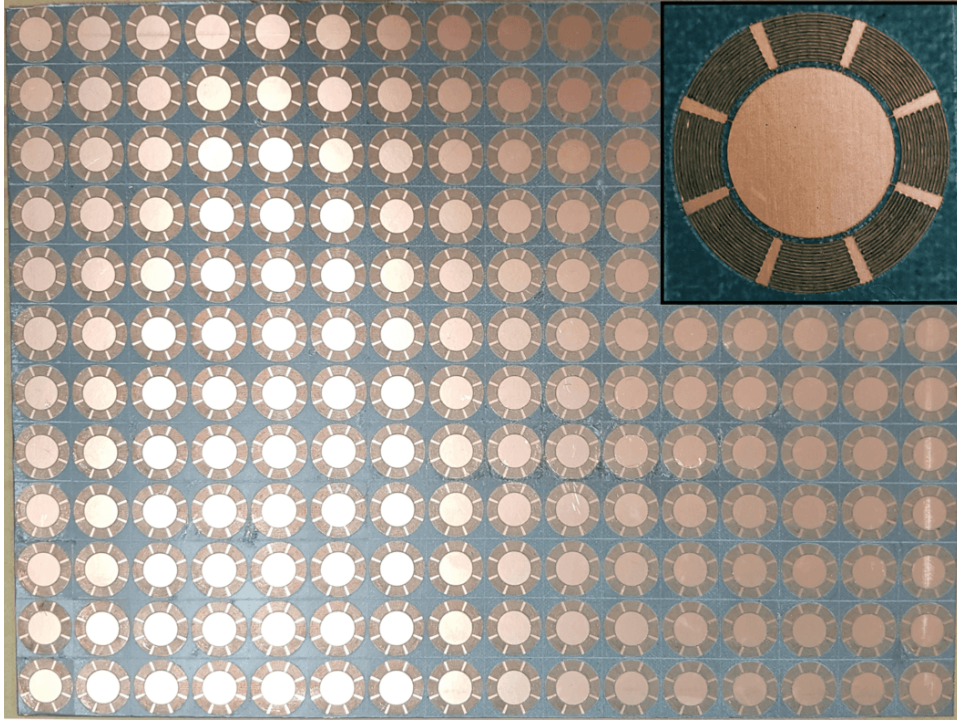
FIGURE 6.13: The fabricated 16×12 metafilm array possessing an overall size of $1.7\lambda \times 2.3\lambda$ at the center frequency.

Figure 6.14 depicts the experimental setup in an ETS-Lindgren shielded fully anechoic chamber, picturing the double-ridged horn (DRH) antenna probe on the left-hand side and the WR-340 standard-gain horn (SGH) antenna on the right-hand side, placed at a distance of 166 cm (i.e., 14λ) from each other. The metafilm array is inserted at a distance of 39 cm from the DRH antenna (implying a distance of 127 cm from the SGH antenna). These distances are chosen as close to the far-field distances of the two antennas as possible within the space afforded by the chamber, so as to realize a plane-wave-like excitation. This experimental setup has been designed for measuring the S_{21} parameter of the

proposed metafilm, as this parameter proves easier to experimentally validate. As the

simulation data in Fig. 6.3 demonstrate that this metafilm is generally low-loss, it can be

concluded that a reduction in S_{21} implies an increase in S_{11}. Furthermore, these data need

to be properly normalized prior to comparison with the simulation data due to the finite

size of the fabricated array versus the infinite array modeled in simulations. To do this,

a large screen covered with absorbers was built with a window of the same size as the

fabricated metafilm design in the center. The transmission parameter was then obtained

with the fabricated design inserted into the window, and normalized to the corresponding

values measured in its absence.

The measured S_{21} is presented in Fig. 6.15 (solid curve) along with the simulated

data (dashed curve). Although the two sets of data are in strong agreement in terms of

trend and contrast, the measured data demonstrate a 95 MHz (3.9%) frequency upshift

compared to the simulation data. This upshift may be attributed to an effective reduction

in the value of the interdigitated capacitors caused by fabrication tolerances. In fact, a

precise study of one unit cell through white-light interference profilometry demonstrates

an effective trace width of 95 μm (i.e., a gap width of 105 μm) instead of the desired value

of 100 μm caused by the Gaussian beam shape of the milling laser, as well as an effective

copper thickness of 13 μm instead of the simulated value of 17 μm. The original simulation

was repeated according to these measured parameters, and the resulting data are shown

in the dotted black curve in Fig. 6.15. The new data show much better agreement with the
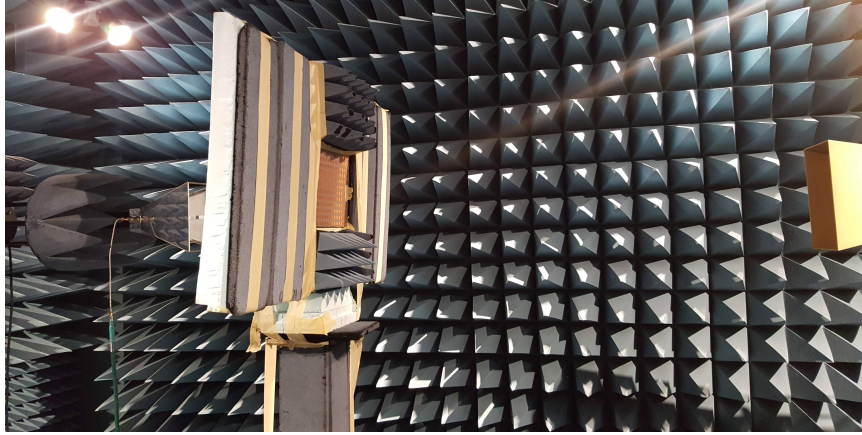
FIGURE 6.14: The measurement setup in an antenna anechoic chamber with the double-ridged horn antenna probe on the left hand side and the WR-340 standard gain horn (SGH) antenna on the right-hand side, placed at a distance of 166 cm (i.e., 14λ) from each other. The fabricated prototype is inserted between the two antennas at a distance of 39 cm from the ridged horn.

measured data. A bandstop response is observed at approximately 2.5 GHz, providing better than 18-dB decrease in transmission.

6.8 Applications

The proposed metafilm unit cell may be made extremely subwavelength. This property can be exploited through the design of inhomogeneous partially transmitting and/or reflecting surfaces for beam-shaping with extremely high-spatial-resolution control of the transmitted and/or reflected fields. This metafilm is also beneficial for selective shielding applications that require a compact array due to a limited available space, or need the array to remain transparent outside a narrow shielding band. They can also be utilized
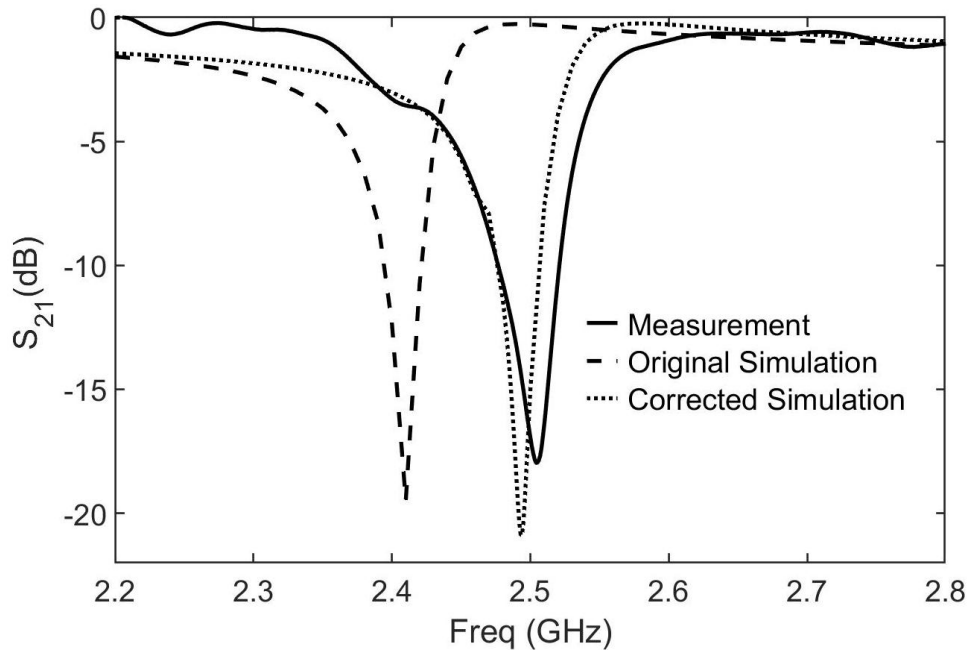
FIGURE 6.15: The normalized measured data plotted against the original simulation data (dashed curve) and the corrected simulation data (dotted curve).

for the design of far-field, high-resolution magnifying devices following the approach reported in chapter 5. Moreover, this unit cell can be made polarization sensitive and/or dual-band by judicious changes in the MNNZ liner design. The circular-shaped geometry of this unit cell along with its subwavelength size provides maximum adaptability for applications that require conformal metasurfaces (MTSs) [189]. Frequency insensitivity with respect to the periodicity and the angle of incidence are also advantageous for many applications.

Chapter 7

Dual-Band and Polarization-Selective Shielding Using Anisotropic Metafilm Unit Cells

Metasurfaces (MTSs) and frequency selective surfaces (FSSs) with a dual-band response have recently been receiving great attention for various applications. In particular, EMI shielding for GSM or ISM bands or wireless LAN applications may benefit from dual-band compact MTSs/FSSs. Generally, the development of wireless and portable communication devices raises the concern of device malfunction caused by unwanted interference of electromagnetic waves. These EMI issues become especially hazardous when occurring in medical environments [190]. Many works have explored the design of dual-band MTSs and FSSs during the last few years [40, 191–197]; however, the proposed designs suffer from different drawbacks, such as a large overall size, the need to pattern

both sides of the substrate, lack of independent control of the operating bands, unstable response for larger oblique angles of incidence, not being fully transparent outside of the shielding band, and/or not demonstrating the desired polarization selectivity. One important challenge in many applications is designing for unit cells that are highly subwavelength with respect to the operating wavelength, as they provide stable performance with respect to the angle of incidence. Miniaturized rectangular-loop unit cells have been widely explored to achieve extreme miniaturization. However, the existing works are sometimes difficult to implement and/or possess various limitations. For example, a dual-band miniaturized-element FFS is introduced in [198] based on rectangular meandered-loop elements. Although the unit cells are well miniaturized ($\lambda/11$ and $\lambda/5$) at the two operating frequencies, the proposed structure needs patterning of the two metallic layers separated by a dielectric spacer. Furthermore, the two operating bands cannot be controlled independently. Another dual-band miniaturized-element FSS unit cell operating at WLAN frequencies is introduced in [199], which provides dual-band behaviour with a single-layer structure; however, independent control of operating frequencies is only possible for the upper frequency band, and only in a very small frequency range. Another challenge in such designs is achieving closely spaced operating bands. Two unit cells with different operating frequencies are integrated to construct a dual-band miniaturized-element FSS unit cell in [200], where arrays of metallic vias are used to form a Faraday cage

structure and minimize the coupling between the two unit cells. This results in fabrication complexity, and the obtained ratio between the operating bands become only as small as 1.4. This ratio is improved to 1.36 in [201] to realize operating bands at 1.8 GHz and 2.45 GHz, at the cost of added fabrication complexity as the unit cells are placed in a substrate integrated waveguide cavity structure to eliminate the unwanted coupling effects. In this work, operating bands with a frequency ratio of 1.28 are achieved without any need for the use of vias. In fact, the operating bands in this work are highly decoupled and can be placed much closer to each other if needed.

In this chapter, two dual-band, polarization-selective metafilm designs are introduced, which perform as dual stop-band filters at the representative operating frequencies of 1.8 GHz and 2.4 GHz. Both designs are dual-band and highly subwavelength, but they exhibit different polarization selectivities. The first dual-band design demonstrates two bands that both respond to one polarization of incidence, while remaining transparent for the other (perpendicular) polarization. The second dual-band design also offers two operating bands, with the difference that these bands respond to different polarizations of incidence. Both designs show angular stability for incidence angles up to $60°$. Furthermore, the operating bands can be tuned independently.

7.1 Theory

The proposed dual-band metafilm designs are obtained through circular metallic discs lined using magnetic metamaterial (MTM) liners. It was shown in chapter 6 that extremely subwavelength metafilm unit cells can be realized through miniaturized metallic disc resonators loaded using μ-negative and near-zero (MNNZ) liners. This was achieved by reducing the resonance frequency of the fundamental EH_{11} mode, and the MNNZ property of the liner was achieved using capacitively loaded, azimuthally directed copper traces. Here, we show that μ-positive and large (MPL) liners can be utilized to obtain subwavelength metafilm unit cells in the same manner. As the two MNNZ-lined and MPL-lined unit cells show different polarization selectivities, they may be combined for development of dual-band designs. The MPL liner technology is inspired by the idea of miniaturizing loop resonators through meandering. A simple, unloaded loop would resonate at frequencies where its overall length measures multiples of λ, where λ is the wavelength at the operating frequency. This length corresponds to formation of two bent electric dipoles, each possessing a length of $\lambda/2$ [202]. This frequency can be reduced by adding to the overall current path length by means of meandering, or alternatively, loading the ring using inductors. To the best of our knowledge, only two related works have investigated the design of miniaturized-element MTSs based on circular-loop-shape unit cells [202, 203]. In the present work, fully printed, dual-arm spiral inductors are used to load a ring-shaped resonator, which acts as an MPL liner to a metallic disc. Although
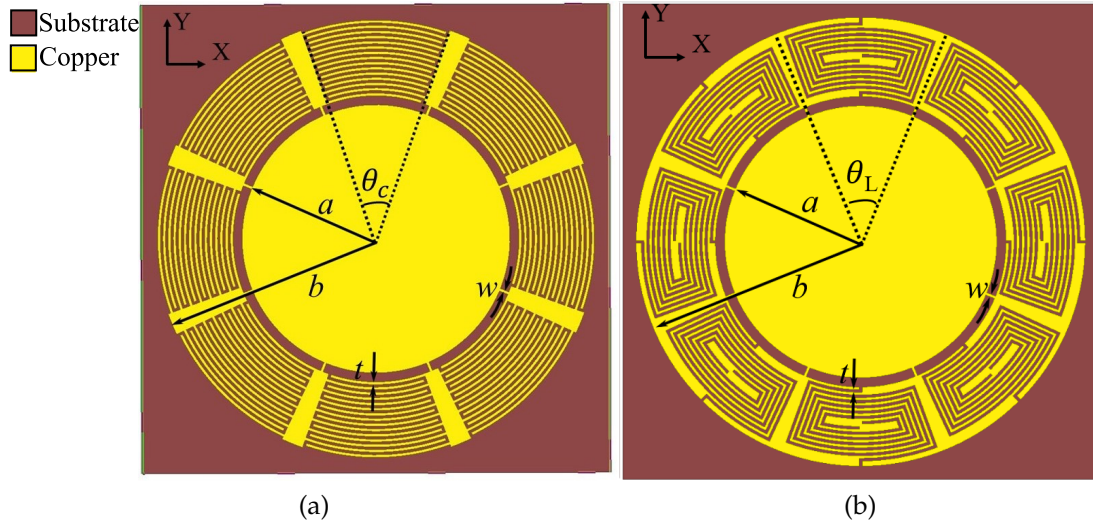
FIGURE 7.1: Single-band, polarization-insensitive metafilm unit cells possess-
ing 8 interdigitated capacitors (a) or spiral inductors (b).

the presence of the inner metallic disc is not crucial to the operation of this MPL-lined

unit cell, the first unit cell possessing an MNNZ liner requires the inner disc to resonate,

and the ultimate dual-band MTS unit cell is obtained by combining the two (MNNZ and

MPL) liners. Therefore, the presence of the metallic disc is necessary for the design of the

dual-band MTS unit cell.

The first metafilm unit cell is demonstrated in Fig. 7.1(a), and pictures a PEC disc lined

using a layer of MNNZ MTM liner (previously discussed in chapter 6). The MNNZ liner is

realized by means of series interdigitated capacitors loading the exterior ring region, and

shunt inductive stubs connecting the outer ring and inner disc regions. The resonance

mechanism in this unit cell is based on reduced resonance modes of a disc resonator, as

studied in chapter 6. The second resonant metafilm unit cell is shown in 7.1(b), which

looks very similar to the unit cell shown in Fig. 7.1(a), where the interdigitated capacitors are replaced with spiral inductors. Whereas the two designs might look identical at first glance except for different printed loading elements, they are, in fact, very different. The series spiral inductors form a liner that possesses a large and positive permeability, and the MPL liner reduces the resonance frequency of the outer loop by adding to the current path length. Both metafilm unit cells shown in Fig. 7.1 reflect strongly at their resonance frequency, and exhibit a Fano-shape profile of reflection.

These metafilm unit cells can be made polarization-sensitive by reducing the number of loading capacitors/inductors from eight to two. Figure 7.2 demonstrates the schematics of these polarization-sensitive unit cells. A smaller number of loading elements also allows increase of the span (θ) of the remaining capacitor/inductor elements, and therefore, further miniaturization of the unit cells [see the parametric study on the capacitor span (θ) shown in Fig. 6.11]. Furthermore, the resulting unit cells respond to different polarizations of incidence. Whereas the metafilm unit cell shown in Fig. 7.2(a) responds to an X-directed electric field of excitation, the unit cell shown in Fig. 7.2(b) may be excited through a Y-directed electric field of excitation. In each case, the other polarization passes through the metafilm with small insertion loss and no resonance behaviour. The polarization selectivity of the unit cell shown in Fig. 7.2(a) is governed by the need for series capacitive loading to realize the MNNZ liner property, which is realized by an X-directed electric field of excitation. The polarization selectivity of the unit cell shown in Fig. 7.2(b),

however, is a function of the amount of inductive loading that the proposed printed inductor provides under different polarizations of excitation, as this loading inductor does not possess an X-Y symmetric geometry. Therefore, it can respond to an X-directed electric field of excitation too, although at a generally different (and higher) frequency range.

Interesting phenomena can be obtained by combining these two metafilm unit cells. Figure 7.3(a) shows a dual-band unit cell obtained by integrating the two MTM liner technologies shown in figures 7.2(a) and 7.2(b) in one unit cell. The underlying idea is that if the axis of one pair of these loading elements is rotated 90° with respect to the other, they will both respond to the same polarization of excitation (i.e., X-directed polarization of incidence for the depicted unit cell), but generally at different frequencies with highly decoupled resonance frequencies. The two resonance frequencies may also be overlapped for the purpose of obtaining a broader single-band response. The other (i.e., Y-directed) polarization of incidence would pass through this metafilm with negligible amounts of insertion loss; therefore, this metafilm acts like a dual-band shielding device for X-polarized incident waves.

Figure 7.3(b) demonstrates a second dual-band unit cell where pairs of printed interdigitated capacitors are used on different (i.e., X and Y) axes of the unit cell, with different values realized through the use of different capacitor spans. A dual-band operation can be inferred from different values of capacitor spans. Furthermore, based on the above
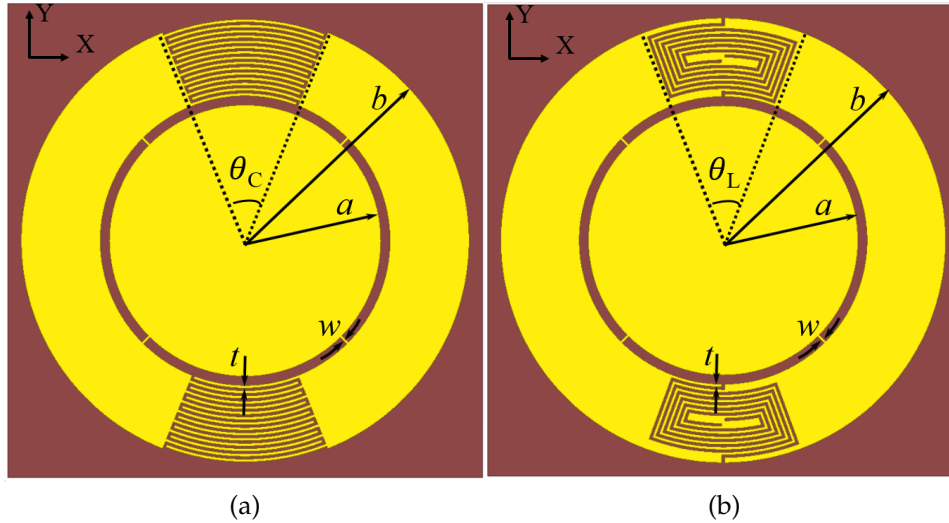
FIGURE 7.2: Single-band, polarization-sensitive metafilm unit cells possessing 2 interdigitated capacitors (a) or spiral inductors (b).

discussion on polarization sensitivity of these printed capacitors, the capacitor pair located on the vertical axis responds to an X-directed electric field of excitation, while the capacitors on the horizontal axis respond to a Y-directed electric field of excitation. This implies that the two bands respond to differently polarized incident waves. Therefore, the metafilm realized using this unit cell will act as a dual-band shielding device for two different polarizations of incident waves, at generally different frequencies. In each band, the cross-polarized wave would pass through the unit cell with a minimal amount of insertion loss. Although not shown, the same behaviour could be achieved through the MPL liner technology if printed spiral inductors are used instead.
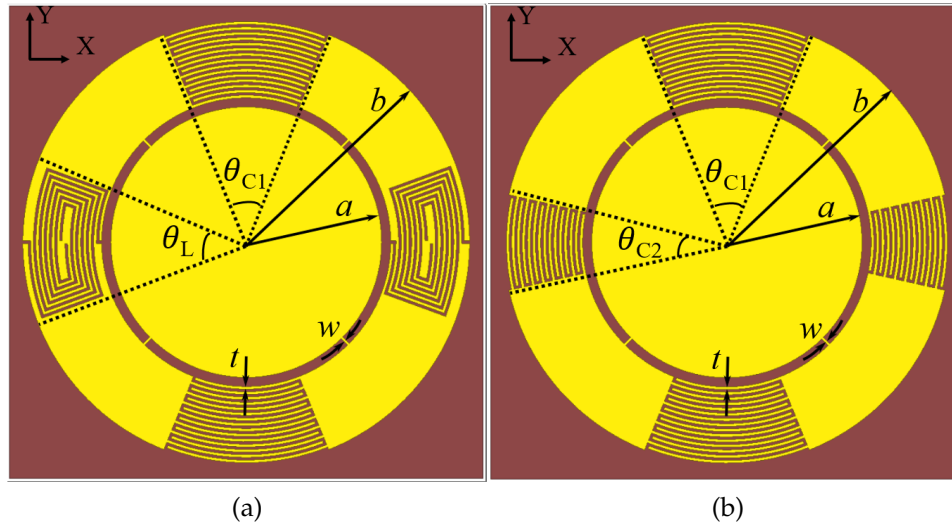
FIGURE 7.3: Dual-band, polarization-selective metafilm unit cells possessing (a) one pair of loading interdigitated capacitors on the vertical axis and one pair of spiral inductors on the horizontal axis, and (b) two pairs of interdigitated capacitors on different axes of the unit cell.

7.2 Designs and Simulations

Figures 7.4(a) and 7.4(b) demonstrate transmission and reflection parameters obtained through full-wave HFSS simulations for an infinite array of the two metafilm unit cells previously shown in figures 7.3(a) and 7.3(b), respectively, each illuminated using a normally incident plane wave. In each figure, solid and dashed linestyles are used for plotting reflection and transmission parameters, respectively. Furthermore, different markers (stars and dots) are used to label the data corresponding to different polarizations of incidence. The scattering parameters of an infinite unlined metallic disc array of the same size are plotted for reference in curves with no markers. In all figures, polarization 1 refers to an X-directed electric field of incidence, while polarization 2 refers to a

Y-polarized electric field of incidence. The design parameters are as follows: $b = 8.5$ mm, $a = 5.15$ mm, $w = 0.1$ mm, $t = 0.1$ mm, $\theta_{c_1} = 44°$, $\theta_L = 40.2°$, and $\theta_{c_2} = 25.4°$. Capacitor/inductor spans are chosen such that both metafilm designs possess two bands located around 1.8 GHz and 2.4 GHz. The substrate used in each array is a Rogers/Duroid 5880 substrate ($\epsilon_r = 2.2$, $\tan \delta = 0.0009$) of 1.524-mm thickness, metallized on one side with copper of thickness 17 μm.

As is evident from the data in Fig. 7.4(a), resonance effects are observed at 1.82 GHz and 2.33 GHz in the curves with star markers corresponding to the metafilm design shown in Fig. 7.3(a), illuminated using an X-polarized plane wave. The discs are extremely subwavelength, and measure approximately $\lambda/9.7$ and $\lambda/7.6$ in diameter at 1.82 GHz and 2.33 GHz, respectively. The reflection parameter shows a Fano-shape resonance profile at both operating bands, and the transmission parameter experiences a minimum at each band. Reductions of about 11 dB and 12 dB are observed in the transmission parameter at the lower and upper bands, respectively, compared to the unloaded-disc array. Furthermore, transmission enhancements of 0.5 dB and 1 dB compared to the unlined disc array are obtained slightly above the antiresonance frequencies at 1.87 GHz and 2.43 GHz, respectively. The transmission levels remain high in broadband frequency regions above each resonance.

The curves with star markers in Fig. 7.4(b) corresponding to the dual-band design shown in Fig. 7.3(b) exhibit a stop-band at 1.82 GHz for an X-polarized incident plane
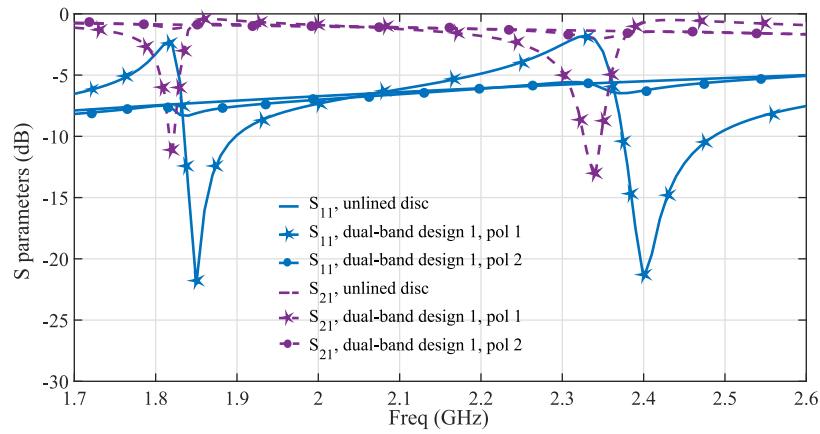
(a)
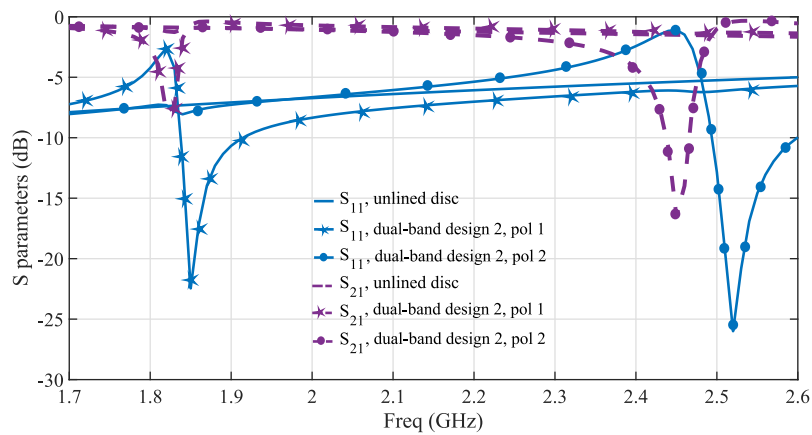
(b)
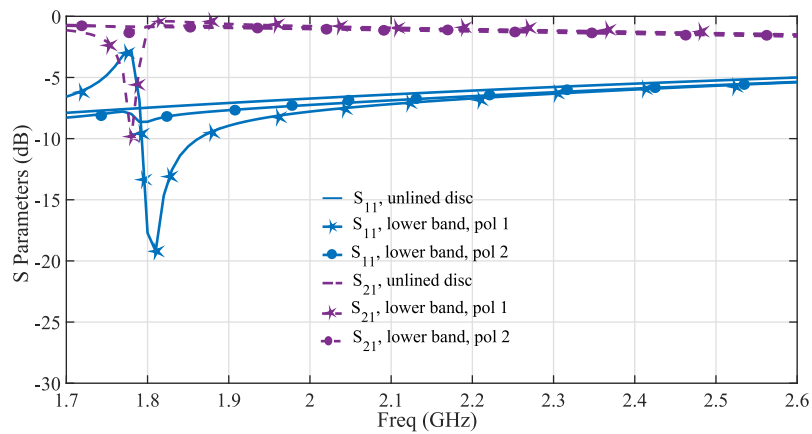
(c)

FIGURE 7.4
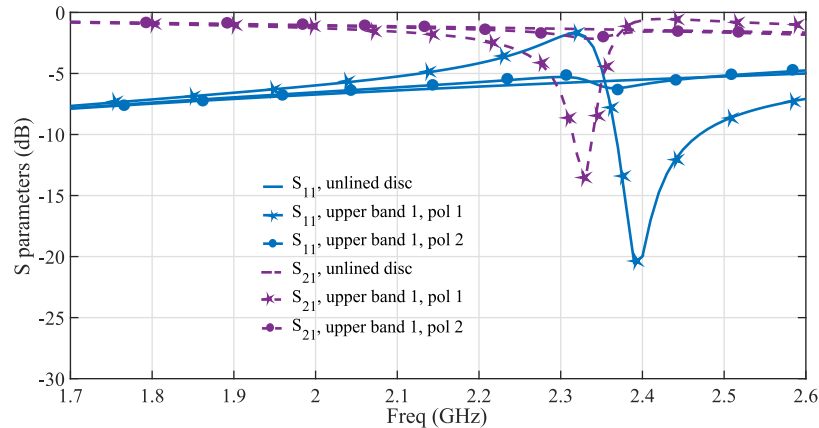
(d)
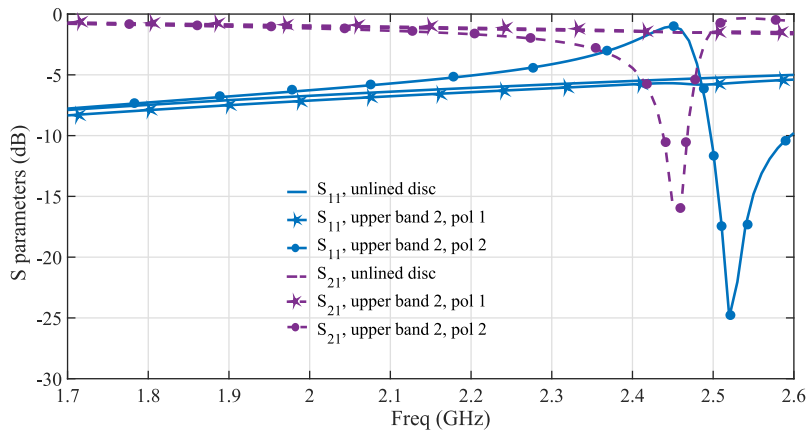
(e)

FIGURE 7.4: Scattering parameters for an infinite array of (a) the dual-band metafilm design shown in Fig. 7.3(a), (b) the dual-band metafilm design shown in Fig. 7.3(b), (c) the single-band design obtained by shorting out the loading elements on the horizontal axis of either dual-band metafilm unit cell, (d) the single-band design obtained by shorting out the loading elements on the vertical axis of the dual-band metafilm unit cell shown in Fig. 7.3(a), and (e) the single-band design obtained by shorting out the loading elements on the vertical axis of the dual-band metafilm unit cell shown in Fig. 7.3(b). In each case, the scattering parameters are shown for both X- and Y-polarized normally incident plane waves.

wave. Another shielding band is observed at 2.45 GHz for the same metafilm design illuminated using a Y-polarized plane wave. Similar to the previous metafilm design, the reflection parameters undergo Fano-shape resonance profiles at both resonance frequencies, and the transmission level remains high in a broadband frequency region above each resonance. A 7 dB reduction in transmission is observed at the lower shielding band compared to the unloaded disc array, while this value measures 15 dB at the upper shielding band. Increased transmission values of 0.55 dB and 1.26 dB compared to the unlined disc array are measured slightly above the antiresonance frequencies at 1.87 GHz and 2.54 GHz, respectively.

The transmission/reflection parameters of the single-band designs obtained by shorting out one pair of loading elements at a time in the dual band unit cells shown in Fig. 7.3 are also obtained for different polarizations of incidence, and plotted against those of the unlined disc array in figures 7.4(c)-7.4(e). Consistent linestyles and markers are used so that the data are easily comparable to those shown in figures 7.4(a)-7.4(b). Figure 7.4(c) demonstrates the scattering parameters of the single band design obtained by shorting out the loading elements on the horizontal axis of either dual-band unit cell (note that the interdigitated capacitors on the Y axis of the proposed dual-band unit cells are identical). A Fano-shape resonance is observed in the reflection parameter of the resulting single-band design at 1.78 GHz as observed in Fig. 7.4(c) for a X-polarized incident plane wave (i.e., polarization 1). These data prove that the interdigitated capacitors placed on the vertical

axes of the proposed dual-band metafilm unit cells govern the lower-frequency shielding bands in both designs. The scattering parameters shown in Fig. 7.4(d) are obtained by shorting out the interdigitated capacitors on the vertical axis of the unit cell shown in Fig. 7.3(a). These data confirm that the upper operating band in the response of the first dual-band design is caused by the presence of the spiral loading inductors only, and therefore, may be controlled by modifying the value of inductive loading. Lastly, Fig. 7.4(e) exhibits the response of the single-band design obtained by shorting out the interdigitated capacitors on the vertical axis of the unit cell shown in Fig. 7.3(b), while maintaining the other pair of loading capacitors. The data confirm that the operating frequency as well as polarization dependence of the upper frequency band for this dual-band unit cell are determined through the value and placement of interdigitated capacitors located on the horizontal axis of the proposed unit cell.

The data in figures 7.4(c)-7.4(e) also confirm that operating frequencies are largely decoupled, and only small upshifts in the frequency of the lower shielding band are observed as the result of integrating the single-band designs to construct the dual-band unit cells. Hence, independent control of the operating bands is possible by modifying the design parameters of the corresponding loading elements. Furthermore, smaller shielding levels are sometimes observed at the lower frequency bands, caused by the subwavelength size of the resonator at the operating frequency. Consequently, there may be a
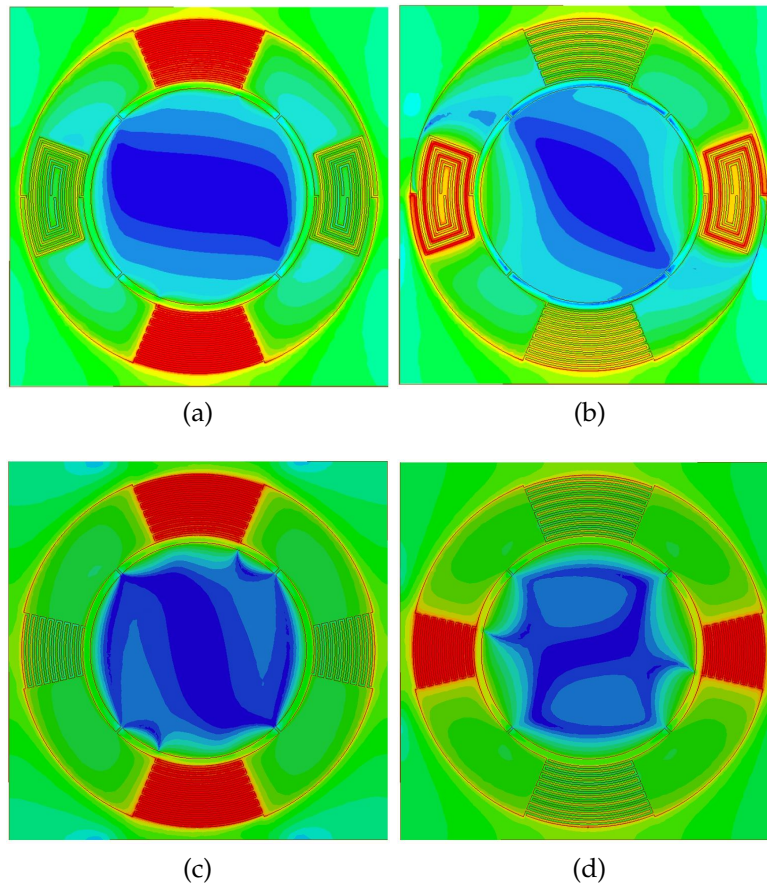
FIGURE 7.5: Complex electric-field magnitudes at (a) lower resonance frequency of the metafilm design shown in Fig. 7.3(a), (b) upper resonance frequency of the metafilm design shown in Fig. 7.3(a), (c) lower resonance frequency of the metafilm design shown in Fig. 7.3(b), and (d) upper resonance frequency of the metafilm design shown in Fig. 7.3(b).

tradeoff between shielding levels and the degree of miniaturization. Polarization selectivities prove consistent between each dual-band unit cell and its corresponding single-band designs as indicated by use of similar markers for similar polarizations in different parts of Fig. 7.4. Complex magnitudes of electric field vectors are shown in Fig. 7.5 at the lower and upper frequency bands for each dual-band metafilm design, depicting strong fields at only one pair of loading elements at each resonance frequency.

7.3 Extraction of Effective Surface Parameters

Generalized sheet transitions (GSTCs) are used to determine the electric-magnetic-dipole like behaviour of these unit cells at resonance (refer to sec. 2.7 for background on GSTCs). To extract the susceptibility components of the proposed unit cells assuming an anisotropic and diagonal susceptibility tensor, the following equations 7.1(a)-7.1(f) from [156] are used:

$$\chi_{MS}^{xx} = \frac{2j}{k_0} \frac{R_{TE}(0) - T_{TE}(0) + 1}{R_{TE}(0) - T_{TE}(0) - 1} \tag{7.1a}$$

$$\chi_{ES}^{xx} = \frac{2j}{k_0} \frac{R_{TM}(0) + T_{TM}(0) - 1}{R_{TM}(0) + T_{TM}(0) + 1} \tag{7.1b}$$

$$\chi_{MS}^{yy} = \frac{2j}{k_0} \frac{R_{TM}(0) - T_{TM}(0) + 1}{R_{TM}(0) - T_{TM}(0) - 1} \tag{7.1c}$$

$$\chi_{ES}^{yy} = \frac{2j}{k_0} \frac{R_{TE}(0) + T_{TE}(0) - 1}{R_{TE}(0) + T_{TE}(0) + 1} \tag{7.1d}$$

$$\chi_{MS}^{zz} = -\frac{\chi_{ES}^{yy}}{sin^2(\theta)} + \frac{2j\cos(\theta)}{k_0 sin^2(\theta)} \frac{R_{TE}(\theta) + T_{TE}(\theta) - 1}{R_{TE}(\theta) + T_{TE}(\theta) + 1} \tag{7.1e}$$

$$\chi_{ES}^{zz} = -\frac{\chi_{MS}^{yy}}{sin^2(\theta)} + \frac{2j\cos(\theta)}{k_0 sin^2(\theta)} \frac{T_{TM}(\theta) - R_{TM}(\theta) - 1}{T_{TM}(\theta) - R_{TM}(\theta) + 1}, \tag{7.1f}$$

In the above equations, R and T refer to the reflection and transmission parameters, respectively, of an infinite array of non-touching scatterers illuminated using a plane wave. The subscripts TE and TM refer to the polarization of the incident wave assuming an X-Z plane of incidence, 0 refers to normal incidence, and θ refers to an arbitrary oblique angle of incidence. The subscripts ES and MS of the $\bar{\chi}$ parameters imply electric-surface and magnetic-surface parameters, respectively, and the superscripts xx, yy, and zz refer to different diagonal components of the susceptibility tensor. To uniquely characterize an anisotropic metafilm with diagonal susceptibility tensors using the above equations, scattering parameters must be obtained for two different polarizations of incidence (TE and TM) as well as two different angles of incidence (normal, and one oblique incidence angle of choice). Therefore, an arbitrary oblique incidence angle of $\theta= 15°$ was chosen, and the transmission and reflection parameters were obtained for all the above-mentioned incident scenarios assuming an X-Z plane of incidence.

Figure 7.6 presents the extracted transverse χ_{ES} and χ_{MS} parameters for the dual-band unit cells shown in Fig. 7.3. As these data demonstrate, both dual-band unit cells demonstrate strong electric-dipole-like behaviour at their corresponding resonance frequencies.
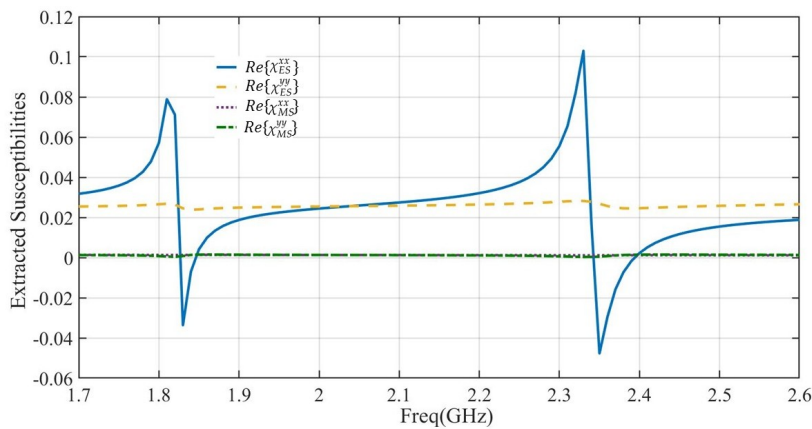
(a)
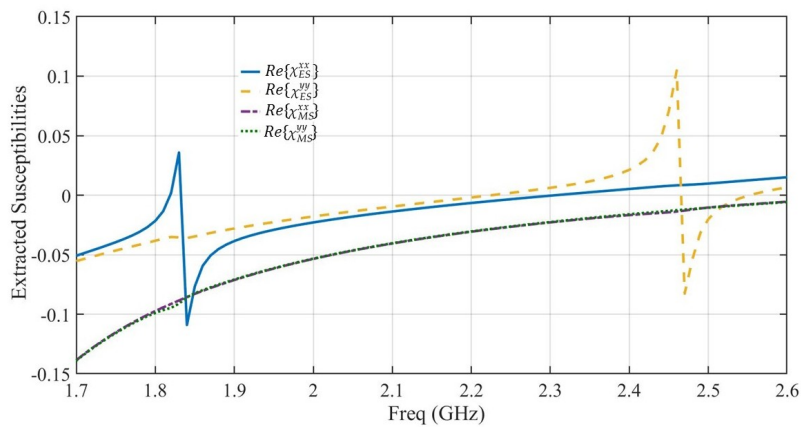
(b)

FIGURE 7.6: Transverse susceptibility parameters for the proposed dual-band metafilm unit cells shown in Fig. 7.3(a) and Fig. 7.3(b).

The data shown in Fig. 7.6 also explain the polarization selectivity of the proposed designs. The χ_{ES}^{xx} susceptibility component in Fig. 7.6(a) explains the dual-band behaviour of the unit cell shown in Fig.7.3(a) for an X-polarized electric field of excitation. Similarly, the χ_{ES}^{xx} and χ_{ES}^{yy} components in Fig. 7.6(b) indicate that the lower frequency band of the metafilm design shown in Fig.7.3(b) needs to be excited through an X-polarized incident wave, while the upper band responds to a Y-polarized incident wave. The strength of the observed dipole-like susceptibility components is consistent with the contrast of the resonances in the scattering parameters of each structure.

7.4 Fabrication and Experiment

To verify the shielding response of the proposed metafilm designs, two 16×12 arrays were fabricated using an LPKF ProtoLaser U3 laser-milling machine as shown in Fig. 7.7. An inset is shown at the top-right corner of each fabricated prototype, magnifying one fabricated unit cell. The number of unit cells in the arrays was chosen to maximize the use of space on an available 9-in $\times$ 12-in substrate panel. The substrate used for fabrication is Rogers RT/Duroid 5880 with 17-µm copper cladding thickness, which matches that used in simulations. The fabricated structure measures $1.7\lambda \times 2.3\lambda$ at the upper resonance frequency, and $1.3\lambda \times 1.7\lambda$ at the lower resonance frequency.

Figure 7.8 depicts the experimental setup used for measuring both dual-band designs in an ETS-Lindgren shielded fully anechoic chamber, picturing the double-ridged horn
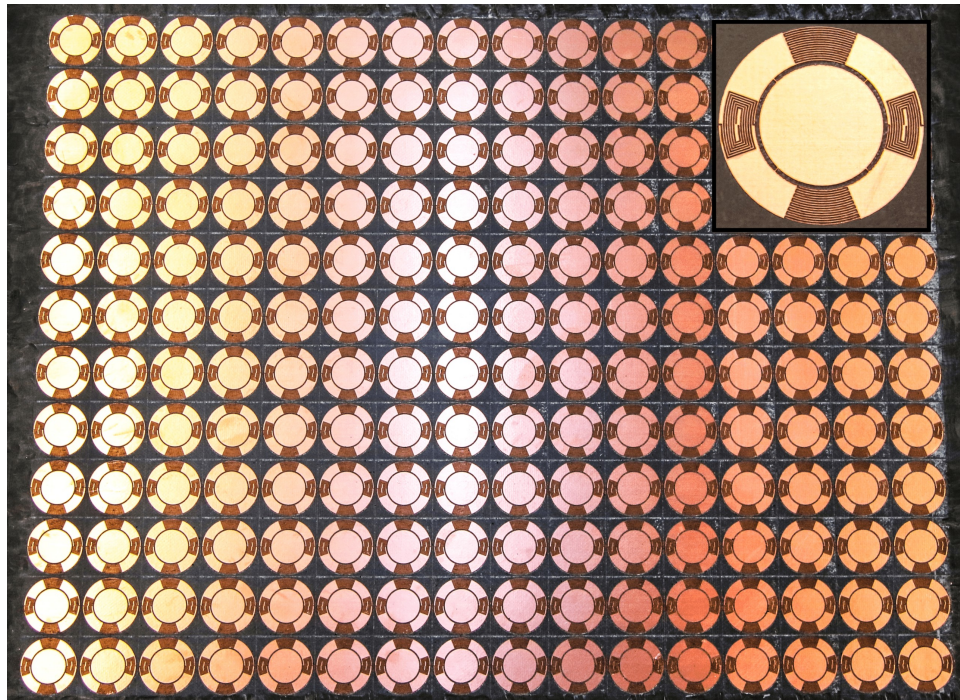
(a)
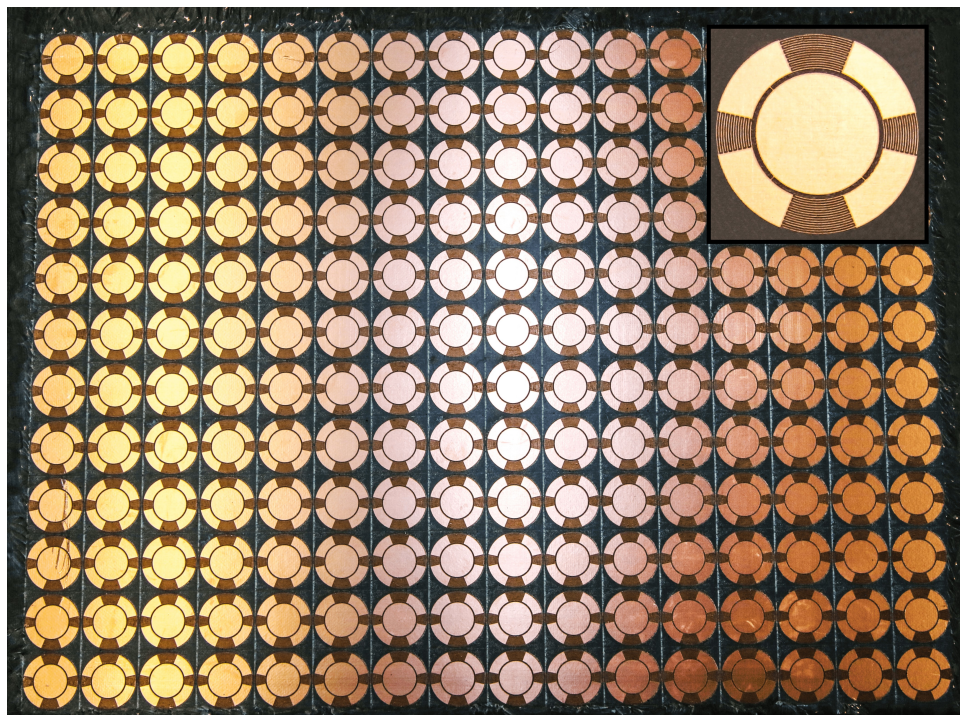
(b)

FIGURE 7.7: The fabricated 16×12 dual-band metafilm arrays possessing an overall size of $1.7\lambda \times 2.3\lambda$ at the upper resonance frequency, and $1.3\lambda \times 1.7\lambda$ at the lower resonance frequency.

(DRH) antenna probe on the left-hand side and an electrically small loop antenna on the right-hand side, placed at a distance of 166 cm (i.e., 13λ at 2.4 GHz and 10λ at 1.8 GHz) from each other. The metafilms are inserted at a distance of 104 cm from the DRH antenna (implying a distance of 62 cm from the loop antenna). These distances are chosen as close to the far-field distances of the two antennas as possible within the space afforded by the chamber, so as to realize a plane-wave-like excitation. This experimental setup has been designed for measuring the transmission parameter of the proposed metafilm arrays, as this parameter proves easier to experimentally validate. As the simulation data in Fig. 7.4 demonstrate that these metafilms are generally low-loss, it can be concluded that a reduction in S_{21} implies an increase in S_{11}.

Furthermore, a large screen covered with absorbers was built with a window of the same size as the fabricated metafilms in the center, so as to minimize the multi-path propagation effects on the measured response of the metafilms. The transmission parameter was then obtained for each design with the fabricated prototype inserted into the window, and normalized to the corresponding values measured in its absence. The measured transmission parameters are presented in Fig. 7.9 (solid curves) along with the simulated data (dashed curves) for each dual band metafilm design.

As the data in Fig. 7.9(a) represent, two shielding bands are observed in the response of the first metafilm design for an X-directed electric field of incidence (i.e., polarization 1), while no resonance effects are observed for a Y-polarized incident plane wave (i.e.,
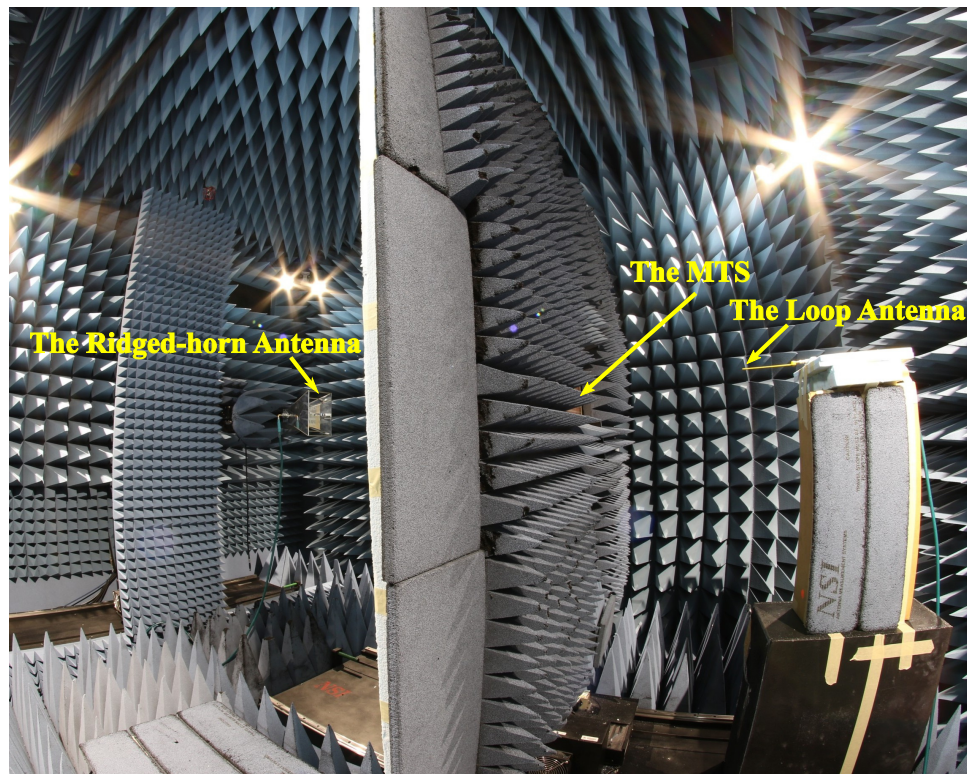
FIGURE 7.8: The measurement setup in an antenna anechoic chamber with the double-ridged horn antenna probe on the left hand side and the small loop antenna on the right-hand side, placed at a distance of 166 cm ($\sim 13\lambda$ at 2.4 GHz and 10λ at 1.8 GHz) from each other. For each measurement, the fabricated prototypes are inserted between the two antennas at a distance of 104 cm from the ridged horn.
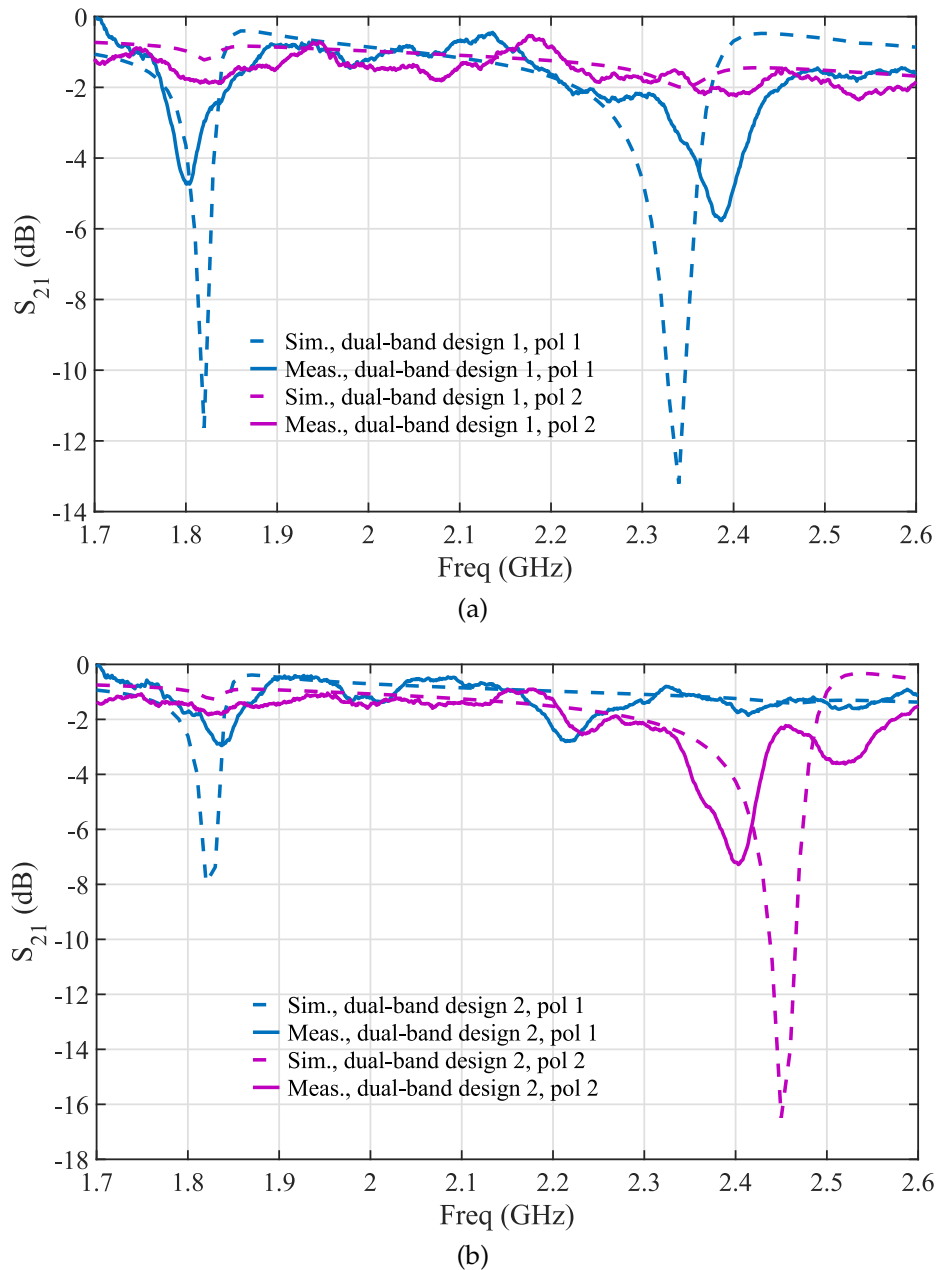
FIGURE 7.9: The normalized measured S_{21} plotted against the original simulation data (dashed curves) for (a) the dual-band metafilm design shown in Fig. 7.3(a), and (b) the dual-band metafilm design shown in Fig. 7.3(b).

polarization 2). The data shown in Fig. 7.9(b) demonstrate the lower shielding band for an X-polarized incident wave, and the upper shielding band for a Y-polarized incident wave, as was expected from simulations. Although the polarization selectivity and trend of the transmission parameters are consistent between the simulation and measurement data, minor frequency shifts ($1 - 2\%$) are observed as a result of fabrication errors specially at the upper shielding bands. It can be inferred from the measured data that trace widths that are slightly larger than the desired value of $100\,\mu$m are responsible for such shifts. In fact, wider traces can cause an upshift in the upper band of the first dual-band design, as such an error causes a reduction in the value of spiral inductors. In the second dual-band design, however, wider traces (i.e., narrower gaps) imply a larger loading capacitor, resulting in a downshift in the operating frequency. An apparent reduction in the amount of shielding is also observed in the measured data. Whereas the simulated reductions in the transmission parameter at the lower and upper shielding bands of the first metafilm design measure 11 and 12 dB, respectively, the measured values are only about $5 - 6$ dB. The transmission reductions of the second metafilm design measure 7 and 15 dB in simulation, whereas the measured values are about 3 and 7.5 dB, respectively. Part of this reduction is a result of overheating of the substrate during the laser milling process, which has shown to increase the amount of power dissipation in capacitors/inductors. Another (more important) factor responsible for this difference is the finite size of the fabricated array as compared to the infinite size modeled in simulations through periodic

boundary conditions. Therefore, the measured shielding levels can be improved through a more accurate fabrication process as well as the fabrication of larger metafilm arrays.

7.5   Applications

Both proposed metafilm unit cells may be made extremely subwavelength. This property can be exploited through the design of dual-band, polarization-selective inhomogeneous partially transmitting/reflecting surfaces for beam-shaping, as they provide extremely high-spatial-resolution control of the transmitted and reflected fields. This metafilm is also beneficial for dual-band shielding applications that require a compact array due to a limited available space, or require polarization sensitivity. Moreover, these unit cells can act as a dual-band polarizers, as one polarization passes through with small amount of insertion loss, while the opposite polarization is reflected. Therefore, an incoming circularly polarized wave will be converted to a linearly polarized one. In all these applications, there is always a trade-off between the level of shielding and the degree of miniaturization. The circular-shaped geometry of this unit cell along with its subwavelength size provides maximum adaptability for applications that require conformal MTSs [189]. Frequency insensitivity with respect to the periodicity and the angle of incidence (owed to extreme miniaturization) are also beneficial for many applications.

Chapter 8

Conclusions and Future Work

8.1   Summary

The work described in this thesis has been focused on the intriguing effects of lining circular apertures in a metallic screen with MTM liners possessing dispersive negative and near-zero permittivity. The MTM liner partially fills the aperture, allowing access to the interior of the aperture. The reduced resonance mechanism of a miniaturized circular aperture is analyzed theoretically, numerically, and experimentally. It was shown that the resonance frequency of the fundamental HE_{11} mode may be controlled using the aperture size and liner permittivity and/or thickness. The transmission through an infinite array of practical ENNZ-MTM-lined apertures excited using a plane wave was obtained through full-wave HFSS simulations, which demonstrated a Fano-shape resonance profile at frequencies where the apertures measured $\lambda/4$ or smaller. A transmission enhancement of $6 - 7$ dB over similar-sized unlined circular apertures was obtained at resonance, followed

by an antiresonance achieving $19 - 20$ dB reduction in transmission. Strong agreement was shown between analytical derivations, full-wave simulation data, and experiments. The ENNZ-MTM-lined circular apertures operating in the frequency-reduced regime offer the potential for various applications through providing high-spatial-resolution control of transmitted/reflected fields. It was shown that the degree of miniaturization can be improved by judiciously changing the design parameters of the MTM liner, and a nonuniform array of five circular apertures measuring approximately $\lambda/7$ at their corresponding resonance frequencies were used to design a near-field imaging probe for detecting conducting obstacles in a frequency-location mapping scheme. As these apertures are only partially filled using the MTM-liner loading, they are suitable for sensing of liquids and biological materials, or shielding applications that demand visual accessibility.

Furthermore, it has been shown that if the metallic and gap regions of the proposed ENNZ-MTM-lined circular aperture are interchanged, and the radially directed loading inductors in the design of ENNZ MTM liner are replaced with azimuthally directed loading capacitors, a complementary miniaturized metallic disc resonator is obtained. This metallic disc is, in fact, lined with an MNNZ MTM liner, and shows dual transmission/reflection behaviour at resonance with a similar level of miniaturization. Whereas the ENNZ-lined aperture array falls in the category of metacreens, the MNNZ-lined disc array may be called a metafilm. The MNNZ behaviour of the MTM liner at resonance was verified using two rigorous and independent studies: I. a homogenization technique based on a

transmission-line model for the MNNZ MTM liner, and II. an eigenmode study of the

first two reduced modes, EH_{11} and HE_{01} modes, under the assumption that the plasma

frequency of the liner is equal to the resonance frequency of the reduced HE_{01} mode, and

that the permeability of the liner follows a Drude dispersion profile. The MNNZ-MTM-

lined metallic discs experience a frequency reduced EH_{11} resonance with a Fano-shape

reflection profile for a normally incident plane-wave excitation, which provides $4 - 5$ dB

better shielding at resonance, and 1.2 dB better transmission at its antiresonance as com-

pared to an unlined metallic disc array. Full-wave simulations were used to verify the

effect of various design parameters and angles of incidence. A stable response was ob-

served for oblique angles of incidence up to $60°$ for both TE- and TM-polarized incident

plane waves owed to the extreme degree of miniaturization. Moreover, the relationships

between the susceptibility components of a homogenized sheet equivalent of the pro-

posed metafilm unit cell and its transmission/reflection parameters were derived assum-

ing a bianisotropic susceptibility tensor, X-Y symmetry, highly decoupled TE/TM modes,

and a vacuum response in the Z direction. The extracted parameters showed an electric-

dipole-like behaviour at resonance, and were validated through full wave simulations.

Lastly, the shielding response of the proposed metafilm was verified experimentally, and

a list of applications that can benefit from this technology was presented.

Complementing these studies, it was shown that the proposed metafilm unit cells can

be made polarization-sensitive by utilizing an MNNZ MTM liner that was loaded asymmetrically in X and Y directions. Moreover, it was exhibited that a similar shielding response can be obtained using a different technology based on MPL-lined metallic discs. Similarly, a polarization-sensitive version of this unit cell was introduced and investigated. It was shown that, interestingly, the two unit cells respond to different polarizations of excitation. This property was exploited for the design of a dual-band unit cell by combining the two technologies. Another dual-band unit cell was also introduced only based on the MNNZ-MTM-lined unit cell, but by using different loading capacitor values on the X and Y axes of the unit cell. The two dual-band metafilm designs were studied numerically and experimentally. Dual-band shielding at representative frequencies of 1.8 GHz and 2.4 GHz was verified, and it was demonstrated that the two operating bands can be tuned independently through extracting the susceptibility tensors of the corresponding single-band unit cells and comparing with those of the dual-band designs.

8.2 Contributions

This section lists academic contributions made during the course of this work, including refereed journal and conference papers, patents and reports of inventions.

8.2.1 Journal Papers

[JP5] Elham Baladi, Mitchell Semple, and Ashwin K. Iyer, "Single-Layer Dual-Band Polarization-Selective Metafilm with Independently Controlled and Closely Spaced Bands", Prepared for submission to *IEEE Trans. Antennas Propagation*.

[JP4] Elham Baladi, Mitchell Semple, and Ashwin K. Iyer, "A Filtering Metasurface Based on Highly Miniaturized MNNZ-Loaded Discs", under review in *IEEE Trans. Antennas Propagation*.

[JP3] Mitchell Semple, Elham Baladi, and Ashwin K. Iyer, "Optical Metasurface Based on Subwavelength Nanoplasmonic Metamaterial-Lined Apertures", under review in the *Special Issue on Metamaterial Photonics and Integration* in *IEEE Journal of Selected Topics in Quantum Electronics*.

[JP2] Elham Baladi and Ashwin K. Iyer, "Far-Field Magnification of Subdiffraction Conducting Features Using Metamaterial-Lined Aperture Arrays", *IEEE Trans. Antennas Propagation*, Vol. 66, No. 7, pp. 3482-3490, July 2018.

[JP1] Elham Baladi, Justin G. Pollock, and Ashwin K. Iyer, "New approach for extraordinary transmission through an array of subwavelength apertures using thin ENNZ metamaterial liners", *Opt. Express*, Vol. 23, No. 16, pp. 20356-20365, July 2015.

8.2.2 Conference Papers

[CP9] E. Baladi and A. K. Iyer, "A Metafilm Based on Magnetic-Metamaterial-Lined Discs", submitted to the *2019 IEEE International Symposium on Antennas and Propagation and North American Radio Science Meeting*, Atlanta, Georgia, USA, July 7-12, 2019.

[CP8] **Invited**: E. Baladi, M. Semple, and A. K. Iyer, "Imaging of Subwavelength Features in the Far-Field Using Resonant Metasurfaces: Design from Microwave to Infrared Frequencies," submitted to the Special Session: Forward Scattering and Propagation at the *URSI-EMTS 2019 International Symposium on Electromagnetic Theory*, San Diego, California, USA, May 27-31, 2019.

[CP7] **Invited**: M. Semple, E. Baladi, and A. K. Iyer, "Advances in metasurfaces based on metamaterial-lined apertures and discs," accepted in the Special Session: Metamaterials and Metasurfaces: Theory and Applications at the *USNC-URSI National Radio Science Meeting*, (Boulder, CO, USA), January 9-12, 2019.

[CP6] E. Baladi, M. Semple, and A. K. Iyer, "High-Resolution Optical Imaging Using ENNZ-Metamaterial-Lined Aperture Arrays", *MRS Fall Meeting and Exhibit*, Boston, Massachusetts, Nov. 26th- Dec. 1st, 2017.

[CP5] M. Semple, E. Baladi, J. Pollock, and A. K. Iyer, "Optical Implementation of a Miniaturized ENNZ-Metamaterial-Lined Aperture Array", *IEEE International Symposium on Antennas and Propagation and North American Radio Science Meeting*, San Diego, California, USA, July 9-14, 2017.

[CP4] E. Baladi and A. K. Iyer, "Subwavelength Metamaterial-Lined Apertures as Far-Field Imaging Devices", *IEEE International Symposium on Antennas and Propagation and North American Radio Science Meeting*, San Diego, California, USA, July 9-14, 2017. Selected as an Honorable Mention at the 2017 IEEE AP-S Symposium Student Paper Competition.

[CP3] E. Baladi and A. K. Iyer, "Far-field High-resolution Imaging of Conducting Obstacles using Metamaterial-lined Aperture Arrays", *IEEE International Symposium on Antennas and Propagation and North American Radio Science Meeting*, Puerto Rico, US, June 26th- July 1st 2016. Selected as an Honorable Mention at the 2016 IEEE AP-S Symposium Student Paper Competition.

[CP2] E. Baladi, J. G. Pollock, and A. K. Iyer, "Enhanced Transmission through Metamaterial-Lined Subwavelength Apertures", *IEEE International Symposium on Antennas and Propagation and North American Radio Science Meeting*, Vancouver, Canada, 19-25 July 2015.

[CP1] E. Baladi, J. G. Pollock, and A. K. Iyer, "A New Approach for Extraordinary Transmission through Subwavelength Apertures Using ENNZ Metamaterials", *META15 conference*, New York, 4-7 August 2015.

8.2.3   Patents and Reports of Invention

[P2] A. K. Iyer, E. Baladi, and J. G. Pollock, "Devices and methods using discs with magnetic metamaterial peripheries (metafilm structures)," US Provisional Patent Application 62/738,988, filed September 28, 2018.

[P1] A. K. Iyer, E. Baladi, and J. G. Pollock, "Metamaterial-based aperture arrays enabling engineered transmission and shielding properties," submitted to TEC Edmonton on June 22, 2015.

8.3   Future Directions

The results presented in this thesis have analytically, numerically and experimentally demonstrated that the introduction of thin ENNZ/MNNZ MTM liners into the interior/exterior of circular apertures/metallic discs allows their strong miniaturization by means of reducing the resonance frequency of the fundamental mode. These structures show improved transmission/reflection properties over similarly sized unlined designs, at frequencies that are controlled by the design of the MTM liners. GSTCs were also used to introduce a set of susceptibility parameters for modeling the MNNZ-lined discs as homogeneous sheets/thin slabs. Dual-band, single-layer metafilm designs were also developed, and studied numerically and experimentally. Possible future directions for this research include:

8.3.1   Investigation of Homogeneous Sheet Models for the Proposed Metascreen Designs

The GSTC conditions for a metascreen were recently published in [160]. These conditions may be used to obtain susceptibility tensors for an equivalent, homogenized sheet model for the ENNZ-lined apertures introduced in this work. The extracted susceptibilities not only provide insight into the mechanism of the resonance, but are also useful for faster numerical studies of inhomogeneous metascreens.

8.3.2   Application of Proposed Metafilm Unit Cells for Beam-shaping

The proposed metafilm unit cells may be applied to the design of beam-shaping radomes, in the form of a transmit-array. For such applications, the metafilm unit cells may be used above their resonance frequency, where they transmit strongly. Studies show that a phase range of about $\sim 45°$ can obtained above the resonance frequency of the proposed metafilm unit cells for a single-layer structure. In such applications, the extremely subwavelength size of the unit cells is beneficial in terms of providing high-spatial-resolution control over transmitted fields. To obtain a $360°$ phase range, stacked layers with an optimum spacing of $\lambda/4$ may be used [140, 204, 205]. Furthermore, the phase range of the single-layer structure may be improved through the simultaneous excitation of a magnetic-dipole-like resonance at the same frequency as the electric-dipole-like resonance [206, 207]. Initial studies show that this is possible for oblique angles of incidence,

and may be controlled through adjusting the spacing between the MTM liner and inner disc regions, or the overall size of the resonator.

8.3.3 Dielectric Sensing

The proposed metafilm/metascreen technology may be explored for characterization of dielectric and/or biological substances. The resonance frequency of both MTS designs is sensitive to the permittivity of the underlying dielectric substrate, a dielectric cover. Additionally, the resonance frequency of the metascreen design is sensitive to the presence of a dielectric material inside the empty region of the aperture, or a liquid passing through this region (as the MTM liner only partially fills the aperture). Shifts in the resonance frequency of homogeneous arrays may be used for material characterization. Inhomogeneous MTSs may also be developed for characterizing inhomogeneous dielectric substrates, in a similar manner to the frequency-multiplexed imaging scheme explained in chapter 5.

8.3.4 Mode Matching Analysis for ENNZ-lined Apertures

The analytical studies based on the analogy with circular waveguides in this work explain the reduced-frequency resonance mechanism, and the calculated fields may be used to explain the enhanced radiation behaviour in the far-field through the application of antenna

array theory. However, this analysis does not explain the Fano-shape profile of transmission, as it does not account for additional, weakly excited modes that are present in the near-field of the apertures, and couple to the fundamental radiating mode. Therefore, a rigorous mode-matching analysis is required so as to explain the Fano-shape profile of resonance of the metascreen design. This study may also be done for the metafilm unit cell, as analytical waveguide-like studies cannot fully model the electric/magnetic fields of the inner disc region at resonance.

8.3.5 Optical Devices

All aspects and applications of the proposed technologies may also be extended to optical frequencies. In fact, this has been actively investigated by my colleague, Mitchell Semple. Studies show that the same reduced-resonance Fano-shape response may be obtained for ENNZ-lined apertures at optical frequencies. Although electrical size of MTS unit cells is not a concern at optical frequencies, the miniaturization is still useful in terms of increasing the resolution of control over the transmitted/reflected fields. The Fano lineshape of the resonance may also be applied to the design of optical switches through the introduction of non-linear materials.

Bibliography

[1] Christopher L Holloway, Edward F Kuester, Joshua A Gordon, John O'Hara, Jim Booth, and David R Smith. "An overview of the theory and applications of metasurfaces: The two-dimensional equivalents of metamaterials". In: *IEEE Antennas and Propagation Magazine* 54.2 (2012), pp. 10–35.

[2] Justin G Pollock and Ashwin K Iyer. "Below-cutoff propagation in metamaterial-lined circular waveguides". In: *IEEE Transactions on Microwave Theory and Techniques* 61.9 (2013), pp. 3169–3178.

[3] Thomas W Ebbesen, H Jêőň Lezec, HF Ghaemi, Tineke Thio, and PA Wolff. "Extraordinary optical transmission through sub-wavelength hole arrays". In: *Nature* 391.6668 (1998), p. 667.

[4] Tineke Thio, HF Ghaemi, HJ Lezec, PA Wolff, and TW Ebbesen. "Surface-plasmon-enhanced transmission through hole arrays in Cr films". In: *JOSA B* 16.10 (1999), pp. 1743–1748.

[5] Henri J Lezec, A Degiron, E Devaux, RA Linke, L Martin-Moreno, FJ Garcia-Vidal, et al. "Beaming light from a subwavelength aperture". In: *Science* 297.5582 (2002), pp. 820–822.

[6] Luis Martin-Moreno, FJ Garcia-Vidal, HJ Lezec, KM Pellerin, Tineke Thio, JB Pendry, et al. "Theory of extraordinary optical transmission through subwavelength hole arrays". In: *Physical review letters* 86.6 (2001), p. 1114.

[7] DR Jackson, J Chen, R Qiang, F Capolino, and AA Oliner. "The role of leaky plasmon waves in the directive beaming of light through a subwavelength aperture". In: *Optics Express* 16.26 (2008), pp. 21271–21281.

[8] Francisco Medina, Francisco Mesa, and Ricardo Marques. "Extraordinary transmission through arrays of electrically small holes from a circuit theory perspective". In: *IEEE Transactions on Microwave Theory and Techniques* 56.12 (2008), pp. 3108–3120.

[9] Vitaliy Lomakin and Eric Michielssen. "Enhanced transmission through metallic plates perforated by arrays of subwavelength holes and sandwiched between dielectric slabs". In: *Physical Review B* 71.23 (2005), p. 235117.

[10] R Marqués, L Jelinek, F Mesa, and F Medina. "Analytical theory of wave propagation through stacked fishnet metamaterials". In: *Optics express* 17.14 (2009), pp. 11582–11593.

[11] Reuven Gordon, Alexandre G Brolo, David Sinton, and Karen L Kavanagh. "Resonant optical transmission through hole-arrays in metal films: physics and applications". In: *Laser & Photonics Reviews* 4.2 (2010), pp. 311–335.

[12] S Carretero-Palacios, FJ García-Vidal, Luis Martín-Moreno, and Sergio G Rodrigo. "Effect of film thickness and dielectric environment on optical transmission through subwavelength holes". In: *Physical Review B* 85.3 (2012), p. 035417.

[13] KJ Klein Koerkamp, Stefan Enoch, Franciscus B Segerink, NF Van Hulst, and L Kuipers. "Strong influence of hole shape on extraordinary transmission through periodic arrays of subwavelength holes". In: *Physical review letters* 92.18 (2004), p. 183901.

[14] HE Went, Alastair P Hibbins, J Roy Sambles, Christopher R Lawrence, and AP Crick. "Selective transmission through very deep zero-order metallic gratings at microwave frequencies". In: *Applied Physics Letters* 77.18 (2000), pp. 2789–2791.

[15]   Ilaria Gallina, Giuseppe Castaldi, Vincenzo Galdi, Emiliano Di Gennaro, and Antonello Andreone. "Paired cut-wire arrays for enhanced transmission of transverse-electric fields through subwavelength slits in a thin metallic screen". In: *IEEE Antennas and Wireless Propagation Letters* 9 (2010), pp. 641–644.

[16]   M Beruete, M Sorolla, I Campillo, JS Dolado, L Martín-Moreno, J Bravo-Abad, et al. "Enhanced millimeter-wave transmission through subwavelength hole arrays". In: *Optics Letters* 29.21 (2004), pp. 2500–2502.

[17]   M Beruete, M Navarro-Cía, V Torres, and M Sorolla. "Redshifting extraordinary transmission by simple inductance addition". In: *Physical Review B* 84.7 (2011), p. 075140.

[18]   M. Born and E. Wolf. *The Diffraction Theory of Aberrations, 7th Ed.* Cambridge University Press, 1999, pp. 465–471.

[19]   Hans Albrecht Bethe. "Theory of diffraction by small holes". In: *Physical review* 66.7-8 (1944), p. 163.

[20]   Reuven Gordon. "Bethe's aperture theory for arrays". In: *Physical Review A* 76.5 (2007), p. 053806.

[21]   Robert Williams Wood. "XLII. On a remarkable case of uneven distribution of light in a diffraction grating spectrum". In: *The London, Edinburgh, and Dublin Philosophical Magazine and Journal of Science* 4.21 (1902), pp. 396–402.

[22]   L Rayleigh. "Note on the remarkable case of diffraction spectra described by Prof. Wood". In: *Philos. Mag.* 14 (1907), pp. 60–65.

[23]   Víctor Torres, Rubén Ortuno, Pablo Rodríguez-Ulibarri, Amadeu Griol, Alejandro Martínez, Miguel Navarro-Cia, et al. "Mid-infrared plasmonic inductors: Enhancing inductance with meandering lines". In: *Scientific reports* 4 (2014), p. 3592.

[24] JB Pendry, L Martin-Moreno, and FJ Garcia-Vidal. "Mimicking surface plasmons with structured surfaces". In: *Science* 305.5685 (2004), pp. 847–848.

[25] SM Orbons and A Roberts. "Resonance and extraordinary transmission in annular aperture arrays". In: *Optics express* 14.26 (2006), pp. 12623–12628.

[26] Andrea Alù, Filiberto Bilotti, Nader Engheta, and Lucio Vegni. "Metamaterial covers over a small aperture". In: *IEEE Transactions on Antennas and propagation* 54.6 (2006), pp. 1632–1643.

[27] Miguel Navarro-Cía, Pablo Rodriguez-Ulibarri, and M Beruete. "Hedgehog subwavelength hole arrays: control over the THz enhanced transmission". In: *New Journal of Physics* 15.1 (2013), p. 013003.

[28] Mário G Silveirinha and Nader Engheta. "Sampling and squeezing electromagnetic waves through subwavelength ultranarrow regions or openings". In: *Physical Review B* 85.8 (2012), p. 085116.

[29] Filiberto Bilotti, Luca Scorrano, Ekmel Ozbay, and Lucio Vegni. "Enhanced transmission through a sub-wavelength aperture: resonant approaches employing metamaterials". In: *Journal of Optics A: Pure and Applied Optics* 11.11 (2009), p. 114029.

[30] Ben A Munk. *Frequency selective surfaces: theory and design*. John Wiley & Sons, 2005.

[31] Ravi Panwar and Jung Ryul Lee. "Progress in frequency selective surface-based smart electromagnetic structures: A critical review". In: *Aerospace Science and Technology* 66 (2017), pp. 216–234.

[32] Raj Mittra, Chi H Chan, and Tom Cwik. "Techniques for analyzing frequency selective surfaces-a review". In: *Proceedings of the IEEE* 76.12 (1988), pp. 1593–1615.

[33] Mudar Al-Joumayly and Nader Behdad. "A new technique for design of low-profile, second-order, bandpass frequency selective surfaces". In: *IEEE Transactions on Antennas and Propagation* 57.2 (2009), pp. 452–459.

[34] Yunlong Shang, S Xiao, M-C Tang, Y-Y Bai, and B Wang. "Radar cross-section reduction for a microstrip patch antenna using PIN diodes". In: *IET microwaves, antennas & propagation* 6.6 (2012), pp. 670–679.

[35] Te-Kao Wu. *Frequency selective surface and grid array*. Vol. 40. Wiley-Interscience, 1995.

[36] Jordi Romeu and Yahya Rahmat-Samii. "Fractal FSS: A novel dual-band frequency selective surface". In: *IEEE Transactions on antennas and propagation* 48.7 (2000), pp. 1097–1105.

[37] Ghaffer I Kiani, Kenneth L Ford, Karu P Esselle, Andrew R Weily, C Panagamuwa, and John C Batchelor. "Single-layer bandpass active frequency selective surface". In: *Microwave and optical technology letters* 50.8 (2008), pp. 2149–2151.

[38] Antonio Luiz PS Campos, Elder Eldervitch C de Oliveira, and Paulo Henrique da Fonseca Silva. "Design of miniaturized frequency selective surfaces using Minkowski island fractal". In: *Journal of Microwaves, Optoelectronics and Electromagnetic Applications (JMOe)* 9.1 (2010), pp. 43–49.

[39] Bo Li and Zhongxiang Shen. "Bandpass frequency selective structure with wideband spurious rejection". In: *IEEE Antennas and Wireless Propagation Letters* 13 (2014), pp. 145–148.

[40] Ke Li, Long Li, Yuan-Ming Cai, Cheng Zhu, and Chang-Hong Liang. "A novel design of low-profile dual-band circularly polarized antenna with meta-surface". In: *IEEE Antennas and Wireless Propagation Letters* 14 (2015), pp. 1650–1653.

[41] Seyed Mohamad Amin Momeni Hasan Abadi, Meng Li, and Nader Behdad. "Harmonic-suppressed miniaturized-element frequency selective surfaces with higher order bandpass responses". In: *IEEE Transactions on Antennas and Propagation* 62.5 (2014), pp. 2562–2571.

[42] Seyed Mohamad Amin Momeni Hasan Abadi and Nader Behdad. "Design of wide-band, FSS-based multibeam antennas using the effective medium approach". In: *IEEE Transactions on Antennas and Propagation* 62.11 (2014), pp. 5557–5564.

[43] Ahmed H Abdelrahman, Atef Z Elsherbeni, and Fan Yang. "Transmission phase limit of multilayer frequency-selective surfaces for transmitarray designs". In: *IEEE Transactions on Antennas and Propagation* 62.2 (2014), pp. 690–697.

[44] Ahmed H Abdelrahman, Atef Z Elsherbeni, and Fan Yang. "Transmitarray antenna design using cross-slot elements with no dielectric substrate". In: *IEEE Antennas and Wireless Propagation Letters* 13 (2014), pp. 177–180.

[45] Lourdes Martinez-Lopez, Jorge Rodriguez-Cuevas, Jose I Martinez-Lopez, and Alexander E Martynyuk. "A multilayer circular polarizer based on bisected split-ring frequency selective surfaces". In: *IEEE Antennas Wireless Propag. Lett* 13 (2014), pp. 153–156.

[46] Benedikt Munk, R Kouyoumjian, and Leon Peters. "Reflection properties of periodic surfaces of loaded dipoles". In: *IEEE Transactions on Antennas and Propagation* 19.5 (1971), pp. 612–617.

[47] Nader Behdad. "A second-order band-pass frequency selective surface using non-resonant subwavelength periodic structures". In: *Microwave and Optical Technology Letters* 50.6 (2008), pp. 1639–1643.

[48] David R Smith, John B Pendry, and Mike CK Wiltshire. "Metamaterials and negative refractive index". In: *Science* 305.5685 (2004), pp. 788–792.

[49] Ashwin K Iyer and George V Eleftheriades. "Mechanisms of subdiffraction free-space imaging using a transmission-line metamaterial superlens: An experimental verification". In: *Applied Physics Letters* 92.13 (2008), p. 131105.

[50] Ashwin K Iyer and George V Eleftheriades. "Free-space imaging beyond the diffraction limit using a Veselago-Pendry transmission-line metamaterial superlens". In: *IEEE transactions on antennas and propagation* 57.6 (2009), pp. 1720–1727.

[51] Koray Aydin, Irfan Bulu, and Ekmel Ozbay. "Subwavelength resolution with a negative-index metamaterial superlens". In: *Applied physics letters* 90.25 (2007), p. 254102.

[52] Nicholas Fang and Xiang Zhang. "Imaging properties of a metamaterial superlens". In: *Nanotechnology, 2002. IEEE-NANO 2002. Proceedings of the 2002 2nd IEEE Conference on*. IEEE. 2002, pp. 225–228.

[53] Andrea Alu and Nader Engheta. "Multifrequency optical invisibility cloak with layered plasmonic shells". In: *Physical review letters* 100.11 (2008), p. 113901.

[54] David Schurig, JJ Mock, BJ Justice, Steven A Cummer, John B Pendry, AF Starr, et al. "Metamaterial electromagnetic cloak at microwave frequencies". In: *Science* 314.5801 (2006), pp. 977–980.

[55] Andrea Alù and Nader Engheta. "Pairing an epsilon-negative slab with a mu-negative slab: resonance, tunneling and transparency". In: *IEEE Transactions on Antennas and Propagation* 51.10 (2003), pp. 2558–2571.

[56] Filiberto Bilotti, Andrea Alu, and Lucio Vegni. "Design of Miniaturized Metamaterial Patch Antennas With mu-Negative Loading". In: *IEEE Transactions on Antennas and Propagation* 56.6 (2008), pp. 1640–1647.

[57] Andrea Alù, Filiberto Bilotti, Nader Engheta, and Lucio Vegni. "Subwavelength, compact, resonant patch antennas loaded with metamaterials". In: *IEEE Transactions on Antennas and Propagation* 55.1 (2007), pp. 13–25.

[58] Jiang Zhu and George V Eleftheriades. "A compact transmission-line metamaterial antenna with extended bandwidth". In: *IEEE antennas and wireless propagation letters* 8 (2009), pp. 295–298.

[59] Le-Wei Li, Ya-Nan Li, Tat Soon Yeo, Juan R Mosig, and Olivier JF Martin. "A broadband and high-gain metamaterial microstrip antenna". In: *Applied Physics Letters* 96.16 (2010), p. 164101.

[60] Ajay Gummalla, Marin Stoytchev, Maha Achour, and Gregory Poilasne. *Metamaterial antenna arrays with radiation pattern shaping and beam switching*. US Patent 8,462,063. 2013.

[61] Carl Pfeiffer and Anthony Grbic. "Metamaterial Huygens' surfaces: tailoring wave fronts with reflectionless sheets". In: *Physical review letters* 110.19 (2013), p. 197401.

[62] Dongmin Wu, Nicholas Fang, Cheng Sun, Xiang Zhang, Willie J Padilla, Dimitri N Basov, et al. "Terahertz plasmonic high pass filter". In: *Applied Physics Letters* 83.1 (2003), pp. 201–203.

[63] Ta-Jen Yen, WJ Padilla, Nicholas Fang, DC Vier, DR Smith, JB Pendry, et al. "Terahertz magnetic response from artificial materials". In: *Science* 303.5663 (2004), pp. 1494–1496.

[64] J Zhou, Th Koschny, M Kafesaki, EN Economou, JB Pendry, and CM Soukoulis. "Saturation of the magnetic response of split-ring resonators at optical frequencies". In: *Physical review letters* 95.22 (2005), p. 223902.

[65] Na Liu, Hongcang Guo, Liwei Fu, Stefan Kaiser, Heinz Schweizer, and Harald Giessen. "Three-dimensional photonic metamaterials at optical frequencies". In: *Nature materials* 7.1 (2008), p. 31.

[66] George V Eleftheriades, Omar Siddiqui, and Ashwin K Iyer. "Transmission line models for negative refractive index media and associated implementations without excess resonators". In: *IEEE Microwave and Wireless Components Letters* 13.2 (2003), pp. 51–53.

[67] Ashwin K Iyer and George V Eleftheriades. "Negative refractive index metamaterials supporting 2-D waves". In: *Microwave Symposium Digest, 2002 IEEE MTT-S International*. Vol. 2. IEEE. 2002, pp. 1067–1070.

[68] Ashwin K Iyer, Peter C Kremer, and George V Eleftheriades. "Experimental and theoretical verification of focusing in a large, periodically loaded transmission line negative refractive index metamaterial". In: *Optics Express* 11.7 (2003), pp. 696–708.

[69] Christopher L Holloway, Edward F Kuester, James Baker-Jarvis, and Pavel Kabos. "A double negative (DNG) composite medium composed of magnetodielectric spherical particles embedded in a matrix". In: *IEEE Transactions on Antennas and Propagation* 51.10 (2003), pp. 2596–2603.

[70] John B Pendry, Anthony J Holden, David J Robbins, and WJ Stewart. "Magnetism from conductors and enhanced nonlinear phenomena". In: *IEEE transactions on microwave theory and techniques* 47.11 (1999), pp. 2075–2084.

[71] Dilong Liu, Cuncheng Li, Fei Zhou, Tao Zhang, Honghua Zhang, Xinyang Li, et al. "Rapid synthesis of monodisperse Au nanospheres through a laser irradiation-induced shape conversion, self-assembly and their electromagnetic coupling SERS enhancement". In: *Scientific reports* 5 (2015), p. 7686.

[72] George V Eleftheriades and Keith G Balmain. *Negative-refraction metamaterials: fundamental principles and applications*. John Wiley & Sons, 2005.

[73] John B Pendry, AJ Holden, WJ Stewart, and I Youngs. "Extremely low frequency plasmons in metallic mesostructures". In: *Physical review letters* 76.25 (1996), p. 4773.

[74] A Vallecchi, F Capolino, and AG Schuchinsky. "2-D isotropic effective negative refractive index metamaterial in planar technology". In: *IEEE microwave and wireless components letters* 19.5 (2009), pp. 269–271.

[75] Richard A Shelby, David R Smith, and Seldon Schultz. "Experimental verification of a negative index of refraction". In: *science* 292.5514 (2001), pp. 77–79.

[76] David R Smith and John B Pendry. "Homogenization of metamaterials by field averaging". In: *JOSA B* 23.3 (2006), pp. 391–403.

[77] David R Smith, DC Vier, N Kroll, and S Schultz. "Direct calculation of permeability and permittivity for a left-handed metamaterial". In: *Applied Physics Letters* 77.14 (2000), pp. 2246–2248.

[78] J-M Lerat, Nicolas Malléjac, and Olivier Acher. "Determination of the effective parameters of a metamaterial by field summation method". In: *Journal of applied physics* 100.8 (2006), p. 084908.

[79] Anders Pors, Igor Tsukerman, and Sergey I Bozhevolnyi. "Effective constitutive parameters of plasmonic metamaterials: homogenization by dual field interpolation". In: *Physical Review E* 84.1 (2011), p. 016609.

[80] Igor Tsukerman. "Nonlocal homogenization of metamaterials by dual interpolation of fields". In: *JOSA B* 28.12 (2011), pp. 2956–2965.

[81] S O'brien and JB Pendry. "Magnetic activity at infrared frequencies in structured metallic photonic crystals". In: *Journal of Physics: Condensed Matter* 14.25 (2002), p. 6383.

[82] Peter Markoš and Costas M Soukoulis. "Transmission properties and effective electromagnetic parameters of double negative metamaterials". In: *Optics express* 11.7 (2003), pp. 649–661.

[83] Xudong Chen, Tomasz M Grzegorczyk, Bae-Ian Wu, Joe Pacheco Jr, and Jin Au Kong. "Robust method to retrieve the constitutive effective parameters of metamaterials". In: *Physical review E* 70.1 (2004), p. 016608.

[84] DR Smith, DC Vier, Th Koschny, and CM Soukoulis. "Electromagnetic parameter retrieval from inhomogeneous metamaterials". In: *Physical review E* 71.3 (2005), p. 036617.

[85] Robert A Shore and Arthur D Yaghjian. "Traveling waves on two-and three-dimensional periodic arrays of lossless acoustic monopoles, electric dipoles, and magnetodielectric spheres". In: (2006).

[86] S Arslanagić, Troels Vejle Hansen, N Asger Mortensen, Anders Heidemann Gregersen, Ole Sigmund, Richard W Ziolkowski, et al. "A review of the scattering-parameter extraction method with clarification of ambiguity issues in relation to metamaterial homogenization". In: *IEEE Antennas and Propagation Magazine* 55.2 (2013), pp. 91–106.

[87] John Brian Pendry. "Negative refraction makes a perfect lens". In: *Physical review letters* 85.18 (2000), p. 3966.

[88] G Lubkowski, R Schuhmann, and T Weiland. "Extraction of effective metamaterial parameters by parameter fitting of dispersive models". In: *Microwave and Optical Technology Letters* 49.2 (2007), pp. 285–288.

[89] Xudong Chen, Bae-Ian Wu, Jin Au Kong, and Tomasz M Grzegorczyk. "Retrieval of the effective constitutive parameters of bianisotropic metamaterials". In: *Physical Review E* 71.4 (2005), p. 046610.

[90] T Weiland, R Schuhmann, RB Greegor, CG Parazzoli, AM Vetter, DR Smith, et al. "Ab initio numerical simulation of left-handed metamaterials: Comparison of calculations and experiments". In: *Journal of Applied Physics* 90.10 (2001), pp. 5419–5424.

[91] Bae-Ian Wu, Weijen Wang, Joe Pacheco, Xudong Chen, Tomasz M Grzegorczyk, and Jin Au Kong. "A study of using metamaterials as antenna substrate to enhance gain". In: *Progress In Electromagnetics Research* 51 (2005), pp. 295–328.

[92] Nader Engheta and Richard W Ziolkowski. "A positive future for double-negative metamaterials". In: *IEEE Transactions on Microwave Theory and Techniques* 53.4 (2005), pp. 1535–1556.

[93] Richard W Ziolkowski. "Pulsed and CW Gaussian beam interactions with double negative metamaterial slabs". In: *Optics Express* 11.7 (2003), pp. 662–681.

[94] Richard W Ziolkowski. "Gaussian Beam Interactions with Double-Negative (DNG) Metamaterials". In: *Negative-Refraction Metamaterials: Fundamental Principles and Applications* (2005), pp. 171–211.

[95] David R Smith, Willie J Padilla, DC Vier, Syrus C Nemat-Nasser, and Seldon Schultz. "Composite medium with simultaneously negative permeability and permittivity". In: *Physical review letters* 84.18 (2000), p. 4184.

[96] MMI Saadoun and N Engheta. "Theoretical study of electromagnetic properties of non-local omega media". In: *Chapter* 15 (1994), pp. 351–397.

[97] PF Loschialpo, DL Smith, DW Forester, FJ Rachford, and J Schelleng. "Electromagnetic waves focused by a negative-index planar lens". In: *Physical Review E* 67.2 (2003), p. 025602.

[98] MK Kärkkäinen. "Numerical study of wave propagation in uniaxially anisotropic Lorentzian backward-wave slabs". In: *Physical Review E* 68.2 (2003), p. 026602.

[99] Andrea Alù and Nader Engheta. "Polarizabilities and effective parameters for collections of spherical nanoparticles formed by pairs of concentric double-negative, single-negative, and/ or double-positive metamaterial layers". In: *Journal of Applied Physics* 97.9 (2005), p. 094310.

[100] SA Tretyakov and SI Maslovski. "Thin absorbing structure for all incidence angles based on the use of a high-impedance surface". In: *Microwave and Optical Technology Letters* 38.3 (2003), pp. 175–178.

[101] Andrea Alù, Alessandro Salandrino, and Nader Engheta. "Negative effective permeability and left-handed materials at optical frequencies". In: *Optics express* 14.4 (2006), pp. 1557–1567.

[102] Joshua A Gordon and Richard W Ziolkowski. "The design and simulated performance of a coated nano-particle laser". In: *Optics Express* 15.5 (2007), pp. 2622–2653.

[103] Nanfang Yu and Federico Capasso. "Flat optics with designer metasurfaces". In: *Nature materials* 13.2 (2014), p. 139.

[104] Stefano Maci, Gabriele Minatti, Massimiliano Casaletti, and Marko Bosiljevac. "Metasurfing: Addressing waves on impenetrable metasurfaces". In: *IEEE Antennas and Wireless Propagation Letters* 10 (2011), pp. 1499–1502.

[105] F Falcone, T Lopetegi, MAG Laso, JD Baena, J Bonache, M Beruete, et al. "Babinet principle applied to the design of metasurfaces and metamaterials". In: *Physical review letters* 93.19 (2004), p. 197401.

[106] Alexander V Kildishev, Alexandra Boltasseva, and Vladimir M Shalaev. "Planar photonics with metasurfaces". In: *Science* 339.6125 (2013), p. 1232009.

[107] Francesco Aieta, Patrice Genevet, Mikhail A Kats, Nanfang Yu, Romain Blanchard, Zeno Gaburro, et al. "Aberration-free ultrathin flat lenses and axicons at telecom wavelengths based on plasmonic metasurfaces". In: *Nano letters* 12.9 (2012), pp. 4932–4936.

[108] Amir Arbabi, Yu Horie, Mahmood Bagheri, and Andrei Faraon. "Dielectric metasurfaces for complete control of phase and polarization with subwavelength spatial resolution and high transmission". In: *Nature nanotechnology* 10.11 (2015), p. 937.

[109] Lingling Huang, Xianzhong Chen, Holger MuÌĹhlenbernd, Guixin Li, Benfeng Bai, Qiaofeng Tan, et al. "Dispersionless phase discontinuities for controlling light propagation". In: *Nano letters* 12.11 (2012), pp. 5750–5755.

[110] Xin Li, Shiyi Xiao, Bengeng Cai, Qiong He, Tie Jun Cui, and Lei Zhou. "Flat metasurfaces to focus electromagnetic waves in reflection geometry". In: *Optics letters* 37.23 (2012), pp. 4940–4942.

[111] Xingjie Ni, Satoshi Ishii, Alexander V Kildishev, and Vladimir M Shalaev. "Ultrathin, planar, Babinet-inverted plasmonic metalenses". In: *Light: Science & Applications* 2.4 (2013), e72.

[112] Xiao-Yan Jiang, Jia-Sheng Ye, Jing-Wen He, Xin-Ke Wang, Dan Hu, Sheng-Fei Feng, et al. "An ultrathin terahertz lens with axial long focal depth based on metasurfaces". In: *Optics Express* 21.24 (2013), pp. 30030–30038.

[113] Babak Memarzadeh and Hossein Mosallaei. "Array of planar plasmonic scatterers functioning as light concentrator". In: *Optics letters* 36.13 (2011), pp. 2569–2571.

[114] Anders Pors, Michael G Nielsen, René Lynge Eriksen, and Sergey I Bozhevolnyi. "Broadband focusing flat mirrors based on plasmonic gradient metasurfaces". In: *Nano letters* 13.2 (2013), pp. 829–834.

[115] Yinghong Gu, Lei Zhang, Joel KW Yang, Swee Ping Yeo, and Cheng-Wei Qiu. "Color generation via subwavelength plasmonic nanostructures". In: *Nanoscale* 7.15 (2015), pp. 6409–6419.

[116] Ting Xu, Haofei Shi, Yi-Kuei Wu, Alex F Kaplan, Jong G Ok, and L Jay Guo. "Structural colors: from plasmonic to carbon nanostructures". In: *Small* 7.22 (2011), pp. 3128–3136.

[117] Anders Kristensen, Joel KW Yang, Sergey I Bozhevolnyi, Stephan Link, Peter Nordlander, Naomi J Halas, et al. "Plasmonic colour generation". In: *Nature Reviews Materials* 2.1 (2017), p. 16088.

[118] Julien Proust, Frederic Bedu, Bruno Gallas, Igor Ozerov, and Nicolas Bonod. "All-dielectric colored metasurfaces with silicon Mie resonators". In: *ACS nano* 10.8 (2016), pp. 7761–7767.

[119] Arseniy I Kuznetsov, Andrey E Miroshnichenko, Mark L Brongersma, Yuri S Kivshar, and Boris Luk'yanchuk. "Optically resonant dielectric nanostructures". In: *Science* 354.6314 (2016), aag2472.

[120] Eng Huat Khoo, Er Ping Li, and Kenneth B Crozier. "Plasmonic wave plate based on subwavelength nanoslits". In: *Optics letters* 36.13 (2011), pp. 2498–2500.

[121] Yang Zhao and Andrea Alù. "Manipulating light polarization with ultrathin plasmonic metasurfaces". In: *Physical Review B* 84.20 (2011), p. 205428.

[122] Dacheng Wang, Yinghong Gu, Yandong Gong, Cheng-Wei Qiu, and Minghui Hong. "An ultrathin terahertz quarter-wave plate using planar babinet-inverted metasurface". In: *Optics express* 23.9 (2015), pp. 11114–11122.

[123] Jessie Y Chin, Mingzhi Lu, and Tie Jun Cui. "Metamaterial polarizers by electric-field-coupled resonators". In: *Applied Physics Letters* 93.25 (2008), p. 251903.

[124] Fei Ding, Anders Pors, and Sergey I Bozhevolnyi. "Gradient metasurfaces: a review of fundamentals and applications". In: *Reports on Progress in Physics* 81.2 (2017), p. 026401.

[125] Stefan Alexander Maier. *Plasmonics: fundamentals and applications*. Springer Science & Business Media, 2007.

[126] Nathaniel K Grady, Jane E Heyes, Dibakar Roy Chowdhury, Yong Zeng, Matthew T Reiten, Abul K Azad, et al. "Terahertz metamaterials for linear polarization conversion and anomalous refraction". In: *Science* (2013), p. 1235399.

[127] Longqing Cong, Wei Cao, Zhen Tian, Jianqiang Gu, Jiaguang Han, and Weili Zhang. "Manipulating polarization states of terahertz radiation using metamaterials". In: *New Journal of physics* 14.11 (2012), p. 115013.

[128] Wujiong Sun, Qiong He, Jiaming Hao, and Lei Zhou. "A transparent metamaterial to manipulate electromagnetic wave polarizations". In: *Optics letters* 36.6 (2011), pp. 927–929.

[129] Chen Shen, Yangbo Xie, Junfei Li, Steven A Cummer, and Yun Jing. "Asymmetric acoustic transmission through near-zero-index and gradient-index metasurfaces". In: *Applied Physics Letters* 108.22 (2016), p. 223502.

[130] Kwok L Chung and Sarawuth Chaimool. "Broadside gain and bandwidth enhancement of microstrip patch antenna using a MNZ-metasurface". In: *Microwave and Optical Technology Letters* 54.2 (2012), pp. 529–532.

[131] Lin Biao Wang, Kye Yak See, Jun Wu Zhang, Budiman Salam, and Albert Chee Wai Lu. "Ultrathin and flexible screen-printed metasurfaces for EMI shielding applications". In: *IEEE Transactions on Electromagnetic Compatibility* 53.3 (2011), pp. 700–705.

[132] Daniel F Sievenpiper. "Nonlinear grounded metasurfaces for suppression of high-power pulsed RF currents". In: *IEEE Antennas and Wireless Propagation Letters* 10 (2011), pp. 1516–1519.

[133] Nima Dabidian, Iskandar Kholmanov, Alexander B Khanikaev, Kaya Tatar, Simeon Trendafilov, S Hossein Mousavi, et al. "Electrical switching of infrared light using graphene integration with plasmonic Fano resonant metasurfaces". In: *Acs Photonics* 2.2 (2015), pp. 216–227.

[134] Manuel Decker, Christian Kremers, Alexander Minovich, Isabelle Staude, Andrey E Miroshnichenko, Dmitry Chigrin, et al. "Electro-optical switching by liquid-crystal controlled metasurfaces". In: *Optics express* 21.7 (2013), pp. 8879–8885.

[135] Edward F Kuester, Mohamed A Mohamed, Melinda Piket-May, and Christopher L Holloway. "Averaged transition conditions for electromagnetic fields at a metafilm". In: *IEEE Transactions on Antennas and Propagation* 51.10 (2003), pp. 2641–2651.

[136] Christopher L Holloway, Derik C Love, Edward F Kuester, Joshua A Gordon, and David A Hill. "Use of generalized sheet transition conditions to model guided

waves on metasurfaces/metafilms". In: *IEEE Transactions on Antennas and Propagation* 60.11 (2012), pp. 5173–5186.

[137] D Berry, R Malech, and W Kennedy. "The reflectarray antenna". In: *IEEE Transactions on Antennas and Propagation* 11.6 (1963), pp. 645–651.

[138] Sean Victor Hum and Julien Perruisseau-Carrier. "Reconfigurable reflectarrays and array lenses for dynamic antenna beam control: A review". In: *IEEE Transactions on Antennas and Propagation* 62.1 (2014), pp. 183–198.

[139] Jose A Encinar and J Agustin Zornoza. "Three-layer printed reflectarrays for contoured beam space applications". In: *IEEE Transactions on Antennas and Propagation* 52.5 (2004), pp. 1138–1148.

[140] Jonathan Y Lau and Sean V Hum. "Reconfigurable transmitarray design approaches for beamforming applications". In: *IEEE Transactions on Antennas and Propagation* 60.12 (2012), pp. 5679–5689.

[141] Hamza Kaouach, Laurent Dussopt, Jérome Lanteri, Thierry Koleck, and Ronan Sauleau. "Wideband low-loss linear and circular polarization transmit-arrays in V-band". In: *IEEE Transactions on Antennas and Propagation* 59.7 (2011), pp. 2513–2523.

[142] Max Born and Emil Wolf. *Principles of optics: electromagnetic theory of propagation, interference and diffraction of light*. Elsevier, 2013.

[143] Nanfang Yu, Patrice Genevet, Mikhail A Kats, Francesco Aieta, Jean-Philippe Tetienne, Federico Capasso, et al. "Light propagation with phase discontinuities: generalized laws of reflection and refraction". In: *science* (2011), p. 1210713.

[144] Francesco Aieta, Patrice Genevet, Nanfang Yu, Mikhail A Kats, Zeno Gaburro, and Federico Capasso. "Out-of-plane reflection and refraction of light by anisotropic optical antenna metasurfaces with phase discontinuities". In: *Nano letters* 12.3 (2012), pp. 1702–1706.

[145]   Jacob Scheuer. "Metasurfaces-based holography and beam shaping: engineering the phase profile of light". In: *Nanophotonics* 6.1 (2017), pp. 137–152.

[146]   Gabriel Biener, Avi Niv, Vladimir Kleiner, and Erez Hasman. "Formation of helical beams by use of Pancharatnam–Berry phase optical elements". In: *Optics letters* 27.21 (2002), pp. 1875–1877.

[147]   Ze'ev Bomzon, Gabriel Biener, Vladimir Kleiner, and Erez Hasman. "Radially and azimuthally polarized beams generated by space-variant dielectric subwavelength gratings". In: *Optics letters* 27.5 (2002), pp. 285–287.

[148]   Xingjie Ni, Naresh K Emani, Alexander V Kildishev, Alexandra Boltasseva, and Vladimir M Shalaev. "Broadband light bending with plasmonic nanoantennas". In: *Science* 335.6067 (2012), pp. 427–427.

[149]   Lixiang Liu, Xueqian Zhang, Mitchell Kenney, Xiaoqiang Su, Ningning Xu, Chunmei Ouyang, et al. "Broadband metasurfaces with simultaneous control of phase and amplitude". In: *Advanced Materials* 26.29 (2014), pp. 5031–5036.

[150]   Viktor G Veselago. "The electrodynamics of substances with simultaneously negative values of and μ". In: *Soviet physics uspekhi* 10.4 (1968), p. 509.

[151]   Dylan Lu and Zhaowei Liu. "Hyperlenses and metalenses for far-field super-resolution imaging". In: *Nature communications* 3 (2012), p. 1205.

[152]   Thomas BA Senior and John Leonidas Volakis. *Approximate boundary conditions in electromagnetics*. 41. Iet, 1995.

[153]   Thomas BA Senior and John L Volakis. "Sheet simulation of a thin dielectric layer". In: *Radio Science* 22.07 (1987), pp. 1261–1272.

[154]   MA Ricoy and JL Volakis. "Derivation of generalized transition/boundary conditions for planar multiple-layer structures". In: *Radio science* 25.4 (1990), pp. 391–405.

[155] Christopher L Holloway, Andrew Dienstfrey, Edward F Kuester, John F O'Hara, Abul K Azad, and Antoinette J Taylor. "A discussion on the interpretation and characterization of metafilms/metasurfaces: The two-dimensional equivalent of metamaterials". In: *Metamaterials* 3.2 (2009), pp. 100–112.

[156] Christopher L Holloway, Edward F Kuester, and Andrew Dienstfrey. "Characterizing metasurfaces/metafilms: The connection between surface susceptibilities and effective material properties". In: *IEEE Antennas and Wireless Propagation Letters* 10 (2011), pp. 1507–1511.

[157] C Strachan. "The reflexion of light at a surface covered by a monomolecular film". In: *Mathematical Proceedings of the Cambridge Philosophical Society*. Vol. 29. 1. Cambridge University Press. 1933, pp. 116–130.

[158] DV Sivukhin. "Contribution to the molecular theory of light reflection". In: *Comptes Rendus (Doklady) Acad. Sci. URSS*. Vol. 36. 1942, pp. 231–234.

[159] D Bedeaux and J Vlieger. "A phenomenological theory of the dielectric properties of thin films". In: *Physica* 67.1 (1973), pp. 55–73.

[160] Christopher L Holloway and Edward F Kuester. "Generalized Sheet Transition Conditions (GSTCs) for a MetascreenâĂŤA Fishnet Metasurface". In: *IEEE Transactions on Antennas and Propagation* (2018).

[161] Srikumar Sandeep, Jian-Ming Jin, and Christophe Caloz. "Finite-element modeling of metasurfaces with generalized sheet transition conditions". In: *IEEE Transactions on Antennas and Propagation* 65.5 (2017), pp. 2413–2420.

[162] Yousef Vahabzadeh, Nima Chamanara, and Christophe Caloz. "Generalized sheet transition condition FDTD simulation of metasurface". In: *IEEE Transactions on Antennas and Propagation* 66.1 (2018), pp. 271–280.

[163] Tom J Smy and Shulabh Gupta. "Finite-difference modeling of broadband Huygens' metasurfaces based on generalized sheet transition conditions". In: *IEEE Transactions on Antennas and Propagation* 65.5 (2017), pp. 2566–2577.

[164] Srikumar Sandeep, Jian-Ming Jin, and Christophe Caloz. "Finite-element modeling of metasurfaces with generalized sheet transition conditions". In: *IEEE Transactions on Antennas and Propagation* 65.5 (2017), pp. 2413–2420.

[165] Joshua A Gordon, Christopher L Holloway, and Andrew Dienstfrey. "A physical explanation of angle-independent reflection and transmission properties of metafilms/metasurfaces". In: *IEEE Antennas and wireless propagation letters* 8 (2009), pp. 1127–1130.

[166] Keith W Whites. *Electromagnetic wave propagation through circular waveguides containing radially inhomogeneous lossy media*. Tech. rep. CONSTRUCTION ENGINEERING RESEARCH LAB (ARMY) CHAMPAIGN IL, 1989.

[167] PJB Clarricoats and BC Taylor. "Evanescent and propagating modes of dielectric-loaded circular waveguide". In: *Proceedings of the Institution of Electrical Engineers*. Vol. 111. 12. IET. 1964, pp. 1951–1956.

[168] GN Tsandoulas. "Bandwidth Enhancement in Dielectric-Lined Circular Waveguides (Short Papers)". In: *IEEE Transactions on Microwave Theory and Techniques* 21.10 (1973), pp. 651–654.

[169] Silvio Hrabar, Juraj Bartolic, and Zvonimir Sipus. "Waveguide miniaturization using uniaxial negative permeability metamaterial". In: *IEEE transactions on antennas and propagation* 53.1 (2005), pp. 110–119.

[170] Fan-Yi Meng, Qun Wu, Daniel Erni, and Le-Wei Li. "Controllable metamaterial-loaded waveguides supporting backward and forward waves". In: *IEEE Transactions on Antennas and Propagation* 59.9 (2011), pp. 3400–3411.

[171] David M. Pozar. *Microwave Engineering, 4th Ed.* JohnWiley & Sons, Inc., 1999, p. 215.

[172] Justin G Pollock. "Analysis and Design of A New Class of Miniaturized Circular Waveguides Containing Anisotropic Metamaterial Liners". PhD thesis. University of Alberta, 2016.

[173] Justin G Pollock and Ashwin K Iyer. "Miniaturized circular-waveguide probe antennas using metamaterial liners". In: *IEEE Transactions on Antennas and Propagation* 63.1 (2015), pp. 428–433.

[174] Ugo Fano. "Effects of configuration interaction on intensities and phase shifts". In: *Physical Review* 124.6 (1961), p. 1866.

[175] Boris Luk'yanchuk, Nikolay I Zheludev, Stefan A Maier, Naomi J Halas, Peter Nordlander, Harald Giessen, et al. "The Fano resonance in plasmonic nanostructures and metamaterials". In: *Nature materials* 9.9 (2010), p. 707.

[176] Justin G Pollock and Ashwin K Iyer. "Experimental verification of below-cutoff propagation in miniaturized circular waveguides using anisotropic ENNZ metamaterial liners". In: *IEEE Transactions on Microwave Theory and Techniques* 64.4 (2016), pp. 1297–1305.

[177] George V Eleftheriades, Ashwin K Iyer, and Peter C Kremer. "Planar negative refractive index media using periodically LC loaded transmission lines". In: *IEEE transactions on Microwave Theory and Techniques* 50.12 (2002), pp. 2702–2712.

[178] Christophe Caloz, Atsushi Sanada, and Tatsuo Itoh. "A novel composite right-/left-handed coupled-line directional coupler with arbitrary coupling level and broad bandwidth". In: *IEEE Transactions on Microwave Theory and Techniques* 52.3 (2004), pp. 980–992.

[179] M Beruete, M Sorolla, I Campillo, and JS Dolado. "Increase of the transmission in cut-off metallic hole arrays". In: *IEEE Microwave and wireless components letters* 15.2 (2005), pp. 116–118.

[180]   Marinus T Vlaardingerbroek and Jacques A Boer. *Magnetic resonance imaging: theory and practice*. Springer Science & Business Media, 2013.

[181]   John Hunt, Tom Driscoll, Alex Mrozack, Guy Lipworth, Matthew Reynolds, David Brady, et al. "Metamaterial apertures for computational imaging". In: *Science* 339.6117 (2013), pp. 310–313.

[182]   Michael R Watts, Michael J Shaw, and Gregory N Nielson. "Optical resonators: Microphotonic thermal imaging". In: *Nature Photonics* 1.11 (2007), p. 632.

[183]   Giuseppe Castaldi, Silvio Savoia, Vincenzo Galdi, Andrea Alù, and Nader Engheta. "Analytical study of subwavelength imaging by uniaxial epsilon-near-zero metamaterial slabs". In: *Physical Review B* 86.11 (2012), p. 115123.

[184]   Silvio Savoia, Constantinos A Valagiannopoulos, Francesco Monticone, Giuseppe Castaldi, Vincenzo Galdi, and Andrea Alu. "Magnified imaging based on non-Hermitian nonlocal cylindrical metasurfaces". In: *Physical Review B* 95.11 (2017), p. 115114.

[185]   Elham Baladi and Ashwin K Iyer. "Far-field high-resolution imaging of conducting obstacles using metamaterial-lined aperture arrays". In: *Antennas and Propagation (APSURSI), 2016 IEEE International Symposium on*. IEEE. 2016, pp. 667–668.

[186]   Elham Baladi and Ashwin K Iyer. "Subwavelength metamaterial-lined apertures AS far-field imaging devices". In: *Antennas and Propagation & USNC/URSI National Radio Science Meeting, 2017 IEEE International Symposium on*. IEEE. 2017, pp. 1077–1078.

[187]   Elham Baladi, Justin G Pollock, and Ashwin K Iyer. "New approach for extraordinary transmission through an array of subwavelength apertures using thin ENNZ metamaterial liners". In: *Optics Express* 23.16 (2015), pp. 20356–20365.

[188] Karim Achouri, Mohamed A Salem, and Christophe Caloz. "General metasurface synthesis based on susceptibility tensors". In: *IEEE Transactions on Antennas and Propagation* 63.7 (2015), pp. 2977–2991.

[189] Edward A Parker and SMA Hamdy. "Rings as elements for frequency selective surfaces". In: *Electronics Letters* 17.17 (1981), pp. 612–614.

[190] TM Schafer, Jürgen Maurer, Jürgen von Hagen, and Werner Wiesbeck. "Experimental characterization of radio wave propagation in hospitals". In: *IEEE transactions on Electromagnetic Compatibility* 47.2 (2005), pp. 304–311.

[191] Ramprabhu Sivasamy, Lingeshwaran Murugasamy, Malathi Kanagasabai, Esther Florence Sundarsingh, and M Gulam Nabi Alsath. "A low-profile paper substrate-based dual-band FSS for GSM shielding". In: *IEEE Transactions on Electromagnetic Compatibility* 58.2 (2016), pp. 611–614.

[192] Ramprabhu Sivasamy and Malathi Kanagasabai. "A novel dual-band angular independent FSS with closely spaced frequency response". In: *IEEE Microwave and Wireless Components Letters* 25.5 (2015), pp. 298–300.

[193] Yajun Liu, Song Xia, Hongyu Shi, Anxue Zhang, and Zhuo Xu. "Dual-band and high-efficiency polarization converter based on metasurfaces at microwave frequencies". In: *Applied Physics B* 122.6 (2016), p. 178.

[194] Hailin Cao, Jianshuo Liang, Xiaodong Wu, Yuwei Pi, Hang Xu, Junjie Liu, et al. "Dual-band polarization conversion based on non-twisted Q-shaped metasurface". In: *Optics Communications* 370 (2016), pp. 311–318.

[195] Zhancheng Li, Wenwei Liu, Hua Cheng, Shuqi Chen, and Jianguo Tian. "Tunable dual-band asymmetric transmission for circularly polarized waves with graphene planar chiral metasurfaces". In: *Optics letters* 41.13 (2016), pp. 3142–3145.

[196] Muhammad Mubeen Masud, Bilal Ijaz, Irfan Ullah, and Benjamin Braaten. "A compact dual-band EMI metasurface shield with an actively tunable polarized lower band". In: *IEEE Transactions on Electromagnetic Compatibility* 54.5 (2012), pp. 1182–1185.

[197] Baoqin Lin, Buhong Wang, Wen Meng, Xinyu Da, Wei Li, Yingwu Fang, et al. "Dual-band high-efficiency polarization converter using an anisotropic metasurface". In: *Journal of Applied Physics* 119.18 (2016), p. 183103.

[198] Xiao-Dong Hu, Xi-Lang Zhou, Lin-Sheng Wu, Liang Zhou, and Wen-Yan Yin. "A miniaturized dual-band frequency selective surface (FSS) with closed loop and its complementary pattern". In: *IEEE Antennas and Wireless Propagation Letters* 8 (2009), pp. 1374–1377.

[199] Mingbao Yan, Shaobo Qu, Jiafu Wang, Jieqiu Zhang, Hang Zhou, Hongya Chen, et al. "A miniaturized dual-band FSS with stable resonance frequencies of 2.4 GHz/5 GHz for WLAN applications". In: *IEEE Antennas and wireless propagation letters* 13 (2014), pp. 895–898.

[200] Rong-rong Xu, Huai-cheng Zhao, Zhi-yuan Zong, and Wen Wu. "Dual-band capacitive loaded frequency selective surfaces with close band spacing". In: *IEEE Microwave and Wireless Components Letters* 18.12 (2008), pp. 782–784.

[201] Rong-Rong Xu, Zhi-Yuan Zong, and Wen Wu. "Low-frequency miniaturized dual-band frequency selective surfaces with close band spacing". In: *Microwave and Optical Technology Letters* 51.5 (2009), pp. 1238–1240.

[202] Fan-Cheng Huang, Cheng-Nan Chiu, Tzong-Lin Wu, and Yih-Peng Chiou. "A circular-ring miniaturized-element metasurface with many good features for frequency selective shielding applications". In: *IEEE Transactions on Electromagnetic Compatibility* 57.3 (2015), pp. 365–374.

[203] Li-Hua Yang, Zheng-Fei Wang, Zhi-Yuan Zong, Wen Wu, and Da-Gang Fang. "A miniaturized frequency selective surface based on convoluted ring slot". In: *Environmental Electromagnetics (CEEM), 2012 6th Asia-Pacific Conference on*. IEEE. 2012, pp. 63–66.

[204] Ivan Russo, L Boccia, G Amendola, and G Di Massa. "Tunable pass-band FSS for beam steering applications". In: *Antennas and Propagation (EuCAP), 2010 Proceedings of the Fourth European Conference on*. IEEE. 2010, pp. 1–4.

[205] L Boccia, I Russo, G Amendola, and G Di Massa. "Preliminary results on tunable frequency selective surface for beam steering transmit-array applications". In: *Antennas and Propagation (EUCAP), Proceedings of the 5th European Conference on*. IEEE. 2011, pp. 1002–1005.

[206] Manuel Decker, Isabelle Staude, Matthias Falkner, Jason Dominguez, Dragomir N Neshev, Igal Brener, et al. "High-efficiency dielectric Huygens' surfaces". In: *Advanced Optical Materials* 3.6 (2015), pp. 813–820.

[207] Ye Feng Yu, Alexander Y Zhu, Ramón Paniagua-Domínguez, Yuan Hsing Fu, Boris Luk'yanchuk, and Arseniy I Kuznetsov. "High-transmission dielectric metasurface with 2π phase control at visible wavelengths". In: *Laser & Photonics Reviews* 9.4 (2015), pp. 412–418.

[208] R Todd Lee and Glenn S Smith. "A design study for the basic TEM horn antenna". In: *IEEE Antennas and Propagation Magazine* 46.1 (2004), pp. 86–92.

[209] Daniel Maystre. "Theory of Wood's anomalies". In: *Plasmonics*. Springer, 2012, pp. 39–83.

Appendix A

The Custom-Designed TEM Horn Antenna

The TEM horn antenna presented here possesses a customized design to illuminate, as uniformly as possible, a 1D array of apertures when it is mounted on the mouth of the horn, as was discussed in chapter 5. The basic TEM horn antenna is constructed from two identical triangular plates each possessing an angular span of α, and separated from each other by an angle of β at the driving point [208]. A schematic of the basic TEM horn antenna design in shown in Fig.A.1.

To obtain an input impedance of $50\,\Omega$, a proper pair of design angles is chosen from the design curves shown in Fig. A.2, which were presented in [208]. In fact, Fig. A.2 introduces different combinations of design angles α and β that can be utilized to obtain the desired input impedance. These design curves for a double-sided TEM horn are adapted to the design of a single-sided horn using a ground plane, as shown in Fig. A.3. Due
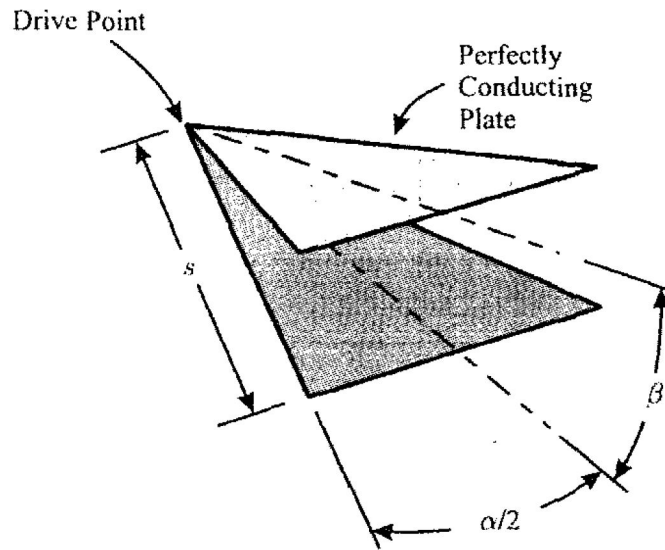
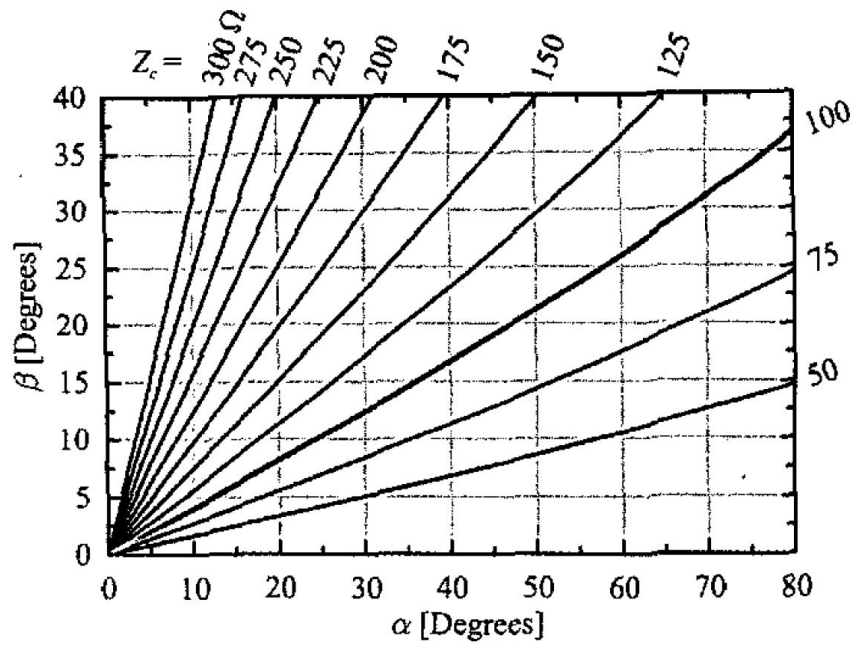FIGURE A.1: The schematic of the basic TEM horn antenna [208].

FIGURE A.2: The characteristic impedance of the TEM horn antenna for different combinations of design angles, α and β [208].

to various design considerations involved in accommodating the 1D aperture array presented in chapter 5 on the TEM-horn's mouth, $\alpha = 50°$ and $\beta = 8.5°$ were selected. This results in an overall height of 20 mm for the single-sided model shown in Fig. A.3, and a width of 195.06 mm. This width was truncated to 100 mm (equal to the width of the 1D aperture array) to avoid unwanted diffraction effects. The TEM horn antenna shown in Fig. A.3 possesses multiple matching regions around the frequencies where its length measured multiples of half wavelength. The overall length of this antenna is therefore chosen so as to place the matching region at the desired frequency range around 3 GHz. A $50\,\Omega$ coaxial feed is then designed for exciting this TEM horn antenna as shown in Fig. A.3. The SMA connector used to feed this antenna possesses an inner conductor that is extended and covered with a Teflon sleeve that improves the mechanical stability at the feed point and eases the practical implementation.

The electric field vectors of this custom-designed TEM horn antenna are plotted at the center of its desired matching region at 2.95 GHz. Uniform, TEM-like fields are observed at the mouth of the designed TEM horn antenna, specially away from the edges, as shown in Fig. A.4. A color bar (in linear format) is included to provide insight about the relative strength of electric field vectors at different points.
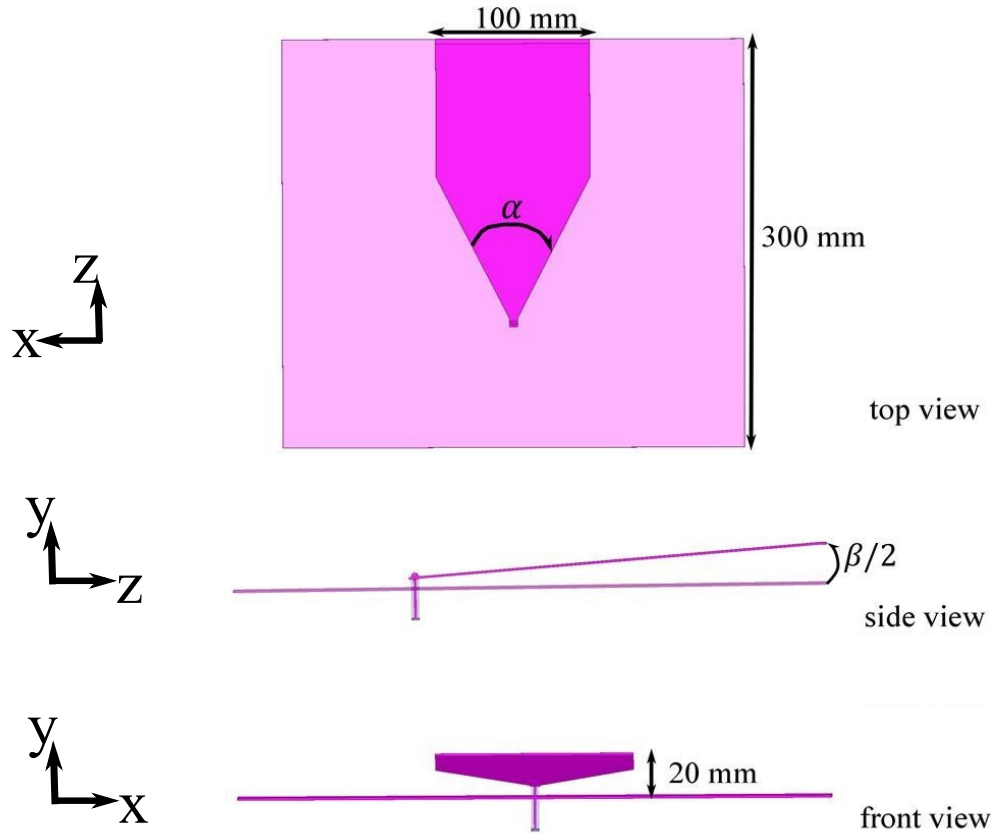
FIGURE A.3: Different views and dimensions of the custom-designed single-sided TEM horn antenna.
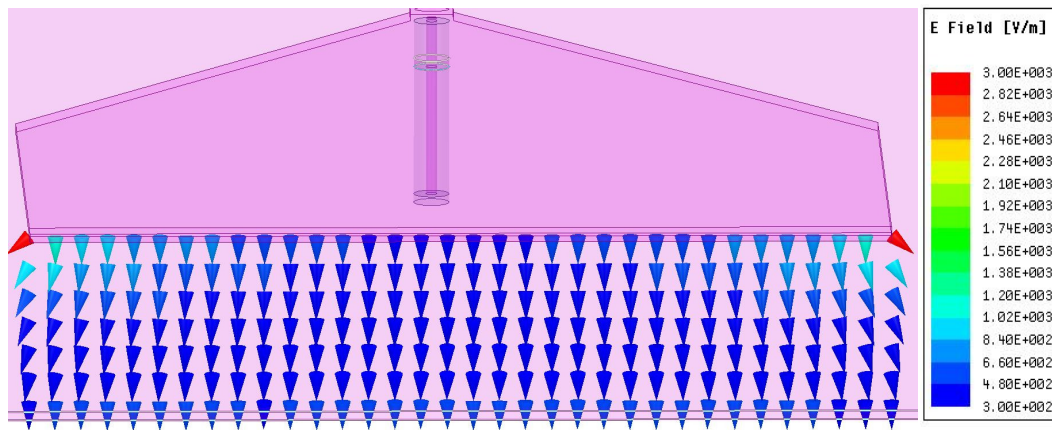

FIGURE A.4: Electric field vectors of the custom designed TEM horn antenna plotted at its mouth at 2.95 GHz.

Appendix B

The Wood-Rayleigh Anomaly

Grating anomalies were discovered by Wood in 1902 [21], when he observed the spectrum of light incident on a metallic diffraction grating at optical frequencies, for incident waves with magnetic field parallel to the grating grooves. The first interpretation for this phenomenon was offered by Rayleigh in 1907 [22]: Wood's anomaly occurs at the wavelength corresponding to the cutoff of a higher order mode, where the scattered wave travels tangential to the grating surfaces [22, 209]. This may also be calculated from the famous grating formula [209]:

$$Sin(\theta_n) = Sin(\theta) + n\lambda/d \qquad \text{(B.1)}$$

where n is the order of the diffracted wave, d is the period of the grating, θ is the incident angle with respect to the normal to the surface of the grating, and θ_n is the diffraction angle of the nth order diffracted wave with respect to the normal to the surface of the grating.

For normal incidence (i.e., $\theta = 0$), and at the cutoff frequency of the nth order mode (i.e., $\theta_n = \pm 90$), the above equation reduces to:

$$\pm 1 = n\lambda/d, n = \pm 1, \pm 2, \pm 3, ... \tag{B.2}$$

Therefore, the lowest diffraction anomaly (i.e., $n = 1$) occurs for $\lambda = d$. Equation B.2 rigorously explains the occurrence of Wood-Rayleigh anomaly, and its dependence to the angle of incidence.